

**IDENTIFYING FEEDBACK CONTROL STRATEGIES OF
RUNNING COCKROACHES AND HUMANS**

by

Jusuk Lee

A dissertation submitted to The Johns Hopkins University in conformity with the requirements for
the degree of Doctor of Philosophy.

Baltimore, Maryland

January, 2009

© Jusuk Lee 2009

All rights reserved

Abstract

In this dissertation, we model biological sensorimotor behaviors of two species, a cockroach following a wall and a human running on a split-belt treadmill, to elucidate the neural processing that underlie locomotor control in biological systems: (1) We model the horizontal musculoskeletal dynamics of antenna-based wall following for the American cockroach, *Periplaneta americana*, as a dynamic planar unicycle with an idealized antenna. Performing nonlinear regression on the transient responses of blinded cockroaches running along various wall perturbations, we show that the stabilizing neural feedback requires not only the distance-to-wall information but also the rate of approach to the wall. We corroborate this result using a robotic platform equipped with an artificial antenna, a numerical simulation of antenna-based lateral leg spring (LLS) model, and a comparison with a neurophysiological experiment. (2) For human running, we model the sagittal-plane feedback control strategies during early and late adaptation phases of split-belt treadmill running. For the early adaptation phase, we assume spring-loaded inverted pendulum (SLIP) body mechanics with compositions of one-step deadbeat feedback controllers; we show that the compositions of slow-belt feedback controllers best represented the steady-state human

ABSTRACT

running data. We compare the eigenvalues of the linearized stride-to-stride return map during late adaptation with those during baseline tied-belt running. Our result suggests larger eigenvalues (i.e. slower recovery rate) during late adaptation, suggesting that adapted split-belt is not simply the dynamic composition of a fast steps and slow steps.

Primary Reader: Noah J. Cowan

Readers: Amy J. Bastian, Louis L. Whitcomb

Acknowledgements

I would first like to thank my adviser, mentor, teacher, and friend, Professor Noah Cowan. Noah, you have been an inspiration since the day I met you. Thank you for being available day or night, when you were sick or tired, on weekends, and even while you were on vacation. Your positive encouragement, immense patience, tireless support, and constant guidance are what carried me forward to this day. Thank you for everything.

I would like to thank my dissertation committee members Professor Amy Bastian and Professor Louis Whitcomb for providing critical and detailed comments about my dissertation. I would also like to thank Julia Choi for her generosity with her time and effort in helping me learn about human locomotion and collect running data. I would like to thank Simon Sponberg for his time and effort in helpful discussions about cockroach locomotion.

I would like to thank my current and previous LIMBS lab family: Vinutha Kallem, Eatai Roth, John Swensen, Danoosh Vahdat, Shahin Sefati, Terrence Jao, Alican Demir, Avik De, Katie Zhuang, Sean Carver, Kyle Reed, Erion Plaku, Owen Loh, Andy Lamper-ski, Brett Kutscher, Landon Unninayer, and Mo Ramadan. I will cherish the time we've

ACKNOWLEDGEMENTS

shared, the research we've discussed, and the laughter we've enjoyed.

I would like to thank all of my friends and colleagues from Hopkins that I've had the privilege of knowing: Jin Seob Kim, Wooram Park, Kiju Lee, Jong Hee Lee, Sung-Ouk Chang, Sarah Webster, Tom Wedlick, Katherine Acton, Lawton Verner, Tomo Yamamoto, Sarthak Misra, Matt Moses, and all other friends in the Haptics Lab, Dynamical Systems and Control Lab, Robot and Protein Kinematics Lab, the ME department and in LCSR.

I would like to thank all the professors who have provided guidance and inspiration throughout my undergraduate and graduate career: Professors Amy Bastian, Greg Chirikjian, Ronald Fearing, Eric Fortune, Robert Full, Karl Hedrick, Allison Okamura, Wilson Rugh, Reza Shadmehr, and Louis Whitcomb. I would like to thank the JHU ME professors for their encouragement and support for Mechanical Engineering Graduate Association. Thank you Mike, Katy, Deana, and the rest of the ME staff for your outstanding and wonderful service to the ME community.

Most importantly, I would like to thank my parents and my two sisters, Yunji Lee and Yunhee Lee, for their unending and unconditional love and support.

Dedication

To my loving parents, Dr. Boo-Kyoon Lee and Ok Sun Kim.

Contents

Abstract	ii
Acknowledgements	iv
List of Tables	xii
List of Figures	xiii
1 Introduction	1
1.1 Modeling Musculoskeletal Body Mechanics	3
1.2 Modeling Neural Control	4
I Cockroach Locomotion	7
2 Motivation	8
2.1 Roadmap	9
2.2 Dissemination	10
3 Background: American Cockroaches and LLS Model	12
3.1 Review: Lateral Leg Spring (LLS) Model	13

CONTENTS

3.2	American Cockroach: Antenna and Behavior	16
4	Antenna-Based Planar Unicycle	19
4.1	Model: Antenna-Based Planar Unicycle (APU)	20
4.2	Prediction: P Control Is Insufficient	24
4.3	Experiment: Cockroach Wall Following	29
4.3.1	Animal Husbandry	29
4.3.2	Wall-Following Arena	29
4.3.3	Animal Preparation	33
4.3.4	Kinematics	33
4.3.5	Finding the Point of Rotation	35
4.3.6	Data Filtering and Normalization	36
4.3.7	Dynamic Model Fitting and Testing	38
4.4	Results and Discussions	40
4.4.1	Model Validation	41
4.4.2	P Control Is Insufficient	41
4.4.3	Basis of Planar Unicycle Model	45
4.4.4	Alternative View of the Effects of Delay	47
4.4.5	Multimodal Role of Antennae in Mechanosensory Integration	49
5	Robotic Integration of Bio-Inspired Antenna	50
5.1	Garcia Robot	51
5.2	Robotics Model: Implementation	52
5.2.1	Antenna Design	52

CONTENTS

5.2.2	Integrating the Antenna with the Garcia Robot	54
5.2.3	Dynamically Scaled Parameters of <i>P. americana</i>	55
5.3	Experiment: Robotic Wall Following	58
6	The Antenna-Based Lateral Leg Spring	60
6.1	Model: LLS (2D Placement of COP)	61
6.1.1	Hybrid Step-to-Step Dynamics	62
6.1.2	Reduced Return Map	64
6.2	Model: Antenna-Based LLS (ALLS) Under PD Control	65
6.3	Simulation: ALLS Wall Following	68
7	Discussion	69
7.1	Multilevel Modeling	71
7.2	Chaplygin Sleigh and APU	72
7.3	Cockroach Antenna Neural Recordings	73
7.4	Biologically-Inspired Tactile Sensors	75
7.5	Robotics for Biology	76
7.6	ALLS for Biology and Robotics	77
7.7	Within-Modality Sensory Integration	78
8	Conclusion	80
A	ALLS Simulation	81
A.1	Simulation Methods	81
A.2	Parameters for <i>P. americana</i>	82

CONTENTS

B	Analysis of COP Placements	84
B.1	Effects of Various COP Placements	85
B.2	Stability as a Function of Fixed COP Position	92
B.3	Comparing Fixed vs. Moving COP Models	95
C	Derivation of Chaplygin Sleigh Using Lagrange–D’Alembert Principle	98
II	Human Locomotion	101
9	Motivation	102
9.1	Biology: Humans	103
9.1.1	Gaits	103
9.1.2	Mechanics and Control of Locomotion	105
9.2	Modeling: Human Movement	109
9.3	Roadmap	110
9.4	Dissemination	111
10	Spring-Loaded Inverted Pendulum (SLIP) Model With Deadbeat Feedback Control	112
10.1	SLIP Model and Simulation	113
10.1.1	Review: SLIP Model	113
10.1.2	SLIP: Equations of Motion	114
10.1.3	Tied-Belt Treadmill vs. Overground Running	115
10.1.4	Tied-Belt Treadmill vs. Split-Belt Treadmill	117
10.2	Deadbeat Feedback Control	118

CONTENTS

10.2.1	Deadbeat Control	118
10.2.2	Early Adaptation Control Strategy	120
10.3	Results and Discussion	122
10.3.1	Results: SLIP Predictions vs. Human Data	122
10.3.2	Discussion	122
11	Blackbox Closed-Loop System Identification	127
11.1	Blackbox Model	127
11.2	Experiments: Human Split-Belt Treadmill Running	128
11.2.1	Experiment Setup and Data Analysis	128
11.3	Results and Discussion	132
11.3.1	Results	132
11.3.2	Discussion	139
12	Conclusion	143
	Bibliography	145
	Vita	159

List of Tables

4.1	Parametric fit for PD-control models	43
5.1	Parameter values for <i>P. americana</i> (from Chapter 4) and the Garcia robot.	55
11.1	Parameters for segmental analysis from [40]. Note, we omitted “Forearm, hand” and “Upper arm” segments (not listed here) discussed in [40].	128

List of Figures

1.1	Animals of different shapes and sizes share similar qualitative vertical and fore-aft foot force patterns (shown in the middle of the figure). For each animal, stance legs (filled circle) and swing legs (open circle) are shown during two consecutive steps. The COM motion during each stance follows similarly as a SLIP. (Image credit: [50]; copyright ©2006 Society for Industrial and Applied Mathematics. Reprinted with permission. All rights reserved.)	2
1.2	(A) Cockroach running is modeled in the lateral plane as a lateral leg spring (LLS) model (Section 3.1; [96]); the three stance legs, indicated by the three small arrows, are represented by a single <i>virtual</i> massless spring leg. (Image credit: [95]; with kind permission from Springer Science+Business Media:Figure 1(a) in [95]) (B) Human running is modeled in the sagittal plane as a spring-loaded inverted pendulum (SLIP). (Image credit: [100])	4
1.3	Layers of abstractions from transistors (hardware) to high-level programs (software). (Image credit: [49])	5
2.1	Top view of an <i>P. americana</i> running along a corridor with sensory obstacles. . . .	9
2.2	Our research program involves multiple levels of modeling, and biological and robotic experimentations. Here, we present three models: the antenna-based planar unicycle (APU, Chapter 4), a model for our Garcia robot (Chapter 5), and the antenna-based LLS (ALLS, Chapter 6). Importantly, each level of modeling admits the same control structure, including parameters (up to a scale factor), that was fitted to cockroach wall-following data (Chapter 4). The two physical systems involved in this study are <i>P. americana</i> (Chapter 4) and a differential drive mobile robot (Chapter 5). Eventually, we plan to extend our modeling effort to more elaborated anchors, such as the planar, multi-legged model proposed by Seipel et al. [104], or the spatial SimSect model developed by Saranli et al. [90] of RHex [91]. As well, we plan to extend our experimental robotics work to include a RHex-like six legged robot, endowed with an artificial antenna.	9
3.1	(A) Dorsal view of an American cockroach (<i>Periplaneta americana</i>). (Image credit: [58]) (B) A view of ventral side of <i>P. americana</i> . (Image credit: [119]) The two images are scaled to closely match the actual size of <i>P. americana</i>	13
3.2	A schematic diagram of lateral leg spring model.	14

LIST OF FIGURES

3.3 Scanning electron micrograph of *P. americana*'s head. Scale bar = 1000 μm ; Co: Compound eye; Fl: Flagellum; Pd: Pedicle; Oc: Ocellus; Sc: Scape. (Image credit: [102]) 17

3.4 Scanning electron micrograph of *P. americana*'s antenna. Scale bar = 100 μm (Image credit: [74]) 18

4.1 (A) Depiction of a cockroach following a straight wall. L is the farthest point ahead of the cockroach's point of rotation (POR), as measured along the body axis, that the antenna contacts the wall. The bold arrow at the bottom indicates the leading point on the antenna that is in contact with the wall. (B) Unicycle model of the running cockroach. The model parameters are ℓ , the preview distance; d , the antenna measurement; v^* , the forward running speed; ω , the angle of the cockroach body relative to the wall (positive is measured counter clockwise (CCW) for all angles, angular velocities and moments; note that $\theta < 0$ in this figure); $\dot{\omega}$, the angular velocity of the body; u , the moment applied by the legs about the POR. The preview distance ℓ may be less than L since the model does not account for neural and muscle activation delays. In the model, the angle of the POR velocity, ϕ , is the same as the body angle, θ , so ϕ is not shown for clarity. 20

4.2 Block diagram of simplified control model. The "mechanics" box represents the torsional dynamics, and relates the body moment, u , to the body angle, θ . The "sensing" box is a simplified model of the antenna sensing kinematics, and it dynamically relates the cockroach angle, θ , to the antenna sensor measurement, d . We fit a simplified neural controller (in the dashed box), in which the error between a nominal "desired" wall-following distance, d^* , and the measured distance, d , is fed back through a PD controller. This control model enabled us to test PD control ($K_D \neq 0$) against P control ($K_D = 0$). 22

4.3 Root locus plots (see, e.g. [31]) of the transfer function of $\tilde{G}(\tilde{s})$ given by (4.8) for five characteristic values of the dimensionless inertia, \tilde{J} . Each plot depicts the locus of poles (roots of the denominator) of the closed-loop system (Fig. 4.2) under P control. The three open-loop poles (roots of the denominator of (4.8)) are indicated by X's, and therefore there are three branches of the root locus (magenta, green, blue). There is an open-loop zero (root of the numerator of (4.8)) at -1, indicated by a circle. The small inset plot (d vs. t) for each root locus depicts a typical response of the hypothetical closed-loop system. For stability, all of the poles of the closed-loop system must be in the open left-half-plane, that is, they must have negative real parts. (A) For $\tilde{J} < 1/9$, all of the poles are in the left-half-plane; the inset shows an over-damped response of d vs. t . (B) For $\tilde{J} = 1/9$, the system would be critically damped with $K_P = 3$. (C) For $1/9 < \tilde{J} < 1$, the system would be underdamped under P control. (D) For $\tilde{J} = 1$, the system would be oscillatory for all choices in gain, K_P . (E) For $\tilde{J} > 1$, the system would be unstable. Since \tilde{J} approaches or exceeds 1 for behaviorally relevant running speeds (4.13), these graphs preclude the possibility of P control. Stability can be greatly improved by adding a derivative feedback term, as in (4.12), enabling larger values of \tilde{J} 27

LIST OF FIGURES

4.4 Three Nyquist plots of the system in (4.14) are shown for three characteristic values of the dimensionless neural delay, \tilde{T} , assuming that $\tilde{J} = 0$. Delay cannot be handled using the root locus method; thus, we resort to Nyquist’s stability criterion (see, e.g. [31]). (A) $\tilde{T} < 1$. (B) $\tilde{T} = 1$. (C) $\tilde{T} > 1$. Each plot is constructed by evaluating the transfer function in (4.14) along the imaginary axis. Because the open-loop system has no open right-half-plane poles, the closed-loop system is stable if the Nyquist plot does not encircle -1 on the complex plane. As can be seen, this is only possible for the case that (A) $\tilde{T} < 1$, whereas for (B-C) $\tilde{T} \geq 1$, there will always be at least two encirclements of -1, and thus at least two right-half-plane poles. Stability can be greatly improved by adding a derivative feedback term, as in (4.12), enabling larger values of \tilde{T} 28

4.5 Illustration of wall-following arena viewed from side and from each camera. (A) Two high-speed cameras were positioned above an enclosed arena. The field-of-view of each camera was centered on an observation wall. Half-silvered mirrors in front of each camera reflected light from a fiber-optic illuminator onto the retroreflective running substrate, providing a stark silhouette of the cockroach despite very low ambient light. (B) The arena viewed from above showing the two cameras’ overlapping fields of view. 30

4.6 Image of the wall-following arena illustrated in Fig. 4.5A. In this image, the room light is on to show the setup. 31

4.7 Multiple exposures of a cockroach running along an angled wall during a single trial. 32

4.8 Three-dimensional lego blocks with retroreflective markers (gray circles). This object is placed in the arena in view of both cameras; the known relative marker positions and the markers seen from the cameras are used for camera calibration. 34

4.9 Instantaneous motion of the unicycle model. The two empty circles correspond to the two retroreflective markers that are used to finding the point of rotation locate the position of the POR (denoted as two concentric circles). v is the forward velocity; ω is the rotational velocity; v^\perp is the component of the velocity of the rear marker perpendicular to the body’s fore-aft axis; α is the distance between the rear marker and the POR. 36

4.10 Relationship between stride-averaged ϕ and θ . Each data point consists of the averaged ϕ and θ values during a stride. We analyzed 1079 strides observed in 59 trials from 11 individuals. The best fit line (solid line) and the model, $\phi = \theta$ (broken line), are both shown. 41

4.11 Average cockroach distance to the wall y (A,B) and body angle θ (C,D) as a function of distance traveled along the 45° angled wall for two different speed groups (Slow A,C and Fast B,D). The actual cockroach data (black) is compared to predictions from the PD-control model (red) using the parameters from Table 1. To show the importance of the derivative gain, K_D , we tested the controller with the $K_D = 0$ (P control, blue); note that for P control, performance degrades with increasing speed as expected. The derivative gain significantly improved the fit for the speeds tested. 42

LIST OF FIGURES

5.1 An overview of the cast urethane antenna construction process. Four flex sensors are enclosed in urethane casting with precurved tip. This bio-inspired antenna provides robot-to-wall distance information for the Garcia robot. This antenna is designed and built by Owen Loh [63, 64]. 52

5.2 The cast urethane antenna with embedded flex sensors mounted on the Garcia robot. 53

5.3 The Garcia robot’s internal states during a trial with parameters from Table 5.1. The onset of the angled wall contact occurs at $t = 1$ s. (A) Measured forward speed (solid) with $v^* = 0.5$ m/s (dashed). (B) Measured raw (solid black) and filtered (solid gray) d values with $d^* = 0.17$ m (dashed); to reduce noise, we low-pass filtered raw distance measurements: $d_k = \lambda d_{k-1} + (1 - \lambda)d_{\text{raw},k}$ where $\lambda = 0.7$ (trial and error); \dot{d} was estimated via finite difference. (C,D) Body angle and position obtained from overhead camera images. 56

5.4 The raw amplified voltage values from the four flex sensors embedded in our antenna; they are shown for their qualitative form. The flex sensor at the base of the antenna (A), which is not used to calculate the value d_{raw} in Fig. 5.3B, shows the onset of the angled wall contact with a sharp peak. The second flex sensor from the base (B) registers zero motion because it is anchored to the rigid support base discussed in the main text. The two distal flex sensors (C,D) are used to calculate the measurement d_{raw} shown in Fig. 5.3B. The third flex sensor (C) flexes more (indicated by the decrease in voltage values) as it encounters the initial part of the angled wall. Meanwhile, the remaining distal part of the antenna (D) conforms to the wall by decreasing its flexion (indicated by the increase in voltage values). . . . 57

6.1 (A) A schematic model of the LLS model; θ is the body angle w.r.t. the x -axis in inertial frame $\{U\}$, v is the speed of the COM, δ is the velocity angle w.r.t. the x -axis of the body frame $\{B\}$, ζ is the distance from the foot placement to the COM, ψ is the angle from the x -axis of the foot frame $\{F\}$ to the COM, η is the leg length, $[a_1, a_2]^T$ is the location of the COP written in $\{B\}$. (B) Illustration of multi-step dynamics and its equivalent representations. 61

6.2 Maximum non-unity eigenvalue for the linearized return map at various fixed-COP positions around the COM. Parameters used for *P. americana* are shown in the caption of Fig. 6.3. 63

6.3 A full stride of LLS at its equilibrium point with the following parameters: $m = 0.77 \times 10^{-3}$ kg, $J = 1.0 \times 10^{-7}$ kgm², $l_0 = 0.0165$ m, $k = 0.766$ N/m, $\beta = 1.051$ rad, $a_1 = 0$ m, $a_2 = -0.003$ m, $v(0) = 0.359$ m/s. In the last subplot, dashed and solid lines are a_1 and a_2 , respectively. 66

LIST OF FIGURES

7.1 Subplots (A,B,D,E) show the task-space trajectories of several models and physical systems from our research program (Fig. 2.2); *’s and o’s indicate COM position and body angle, respectively, at the start of every stride (or dimensionally equivalent stride); (B,D,E) have dimensionally equivalent parameters and the same PD-control law as discussed in the text. (A) A typical trial of *P. americana* (the cockroach is shown every other stride); the cockroach is following the wall at ~ 45 cm/s. (B) APU model simulation using the parameters given in Table 5.1, first row. (C) Neural recording near the base of flagellum. (Image credit: [64]) (D) The Garcia robot experiment, where the robot is shown every other “stride”; the robot uses parameters given in Table 5.1, second row. (E) The ALLS model simulation, shown at the start of every step with *’s indicating COM, x’s indicating COP, and straight lines emanating from COP indicating the effective leg. 70

7.2 Chaplygin sleigh. The skate provides a nonholonomic constraint. d is positive as shown. The two small circles indicate frictionless sliders. 71

7.3 Electroantennogram setup to observe afferent signals from the flagellum under a simulated experiment that mimics a wall-following behavior. A live American cockroach is placed on its back (ventral side up) with its body and the base of its flagellum restrained. The RC servo drives the wall segment closer to the cockroach thus bending the antenna at a rate that resembles the sensory signal during first few strides of angled-wall following. A tungsten electrode is inserted near the base of the flagellum to provide extracellular recording from the antennal nerve; D: distal part of the antenna, P: proximal part of the antenna. (Image credit: [64]) 73

7.4 Comparison of the antenna neural recording to the kinematic data of a running cockroach. (A) The position (dashed) and orientation (solid) of a cockroach running along a wall (Fig. 4.7); strides are marked by asterisks (*). (B) Normalized neural RMS power (mean (black) with confidence interval (gray)) of the antenna when the wall approached toward the cockroach and stopped; it has been scaled to approximately match the kinematic traces above. (C) Raw neural recording voltage (black) and background voltage (gray). (D) Time trace of the actual wall displacement (black) and delay-accounted wall displacement (gray). The vertical lines indicate (from left to right) the stimulation onset, RMS peak time, and settling time. (Image and caption credit: [64]) 74

7.5 Preliminary experiments to address how a cockroach might integrate sensory information from both of its antennae. A cockroach that is following a wall using its right antenna is faced with (A) impulse-like signal, (B) step-like signal, or (C) ramp-like signal from its left antenna. How would the new information from its left antenna contribute to its right antenna wall-following control strategy? Also in (B), will it continue to follow the right wall or will it start to follow the left wall using its left antenna? 79

LIST OF FIGURES

A.1 (A) Stride length versus speed and (B) stride frequency versus speed of the first 4 strides (prior to angled-wall contact) of 43 trials from the data from Chapter 4. The solid line is the linear fit of the data. The dashed line is the linear fit of the data collected by Full and Tu [37]. Unlike Full and Tu, we use cockroaches that are blinded and elicited an escape response and following a wall (Section 4.3). We assume that the data is adequate for our preliminary fitting of the LLS model, and we reduce the bias incurred from wall following by matching the waveform characteristics (e.g. stride length and stride frequency) rather than the waveform itself. 82

B.1 A schematic model of the LLS model, showing the coordinates used by Lee et al. [62]. 85

B.2 *Left:* A stride of the original LLS model ($d_1 \equiv 0$) with a fixed COP (solid) and a moving COP (dashed). The used parameters for the fixed COP are: $v = 0.226$ cm/s, $k = 2.4$ N/m, $\beta_0 = 1$ rad, $l_0 = 0.0102$ m, $d_2 = -0.0025$ m; for the moving COP are: $v = 0.2235$ m/s, $k = 3.52$ N/m, $\beta_0 = 1.125$ rad, $l_0 = 0.0082$ m, $d_2 = 0.0025$ m $\rightarrow -0.0025$ m. *Right:* Experimental measurements of *Blaberus discoidalis* from several sources, [36, 37, 59]; figure from [95]. (Notice, since the right figure doesn't start from $t = 0$, the stride period is roughly the same between the two figures.) 86

B.3 COP placement protocols for a left step with respect to the body frame $\{B\}$. The solid dots indicate fixed COP positions; the arrows indicate the direction, magnitude, and offset of moving COPs. 87

B.4 See text for description of each COP protocol. The parameters used in this figure are: $m = 0.0025$ kg, $I = 2.04 \times 10^{-7}$ kg m², $k = 3.52$ N m⁻¹, $v = 0.2275$ m/s, $l_0 = 0.0127$ m, $\beta_0 = 1.12$ rad (or 64.2°). Note, unlike Fig. B.2, these figures have scaled units (e.g. cm and mN) for clarity. 88

B.5 The parameters used here are: $m = 0.0025$ kg, $I = 2.04 \times 10^{-7}$ kg m², $k = 3.52$ N m⁻¹, $v = 0.2235$ m/s, $l_0 = 0.0082$ m, $\beta_0 = 1.125$ rad. 89

B.6 Parameters used are: $m = 0.0025$ kg, $I = 2.04 \times 10^{-7}$ kg m², $k = 3.52$ N/m, $v = 0.2235$ m/s, $l_0 = 0.0082$ m, $\beta_0 = 1.125$ rad. 90

B.7 Maximum eigenvalue (neglecting two invariant unity eigenvalues for energy and direction) of the linearized return map as a function of our new, two dimensional COP locations. The dark gray indicates the parameter regime of maximum stability and the neutral stability occurs when the contour reads 1. Eigenvalues greater than 3 are empty. The parameter values used are: $v = 0.25$ m/s, $k = 2.4$ N m⁻¹, $l_0 = 0.01$ m, $\beta_0 = 1$ rad, and -0.02 m $< d_1, d_2 < 0.02$ m. 93

B.8 Contour map of the maximum non-unity eigenvalue and the equilibrium points δ^* , θ^* , and $\dot{\theta}^*$. The parameter values are the same as Fig. B.7. 94

B.9 Comparison between moving and fixed COP. $m = 0.0025$ kg, $I = 2.04 \times 10^{-7}$ kg m², $k = 3.52$ N m⁻¹, $\beta_0 = 1.125$ rad. Moving COP (dashed) $v = 0.2235$ m/s, $l_0 = 0.0082$ m, $d_1 = 0$ m, $d_2 = 0.002 \rightarrow -0.002$ m. Fixed COP (solid) $v = 0.2275$ m/s, $l_0 = 0.0128$ m, $d_1 = 0.005$ m, $d_2 = 0$ m. 95

B.10 Comparison between a moving COP and an effective fixed COP during a left step under different protocols. Fixed COP is denoted by a filled dot, and the moving COP is denoted by a gray arrow. 96

LIST OF FIGURES

9.1 Leg kinematics at slow (first row) or fast (seconds row) leg touchdown. During *slow baseline* the subject has similar leg kinematics. During *early adaptation* the split-belt condition causes different shapes at fast or slow touchdowns. During *late adaptation* the legs become more symmetric. During *post adaptation* the learning has retained and causes asymmetric gait even though the belts are turning at the same speed. (Image credit: [83]; used with permission) 103

9.2 Oxygen consumption rate as a function of gait and speed. Notice the minimum of those three curves are indeed the preferred speeds and gaits for those horses. (Reprinted by permission from Macmillan Publishers Ltd: Nature [51], copyright 1981) 104

9.3 (A) A general overview of active pathways in the brain during motor control. Sensory signals (e.g., vision through thalamus or proprioception through the spinal cord) are integrated into the cerebral cortex and limbic system where movements are first initiated. Basic movements are executed in the brainstem and spinal cord which are refined and regulated by the cerebral cortex, basal ganglia, and cerebellum. [112] (Image credit: [112]; reprinted by permission from Koninklijke Brill NV) (B) A general overview of active pathways in the spine during locomotor movements. The descending commands from the brain adjust the interneurons and motoneurons in the spine to modulate the rhythm (generated by the central pattern generator) and pattern of locomotion. The sensory afferents (cutaneous and proprioceptive), in addition to their connections to the supraspinal structures, are directly connected to interneurons and motoneurons in the spine. [112] (Image credit: [112]; reprinted by permission from Koninklijke Brill NV) 107

10.1 Overground running of the SLIP model (moving from left to right). Each i -th step has five phases denoted in superscripts: AP1, apex prior to i -th stance; TD, touch-down; MC, maximum compression; LO, liftoff; AP2, apex after i -th stance. A black spring leg represents one leg and a gray spring represents the other leg. 113

10.2 Comparison between the actual belt speed and the perceived belt speed. The upper figure is the same as the one shown in Fig. 10.1; the figure is not drawn to match the changing belt speeds. The lower figure shows the the actual belt speed (thick gray line) and our assumed perceived belt speed (thin black line). This shows that the belt speed during the flight phase is composed by $v_{belt,i}^{LO}$ and $v_{belt,i+1}^{TD}$ and does not depend on the actual belt speed. 116

10.3 (A) Illustration of the SLIP motion under the split-belt condition. q_i 's are states at apex (AP- or AP+) and r_i 's are states at maximum compression (MC). (B)-(F) are different schemes for control during a "step." A deadbeat controller associated to the slow belt (B) or fast belt (C) is used. The rest of the controller schemes (D)-(F) alternate between slow-belt and fast-belt deadbeat controller in different phases. . . 121

10.4 Early adaptation stage of split-belt running trial. Filled circles are the fast leg, open circles are the slow leg. The third row shows the leg spring stiffness (normalized by mass) during compression and decompression phase of the stance. The height at apex for a slow leg (fast leg, resp.) shows the apex height immediately after the slow-leg (fast-leg, resp.) liftoff. 124

LIST OF FIGURES

10.5 Simulation of the scheme Fig. 10.3 (B) for belt speeds 2 and 2.5 m/s. Notice that the relative scale of the fast leg data to the slow leg data are consistent with the human trial experiment shown in Fig. 10.4. 125

10.6 (Continuation of Fig. 10.5) The % stance time is the stance time of each leg with respect to its stride (two consecutive steps) time. The treadmill-position-error plot shows one of the mismatches of the model to the human trial: the SLIP model drifts forward when running on a split-belt treadmill. 126

11.1 3D kinematic data of marker positions. Note, for the actual data collection, we did not collect wrist and elbow positions because those values did not have major contributions to the overall COM dynamics. The filled green circle is the approximated COM using the segmental analysis discussed in the text. 129

11.2 Experiment design. Red line is the right belt speed and blue line is the left belt speed. The tick marks show when the subject took breaks, when the perturbation took place, and when the metronome was on. f_s^{stride} , f_m^{stride} , f_f^{stride} , and f_{sf}^{stride} are stride frequencies for the slow (2.4m/s), medium (2.8m/s), fast (3.2m/s), and split (2.4 and 3.2m/s), resp., belt speeds. Those frequencies are measured using a stop watch during E0 and E4 phase; the metronome uses those frequencies during E1, E2, E3, E5, and E7 as shown in the last row. 131

11.3 Collected data during E3 phase of a trial plotted against time. The first row shows the belt speeds for the left (red) and right (blue) belts; the crosshairs (+) indicate touch down of the corresponding leg. The second row shows the forward position of the COM; black dots (●), for the remaining plots, indicate COM apexes. The third row shows the height of the COM. The fourth row shows the forward speed of the COM. The fifth row shows the vertical speed of the COM. 134

11.4 Superposition of belt speed and acceleration perturbations of similar types during E3 phase and their corresponding COM responses plotted against *steps*. The first row shows the belt speed at at every touchdown. The second row shows the belt average acceleration during *i*-th stance phase. The third row shows the fore-aft position of the COM at apex. The fourth row shows the height of the COM at apex. The last row shows the COM forward speed at apex. Because we do not distinguish left versus right legs, step-to-step oscillations are introduced when there are unintentional offsets in belt speeds and marker positions. 135

11.5 Effects of different running speeds and adaptation. The values are median of 50 contiguous steps selected at different phases of the experiment from one subject. This figure is meant to give a qualitative overview of steady-state changes that occur during different phases our experiment. Two colors show the median (open circles) and standard deviations (vertical lines) during 50 steps of corresponding experiment phases: the blue color is used for one leg, and the red color is used for the other leg. Note, for E4 phase, the median and std were obtained during early adaptation (EA). From E1 to E2 to E3, we see increase (decrease, resp.) in leg touchdown angle (leg liftoff angle, resp.). We see the leg touchdown angles being relatively similar during E3 and E4 (early adaptation); after adaptation, we see significant changes in leg touchdown and liftoff angles. E6 was unavailable for this particular experiment, hence empty. 136

LIST OF FIGURES

11.6 Transient response after perturbation from one subject. The solid red line is the mean of the trajectories corresponding to that run. The dashed red lines indicate \pm std's. The blue lines are simulations of the linear fit to transient responses; the simulation uses the mean data (red) for the initial condition. Notice the abscissa shows strides (not steps nor time). 137

11.7 Eigenvalues of the A_{CL}^{stride} matrix fitted to the bootstrapped data from E1, E3, and E5 of one subject. The first row shows a 3D histogram of the eigenvalues. The second row shows the data but using contours. 138

11.8 SLIP's closed-loop eigenvalue magnitudes (y-axis) as a function of adaptation rate η (x-axis). The system is stable when $0 \leq \eta < 0.8$ 141

Chapter 1

Introduction

Locomotion is defined as the act of moving from one place to another. While the definition of locomotion may seem simple, diverse and unique ways that animals achieve locomotion are truly astonishing and are anything but simple. A gecko *Gekko gecko* does not fall when running upside down on a ceiling because of the van der Waals forces between the ceiling and the gecko's hairy toes [4]. A mature termite *Nasutitermes corniger* uses its wings to fly in search of a mate to start a new colony; after finding a mate, the couple simply shed their wings because they no longer need to search for a mate [114]. Both an earthworm *Lumbricus terrestris* and a millipede *Illacme plenipes* burrow into the earth but the former does so without legs and the latter burrows with its more than 650 legs [69]. For army ants, locomotion is a collaborative effort where soldier ants form bridges or ledges with their bodies so that worker ants can quickly and safely travel across [41].

Biologists seek to identify general principles describing how these organisms move from one place to another. To successfully navigate and maneuver in a complex environment, animals extract salient sensory information, transduce this information into neural signals, and integrate them

CHAPTER 1. INTRODUCTION

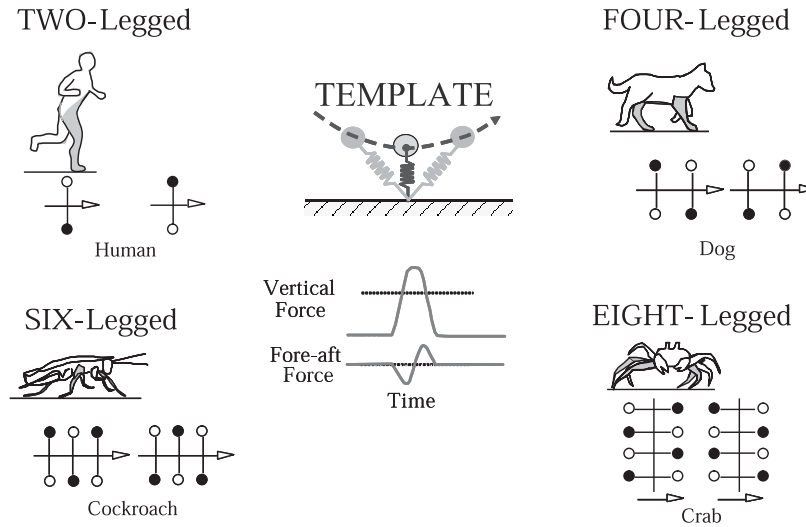


Figure 1.1: Animals of different shapes and sizes share similar qualitative vertical and fore-aft foot force patterns (shown in the middle of the figure). For each animal, stance legs (filled circle) and swing legs (open circle) are shown during two consecutive steps. The COM motion during each stance follows similarly as a SLIP. (Image credit: [50]; copyright ©2006 Society for Industrial and Applied Mathematics. Reprinted with permission. All rights reserved.)

with the dynamics of a locomoting musculoskeletal system. On the engineering side, we seek design inspirations for robust sensorimotor control strategies for robots that provide an environmental responsiveness to conditions outside of controlled laboratory settings. In this thesis, we seek to demonstrate how mutual, reciprocal inspiration can benefit both the neuromechanics and robotics fields. Specifically, we consider the following behaviors of two species: antenna-based wall following in American cockroaches (Part I) and split-belt treadmill running in humans (Part II). For both cases, we begin with mathematical representations (or models) of their body mechanics. Through biological and robotic experiments and computational simulations, we propose different control strategies that the animals might employ in response to perturbations, providing insights into their neural processing.

1.1 Modeling Musculoskeletal Body Mechanics

Legged locomotion results from complex, nonlinear, dynamically coupled interactions between an animal and its environment. Despite this complexity, simple patterns often emerge that are consistent with low-dimensional mechanical models [33]. Holmes et al. [50] suggest that animals of different shapes and sizes can have qualitatively similar force patterns in the vertical and horizontal planes. Figure 1.1 suggests that animals of different shapes and sizes can have qualitatively similar force patterns in the vertical and fore-aft directions.

We utilize the notion of *templates* and *anchors* [33, 50] to systematically formulate the synthesis of sensory, body, and neural controller dynamics; such a formulation makes the model amenable to formal mathematical analyses. A template is the simplest model that captures a specific behavior, while an anchor is a more complex, representative model of the behavior. Templates and anchors are not just “simple models” and “complex models”; there must be a natural embedding of the template behavior within the anchor [33].

In order to understand the complex body mechanics of running animals, researchers have simplified the problem by decoupling the mechanical models into the sagittal and horizontal planes. Horizontal plane locomotion in sprawled-posture animals is well characterized by the lateral leg spring (LLS) template (Fig. 1.2A; Section 3.1 and Chapter 6) [96, 97], because animals bounce side-to-side. Similarly, legged locomotion in the sagittal plane is consistent with a spring loaded inverted pendulum (SLIP) template (Fig. 1.2B; Chapter 10) [9, 16, 72, 101], a result that scales across the number of legs and three orders of magnitude of body mass [10, 30]. Surprisingly, both templates exhibit passive, dynamic stability when perturbed, thus requiring minimal neural feedback [2, 34, 95, 105]. The LLS template reveals that horizontal plane dynamics are asymptotically stable

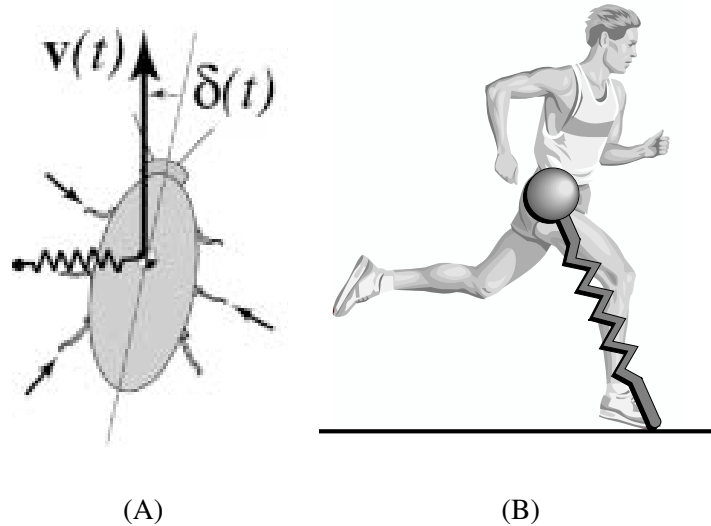


Figure 1.2: (A) Cockroach running is modeled in the lateral plane as a lateral leg spring (LLS) model (Section 3.1; [96]); the three stance legs, indicated by the three small arrows, are represented by a single *virtual* massless spring leg. (Image credit: [95]; with kind permission from Springer Science+Business Media:Figure 1(a) in [95]) (B) Human running is modeled in the sagittal plane as a spring-loaded inverted pendulum (SLIP). (Image credit: [100])

in all states except direction and speed, which are neutrally stable and thus both require active control [96, 97]. In this thesis, we use the LLS model as a motivation for our proposed antenna-based planar unicycle (APU; Chapter 4) and antenna-based LLS (ALLS; Chapter 6) models for cockroach wall following. For human running we use the SLIP model as our body mechanics template (Chapter 10).

1.2 Modeling Neural Control

In a popular book Gödel, Escher, Bach: An Eternal Golden Braid [49] written by D.R. Hofstadter, the author explains the operation of human brains using an analogy with electronic computers: In electronic computers, there are many layers of abstractions starting from silicon

CHAPTER 1. INTRODUCTION

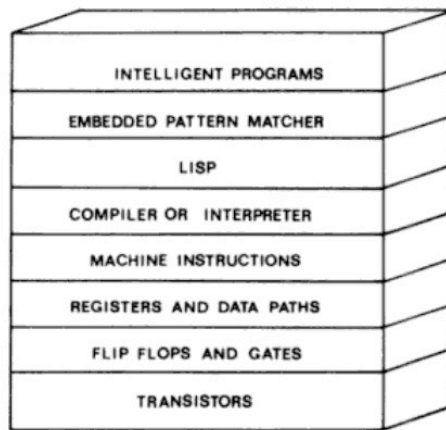


FIGURE 59. To create intelligent programs, one needs to build up a series of levels of hardware and software, so that one is spared the agony of seeing everything only on the lowest level. Descriptions of a single process on different levels will sound very different from each other, only the top one being sufficiently chunked that it is comprehensible to us. [Adapted from P. H. Winston, Artificial Intelligence (Reading, Mass.: Addison-Wesley, 1977).]

Figure 1.3: Layers of abstractions from transistors (hardware) to high-level programs (software). (Image credit: [49])

transistors up to high-level software programs (Fig. 1.3). Operations or instructions available in one layer come from abstractions created by “chunking” many operations from the layer below. The benefit of creating a series of abstract layers is that at the highest level, user-friendly programs (e.g., Matlab) can be written without the need to keep track of the details, say, at the transistor level. Similarly, our brains can employ many layers of these abstractions starting from neurons in the bottom-most layer that yield high-level operations or “intelligence” in the top layer.

Instead of a bottom-up approach where a synaptically-interconnected gross neural network model of biologically-relevant neurons are modeled, in this thesis, we take a “task-level” approach where we find the simplest control law (in the classical control theory sense) that abstractly represents the cockroach and human feedback control strategy during high-speed running. The models we present in this thesis are behavior specific and thus do not capture the complex dynamics—for example, for cockroaches, the switching between escape response and wall following—that may emerge out of more elaborated neural-network-based models [18]. However, the sheer complexity of their neural network hampers formal mathematical analysis (e.g., stability analysis) whereas our

CHAPTER 1. INTRODUCTION

approach elucidates the general functions of the neural network as a whole, nevertheless allowing one to predict how actual neural signals may look [21,22].

Part I

Cockroach Locomotion

Chapter 2

Motivation

Cockroaches demonstrate remarkable locomotor and navigational capabilities. American cockroaches (*Periplaneta americana*) can run up to 1.5 m/s (or 50 body lengths/s), even changing their gait to bipedal in order to attain high speeds [37]. When scaled for body length, this is equivalent to humans running at 200 mph! Furthermore, they can use their antennae as tactile probes to track a wall without visual cues (Figs. 2.1 and 4.7), following along the wall up to 80 cm/s [13,22]. They can also navigate changes in wall orientation up to 25 times/s and can begin to respond to a wall angle change in as little as 30 ms [13].

For such an extraordinary system, we seek to identify general principles about how the organism extract salient sensory information, transduce this information into neural signals, and integrate it with the tuned dynamics of a musculoskeletal system to successfully navigate in a complex environment. As a biological investigation, antenna-based wall following lends itself to mathematical modeling at several levels as well as behavioral and neurophysiological experimentation. This in turn gives us novel strategies for the design and control of antenna-based mobile robots.

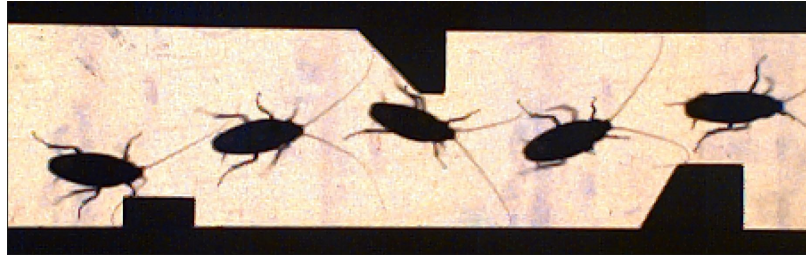


Figure 2.1: Top view of an *P. americana* running along a corridor with sensory obstacles.

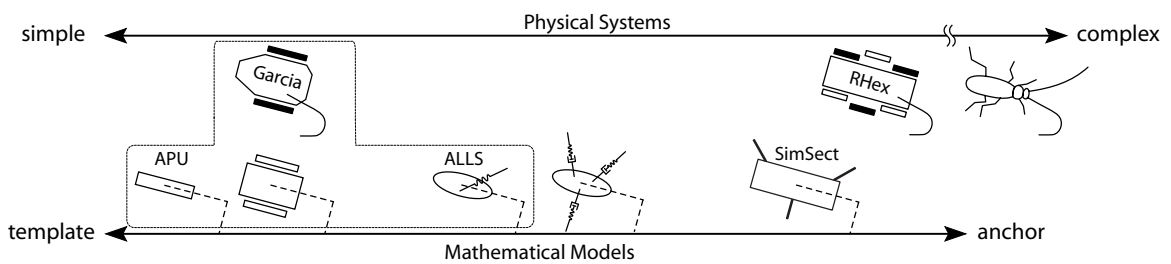


Figure 2.2: Our research program involves multiple levels of modeling, and biological and robotic experimentations. Here, we present three models: the antenna-based planar unicycle (APU, Chapter 4), a model for our Garcia robot (Chapter 5), and the antenna-based LLS (ALLS, Chapter 6). Importantly, each level of modeling admits the same control structure, including parameters (up to a scale factor), that was fitted to cockroach wall-following data (Chapter 4). The two physical systems involved in this study are *P. americana* (Chapter 4) and a differential drive mobile robot (Chapter 5). Eventually, we plan to extend our modeling effort to more elaborated anchors, such as the planar, multi-legged model proposed by Seipel et al. [104], or the spatial SimSect model developed by Saranli et al. [90] of RHex [91]. As well, we plan to extend our experimental robotics work to include a RHex-like six legged robot, endowed with an artificial antenna.

2.1 Roadmap

A schematic overview of our research program, which includes modeling, robotic development, and experimental biology, is depicted in Fig. 2.2. This thesis addresses the antenna-based task-level control of body angle using three models along the template–anchor axis and the results from robotic and ethological experiments.

In Chapter 4, we develop the antenna-based planar unicycle (APU) model (Section 4.1) to capture the antenna-based wall-following behavior of running cockroaches; from the APU model

CHAPTER 2. MOTIVATION

and tools from classical controls theory, we predict that the American cockroaches cannot use P (proportional) control alone (Section 4.2). In Section 4.3, we perform cockroach wall-following experiments; we refute (Section 4.4) the null hypothesis (cockroaches use only P control) and support the next simplest control law—PD (proportional-derivative) control.

In Chapter 5, we support the efficacy of the PD controller gains, found for the cockroaches (Section 4.4), in a *real-world* setting with unmodeled effects, including a flexible antenna and its friction with the wall, by implementing a robotics platform (Section 5.2.2) using the equivalent PD-gains (up to a scale factor; Section 5.2.3) and validating through physical experiments its overall stability (Section 5.3).

In Chapter 6, we develop an extension to the LLS model which captures the salient yaw dynamics of actual running cockroaches (Section 6.1); we show the efficacy of the PD-controller gains (Section 4.4) in a *legged* setting by implementing the PD gains on the antenna-based LLS (ALLS) model (Section 6.2) and validating its overall stability (Section 6.3).

We end Part I with a discussion (Chapter 7) of our results and a conclusion (Chapter 8). In the next chapter, we briefly review the lateral leg spring (LLS) model and provide a background in the behavior and body design of American cockroaches.

2.2 Dissemination

The majority of what is reported in this dissertation are from the following publications (with some corrections and added details):

- N. J. Cowan, J. Lee, and R. J. Full. “Task-level control of rapid wall following in the American cockroach.” *J. Exp. Biol.*, 209(9):1617–1629, 2006;
- J. Lee, A. Lamperski, J. Schmitt, and N. J. Cowan. “Task-level control of the lateral leg spring model of cockroach locomotion.” In M. Diehl and K. Mombaur,

CHAPTER 2. MOTIVATION

editors, *Fast Motions in Biomechanics and Robotics: Optimization and Feedback Control*, volume 340 of Lecture Notes in Control and Information Sciences, pages 167–188. Heidelberg: Springer-Verlag, 2006;

- J. Lee, O. Y. Loh, and N. J. Cowan. “A hierarchy of neuromechanical and robotic models of antenna-based wall following in cockroaches.” In *Proc. IEEE/RSJ Int. Conf. Intell. Robots Syst.*, pages 3547–3553, San Diego, CA, USA, October 2007;
- J. Lee, S. N. Sponberg, O. Y. Loh, A. G. Lamperski, R. J. Full, and N. J. Cowan. “Templates and anchors for antenna-based wall following in cockroaches and robots.” *IEEE Trans. Robot.*, 24(1):130–143, Feb. 2008.

Chapter 3

Background: American Cockroaches and LLS Model

American cockroaches *Periplaneta americana* (Fig. 3.1A and B), despite what their name suggests, originated in Africa and comprise one of the 47 species in the genus *Periplaneta* [85]. Adult cockroaches' body length averages about 4 cm (excluding their antenna). As shown in Fig. 3.1, cockroaches have six legs, two antennae (long, slender appendages on their head), and two cerci (short antenna-like sensors on the opposite ends of their bodies). One of the attributes of arthropods, such as *P. americana*, is their exoskeletons; unlike humans whose skeletal structure (endoskeletons or bones) is surrounded by muscles, arthropods have a hard cuticle skin (exoskeleton) that provides structure to the animal, and their muscles operate from the inside of the shell. To understand how these insects use their antenna to follow along a wall, we begin with a review of a model that captures the salient features of sprawled-posture insects' body mechanics: a lateral leg spring (LLS) model.



Figure 3.1: (A) Dorsal view of an American cockroach (*Periplaneta americana*). (Image credit: [58]) (B) A view of ventral side of *P. americana*. (Image credit: [119]) The two images are scaled to closely match the actual size of *P. americana*.

3.1 Review: Lateral Leg Spring (LLS) Model

Developed by Schmitt and Holmes, the lateral leg spring (LLS) models insect locomotion, specifically that of the cockroach *Blaberus discoidalis* [96, 97]. Cockroaches run using an alternating tripod gait [15]. Experiments have shown that the forces produced by this tripod of legs can be well represented by a single effective leg [32, 37]. Since the total mass of the legs of the insect is less than 6% of the total mass, the LLS model approximates each alternating tripod as a single massless, spring-loaded *virtual leg* that attaches to the midline of the body at a point called the center of pressure (COP). As illustrated in Fig. 3.2, the COP is offset from the center of mass (COM) by a displacement, d , where d may lie in front of the COM ($d > 0$) or behind the COM ($d < 0$). The model assumes that the foot pivots freely without slipping about its attachment to the ground, r_{foot} , and that the leg can rotate freely about the COP. This implies that no moments about the foot or COP can be generated, and forces will be applied to the body along the length of the

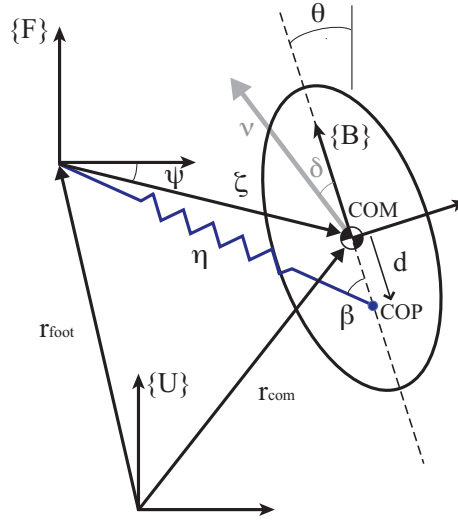


Figure 3.2: A schematic diagram of lateral leg spring model.

leg. A full stride for the model consists of a left and right step phase. A step phase begins with the relaxed spring extended at an angle $\pm\beta_0$ with respect to the body centerline. The body moves forward, compressing and extending the elastic spring, until the spring returns to its original length, at which point the leg is lifted, the next leg is placed down, and the cycle repeats.

Changes in the foot placements between left and right step phases result in a hybrid dynamical system. Systems with piecewise-holonomic constraints such as these can display asymptotic stability [86]. For gaits encountered in the LLS model, periodic motions exhibit neutral eigendirections due to energy conservation and $SE(2)$ invariance. Therefore, stability is partially asymptotic in the sense that perturbations to periodic orbits in the direction of the eigenvectors of conserved quantities and symmetries do not grow or decay, but simply result in movement to a different, stable gait. Gaits in the LLS model display partial asymptotic stability in the heading direction and angular velocity as a result of angular momentum trading between left and right step phases. The mechanical structure of the model therefore self-stabilizes the locomotion sys-

CHAPTER 3. BACKGROUND: AMERICAN COCKROACHES AND LLS MODEL

tem [96].¹ If $d < 0$ then the gaits are asymptotically stable in heading and angular velocity, i.e. the body approaches straight trajectories if the trajectory begins in the basin of attraction for the stable periodic orbit. If $d = 0$, the periodic orbits exhibit neutral stability in angular velocity and asymptotic stability in heading. If $d > 0$, periodic orbits are unstable. To show stability, one can take Poincaré sections at the beginning of a full stride, and numerically approximate the fixed points and eigenvalues of the linearized return map.

While the energetically conservative fixed and moving center of pressure models of [96, 97] reproduce many salient features of the kinematics and forces exhibited experimentally by *Blaberus discoidalis*, detailed comparisons illuminate limitations of the LLS. In particular, the fixed COP models previously investigated consider only COPs on the fore-aft body axis, and consequently only produce sinusoidal variations in θ ; in contrast, the animal produces cosinusoidal variations [115]. This is due to the fact that, under biologically plausible oscillations of the body orientation, a fixed COP located behind the center of mass along the fore-aft body axis is only capable of producing a positive or negative moment, rather than a moment that changes sign during each step phase. Additionally, fore-aft and lateral force profile magnitudes are typically reversed in comparison to those observed experimentally. Allowing the leg attachment point to vary from fore to aft in the moving COP model serves to address the qualitative discrepancies in the moment and yawing profiles [95]. However, while qualitatively correct yaw and moment profiles are produced by the model, quantitative comparisons reveal that the profile amplitudes in each remain an order of magnitude smaller than those observed experimentally. An activated muscle model introduced by Schmitt and Holmes [98] attempts to correct the moment and yawing oscillations by introducing hip

¹Together with the small amount of feedback required to detect the lift-off condition, and to detach the stance leg and attach the swing leg at the appropriately scheduled touch-down angle relative to the body.

CHAPTER 3. BACKGROUND: AMERICAN COCKROACHES AND LLS MODEL

torques and muscle activation. While these authors obtained moment profiles that matched those of actual cockroaches, they are obtained at the expense of increased model complexity and inverted fore-aft force profiles.

In this thesis, we use the LLS model as an “anchor” (discussed in Chapter 1) to develop even simpler representation of cockroach running: antenna-based planar unicycle template (Chapter 4). We come back to the LLS model in Chapter 6 to develop antenna-based LLS (ALLS) model. We show that a lateral placement of the COP produces the desired yaw dynamics without the need to move the COP during each stance phase (Appendix B).

3.2 American Cockroach: Antenna and Behavior

A cockroach antenna is composed of actuated joints at the base of the antennae, Fig. 3.3, between pedicle and scape and between scape and head, and the passive components called flagellum, which consist of ~ 150 small segments (Fig. 3.4). The flagellum is covered with various receptors that allow not only mechanoreception (touching or bending of the antenna) but also olfaction, taste, thermoreception, and hygrometry [102].

During slow exploratory behaviors, cockroaches actively sweep their antennae to provide rich information about their environment for self-orientation [76,77,78] and for slow-speed walking [28]. Basal receptors (Fig. 3.3), as opposed to flagellar receptors, initiate escape turns, while prior flagellar [20] or visual [120] stimuli either directly or indirectly influence the response.

Once elicited an escape response, rapidly running cockroaches use antennal feedback to follow surfaces with remarkable consistency, while holding the base of their antenna at nearly fixed angles relative to their body [13]. The dominant information for task-level control of this

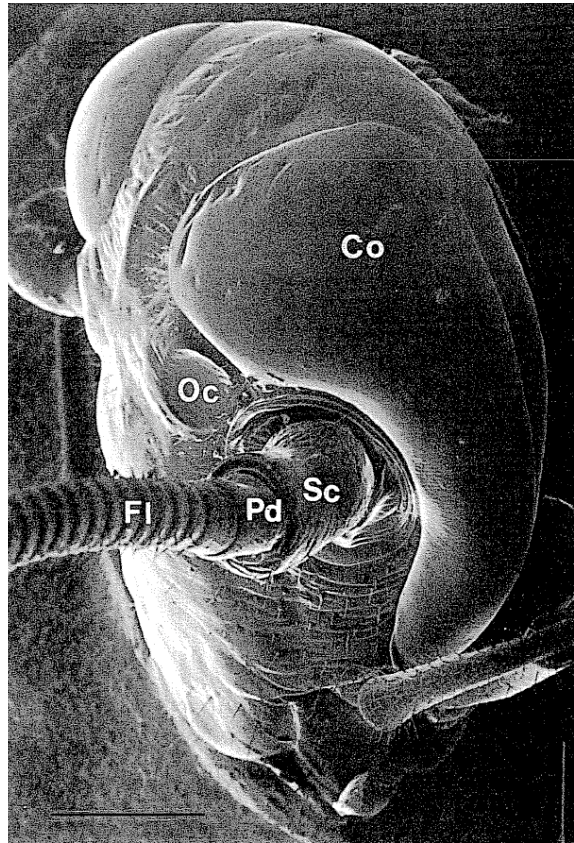


Figure 3.3: Scanning electron micrograph of *P. americana*'s head. Scale bar = 1000 μm ; Co: Compound eye; Fl: Flagellum; Pd: Pedicel; Oc: Ocellus; Sc: Scape. (Image credit: [102])

behavior originates from the flagellum (Fig. 3.4), with little-to-no contribution from the base of the antenna [13], though antenna base angle regulation likely requires basal proprioception. The long, passive, unactuated flagellum bends in response to objects in its environment and transduces contact and strain stimuli to neural impulses for control. Using this sensory input, cockroaches can execute quick wall-following maneuvers measuring up to 25 volitional body turns per second [13].

CHAPTER 3. BACKGROUND: AMERICAN COCKROACHES AND LLS MODEL

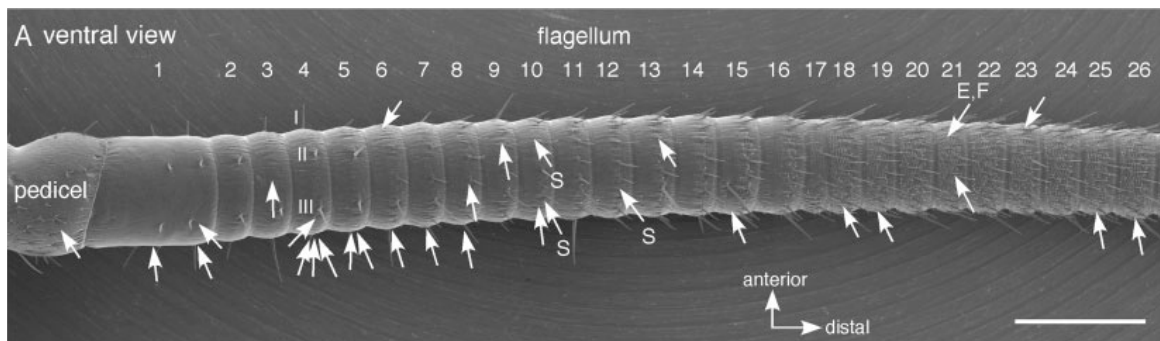


Figure 3.4: Scanning electron micrograph of *P. americana*'s antenna. Scale bar = 100 μm (Image credit: [74])

Chapter 4

Antenna-Based Planar Unicycle

In this chapter, we assume that control of rapid locomotion must be embedded in both neurosensory circuitry and an animal's mechanical system, and that a neuromechanical model of a sensory mediated behavior can lead to specific, testable hypotheses regarding afferent neural processing. From this assumption, we tested task-level control hypotheses using the antennal sensory system because of the behavior's effectiveness at high speeds, the ease of measuring performance, and the availability of well-developed mechanical models upon which we can build.

To build upon prior mechanical locomotor templates, we incorporate antennal sensing and neural control of running direction directly into one mechanosensory template of antenna-based wall following. In contrast to the LLS model, which aims to capture the within-stride dynamics of cockroach locomotion [95, 104], our model focuses on the multi-stride dynamics.

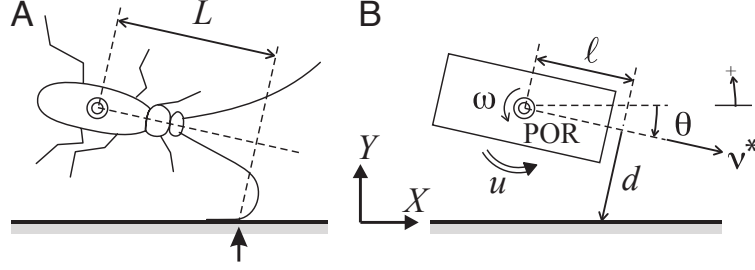


Figure 4.1: (A) Depiction of a cockroach following a straight wall. L is the farthest point ahead of the cockroach's point of rotation (POR), as measured along the body axis, that the antenna contacts the wall. The bold arrow at the bottom indicates the leading point on the antenna that is in contact with the wall. (B) Unicycle model of the running cockroach. The model parameters are ℓ , the preview distance; d , the antenna measurement; v^* , the forward running speed; θ , the angle of the cockroach body relative to the wall (positive is measured counter clockwise (CCW) for all angles, angular velocities and moments; note that $\theta < 0$ in this figure); $\dot{\theta}$, the angular velocity of the body; u , the moment applied by the legs about the POR. The preview distance ℓ may be less than L since the model does not account for neural and muscle activation delays. In the model, the angle of the POR velocity, ϕ , is the same as the body angle, θ , so ϕ is not shown for clarity.

4.1 Model: Antenna-Based Planar Unicycle (APU)

Consider a cockroach running on a horizontal flat substrate, following a straight vertical wall. The inertial frame's X-axis points along the wall, and the Y-axis points into the arena, as shown in Fig. 4.1. We model the cockroach as a planar rigid body. Let (x, y) denote the position of a point we call the point of rotation (POR). Let v^* denote the forward speed of the POR, and ϕ the velocity heading of the body POR, so that $(v^* \sin \phi, v^* \cos \phi)$ is the POR velocity vector. Denote the body angle by θ , and let $\omega = d\theta/dt$ denote the rotational velocity of the body. Cockroaches apply forces with their legs that keep the two angles θ and ϕ aligned during turning [54], therefore we model the body angle and the heading as coincident at all times, namely

$$\phi = \theta. \quad (4.1)$$

CHAPTER 4. ANTENNA-BASED PLANAR UNICYCLE

Under these modeling assumptions, the rigid body kinematics are given by

$$\begin{aligned}\dot{\theta} &= \omega \\ \dot{x} &= v^* \cos \theta \\ \dot{y} &= v^* \sin \theta\end{aligned}\tag{4.2}$$

where dot is used to indicate the time derivative, e.g. $\dot{x} = dx/dt$. At each instant, the body moves forward in the heading direction at speed v^* (assumed constant), while pivoting about the POR at angular velocity ω . The general robotics literature refers to this kinematic model as a “planar unicycle” [11].

We assume that the cockroach antenna measures the distance d from the body centerline to the wall (Fig. 4.1B) a fixed distance ℓ ahead of the body center, and we assume that the antenna is massless and does not impose force to its environment nor to the cockroach. Under these assumptions,

$$d = \ell \tan \theta + y \sec \theta.\tag{4.3}$$

Differentiating, and substituting the kinematics (4.2) yields

$$\begin{aligned}\dot{d} &= \dot{\theta} \ell \sec^2 \theta + v \tan \theta + y \dot{\theta} \tan \theta \sec \theta \\ &\approx \ell \dot{\theta} + v \theta \quad (\text{linearization}),\end{aligned}\tag{4.4}$$

or, in transfer function form,

$$\frac{D(s)}{\Theta(s)} = \frac{\ell s + v}{s}.\tag{4.5}$$

Equation 4.3 describes how the antenna measurement, d , changes as a function of the motion of the cockroach. We distinguish the model’s effective preview distance, ℓ , from the physical contact distance, L , which denotes the distance ahead of the animal that the antenna is touching the

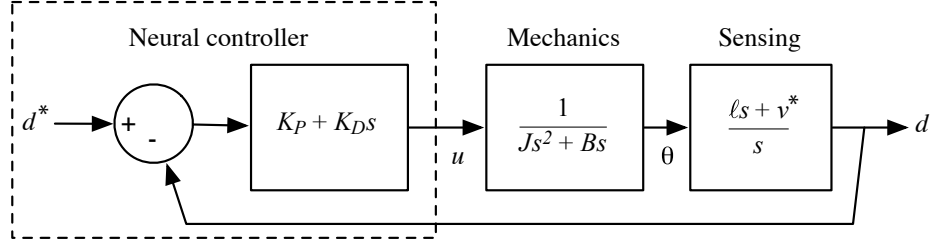


Figure 4.2: Block diagram of simplified control model. The “mechanics” box represents the torsional dynamics, and relates the body moment, u , to the body angle, θ . The “sensing” box is a simplified model of the antenna sensing kinematics, and it dynamically relates the cockroach angle, θ , to the antenna sensor measurement, d . We fit a simplified neural controller (in the dashed box), in which the error between a nominal “desired” wall-following distance, d^* , and the measured distance, d , is fed back through a PD controller. This control model enabled us to test PD control ($K_D \neq 0$) against P control ($K_D = 0$).

wall (Fig. 4.1A). The preview distance, ℓ , is based on the information available to the cockroach from a variety of potential mechanosensory receptors (e.g. campaniform sensilla, hair sensilla, and marginal sensilla). The antenna may encode distance, d , to the wall via a variety of surrogate signals such as contact point, strain, antennal forces, contact area, or bend, or some combination, that are all likely to be highly correlated with the distance to the wall during wall following. Finally, neural and muscle activation delays may decrease the effective preview distance (Section 4.2). To turn, a cockroach must generate a net polar moment, u [54]. The polar moment of inertia, J , and damping coefficient, B , parameterize the “yaw” dynamics,

$$J\ddot{\theta} + B\dot{\theta} = u. \quad (4.6)$$

Damping is used to model stride-to-stride frictional and impact losses. The animal does not run in a preferred direction, so we do not include a torsional spring force that would orient the animal.

Combining the two linear differential equations, (4.4) and (4.6), yields an open-loop dynamical system model of cockroach wall following. One can express a transfer function, $G(s)$,

CHAPTER 4. ANTENNA-BASED PLANAR UNICYCLE

between the moment, u , and the antenna measurement, d , as

$$G(s) = \frac{\ell s + v^*}{s} \cdot \frac{1}{Js^2 + Bs}. \quad (4.7)$$

The dynamical system model (4.4), (4.6) summarized by the linearized transfer function (4.7), has eight parameters, including the dimensionless angle, θ , and seven dimensional quantities: complex frequency, s ; head-to-wall distance, d ; input moment, u ; polar moment of inertia, J ; damping, B ; preview distance, ℓ ; and forward velocity, v^* . These reduce to four dimensionless groups: $\tilde{u} = u\ell/Bv^*$, $\tilde{J} = Jv^*/B\ell$, $\tilde{d} = d/\ell$, θ ; with $\tilde{s} = s\ell/v^*$, where \tilde{s} is the dimensionless complex frequency. Then, from (4.7) the dimensionless transfer function relating \tilde{u} and \tilde{d} can be written as

$$\tilde{G}(\tilde{s}) = \frac{\tilde{s} + 1}{\tilde{s}^2(\tilde{J}\tilde{s} + 1)}. \quad (4.8)$$

The dimensionless inertia

$$\tilde{J} = \frac{Jv^*}{B\ell} \quad (4.9)$$

plays an important role in our model since its value determines the ease of stabilization via closed-loop feedback (Fig. 4.2). If the cockroach uses negative feedback from the antenna-based distance measurement d , then \tilde{J} constrains the control structures that can stabilize the system.

Feedback Control: P Control The simplest possible feedback strategy, proportional feedback control (P control), assigns an input moment proportional to the “tracking error,”

$$u = -K_P(d - d^*), \quad (4.10)$$

where d^* is the steady-state distance that the cockroach neural control system attempts to maintain and K_P is the feedback gain. For stability, the poles (zeros of the denominator) of the closed-loop

CHAPTER 4. ANTENNA-BASED PLANAR UNICYCLE

system, $K_P G / (1 + K_P G)$, must have negative real parts. In nondimensional terms, the closed-loop poles are given by the solutions of the characteristic equation

$$\tilde{J}\tilde{s}^3 + \tilde{s}^2 + \tilde{K}_P\tilde{s} + \tilde{K}_P = 0, \quad (4.11)$$

where \tilde{K}_P is the dimensionless proportional gain. Routh's stability criterion (see [31]) reveals that the system is stable (i.e. the roots of (4.11) have negative real parts) if and only if $0 < \tilde{J} < 1$ and $\tilde{K}_P > 0$.

Feedback Control: PD Control We hypothesize (for reasons expanded upon in Section 4.2) that P control will not be sufficient to guarantee stability. To test our hypothesis, we fit a closed-loop model to a set of behavioral observations. The closed-loop model couples the dynamics of (4.2), (4.3), (4.4), and (4.6) with a proportional-derivative (PD) controller,

$$u = -K_P(d - d^*) - K_D\dot{d}, \quad (4.12)$$

where K_D is the gain of the derivative term, which encodes rate of approach to the wall. This additional derivative term helps to stabilize the system, allowing a greater range of allowable values for \tilde{J} . Note that setting $K_D = 0$ reduces the controller to P control. The nesting of models enables statistical hypothesis testing of the P-Hypothesis (null) against the PD-Hypothesis (alternative). During model fitting, we obtain estimates for ℓ , as well as the ratios K_P/J , K_D/J , and B/J . The resulting values enable us to estimate the dimensionless inertia, \tilde{J} .

4.2 Prediction: P Control Is Insufficient

The proposed controller for the planar unicycle demonstrates the necessary integration of mechanics and sensing during rapid running (Fig. 4.2). Stable control requires a consideration of

CHAPTER 4. ANTENNA-BASED PLANAR UNICYCLE

mechanics, sensing, and delay. Our simple PD-controlled unicycle model provides a mechanism to investigate these three components, which all contribute to the neuromechanical performance limitations inherent in wall following.

Our hypothesis that P control would be insufficient is motivated by root-locus analysis of the system $\tilde{G}(\tilde{s})$ in (4.8) under P control (4.10), as shown in Fig. 4.3. Under P control, for \tilde{J} near 1, two complex conjugate roots will dominate the response leading to large oscillations every time the cockroach encounters an angled wall. For a given gain \tilde{K}_P , the system becomes increasingly damped as \tilde{J} decreases. At the critical value $\tilde{J}_{\text{crit}} = 1/9$, the system can be critically damped with $\tilde{K}_P = 3$, with a triple root at $\tilde{s} = -3$. For any $\tilde{J} < \tilde{J}_{\text{crit}}$ and an appropriate choice of \tilde{K}_P the closed-loop system have one distinct real pole and one double real pole. This analysis leads to three distinct cases:

1. $\tilde{J} \geq 1$. The system cannot be stabilized with P control.
2. $\tilde{J}_{\text{crit}} < \tilde{J} < 1$, where $\tilde{J}_{\text{crit}} = 1/9$. For all choices of the gain K_P , the system will be under-damped and therefore oscillatory.
3. $\tilde{J} \leq \tilde{J}_{\text{crit}}$. The system can be stabilized with P control, and for an appropriate choice of K_P , the system can be either under damped, over damped, or critically damped.

Equation 4.9 indicates that \tilde{J} increases with speed. If \tilde{J} remains bounded below \tilde{J}_{crit} for behaviorally relevant speeds, then we would hypothesize that P control will be sufficient. If \tilde{J} exceeds unity (or even \tilde{J}), then we would hypothesize the need for a more complex compensation mechanism that includes adding velocity dependent feedback via a proportional-derivative (PD) controller (4.12).

Unfortunately, we cannot independently measure all of the parameters that determine \tilde{J} (4.9), and it would therefore seem impossible to make a prediction as to whether or not P control

CHAPTER 4. ANTENNA-BASED PLANAR UNICYCLE

is sufficient. However, one additional insight leads to the hypothesis that P control is insufficient: delay can destabilize a control system. Two separate calculations below predict that ethologically observed neural delays of 30 ms or more preclude P control for stability. As seen, our experimental results bear out this prediction.

A delay of T seconds, arising from neural processing and generation of muscular forces, adds a multiplicative term e^{-sT} to the open-loop transfer function $G(s)$ in (4.7):

$$G(s) = \underbrace{e^{-sT}}_{\text{delay}} \cdot \underbrace{\frac{\ell s + v^*}{s}}_{\text{antenna}} \cdot \underbrace{\frac{1}{Js^2 + Bs}}_{\text{mechanics}}. \quad (4.13)$$

The term e^{-sT} adds pure phase lag. This can be seen by evaluating e^{-sT} along the imaginary axis, along which it has unity gain and negative phase. Recall that lower values for \tilde{J} make P control possible, so assume for simplicity that $\tilde{J} = 0$. In this case, the delayed version of the dimensionless transfer function (4.8) simplifies to

$$\tilde{G}(\tilde{s}) = e^{-\tilde{s}\tilde{T}} \cdot \frac{\tilde{s} + 1}{\tilde{s}^2}, \quad (4.14)$$

where $\tilde{T} = Tv^*/\ell$ is the dimensionless delay. We use measured latency of approximately 30 ms for a cockroach to respond to an outward wall projection during wall following in *P. americana* [13]. That result nearly matches the latency of the antennal escape response for this species [120]. Since longer preview distances simplify control, we assume that the preview distance is $\ell = 4.5$ cm (which corresponds to the contact distances, L , that we measured). With these optimistic assumptions, as the running speed approaches the maximum observed running speed of *P. americana* of 1.5 m/s [37], the dimensionless delay approaches a critical value of $\tilde{T} = 1$, at which point the cockroach cannot be stabilized with P control for any choice of proportional feedback gain, K_P . This can be seen by using the Nyquist stability criterion (Fig. 4.4). A Nyquist plot is constructed by evaluating

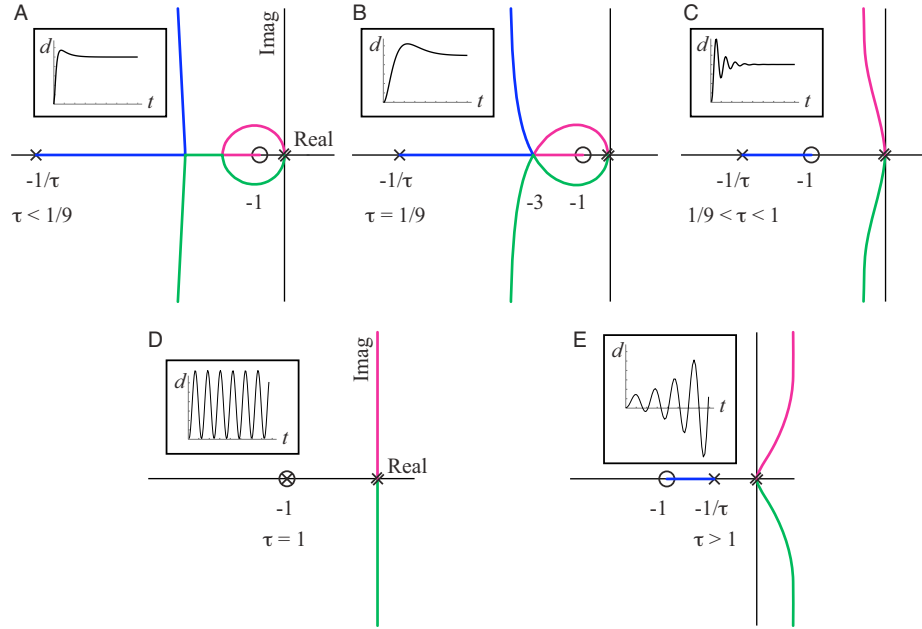


Figure 4.3: Root locus plots (see, e.g. [31]) of the transfer function of $\tilde{G}(\tilde{s})$ given by (4.8) for five characteristic values of the dimensionless inertia, \tilde{J} . Each plot depicts the locus of poles (roots of the denominator) of the closed-loop system (Fig. 4.2) under P control. The three open-loop poles (roots of the denominator of (4.8)) are indicated by X's, and therefore there are three branches of the root locus (magenta, green, blue). There is an open-loop zero (root of the numerator of (4.8)) at -1 , indicated by a circle. The small inset plot (d vs. t) for each root locus depicts a typical response of the hypothetical closed-loop system. For stability, all of the poles of the closed-loop system must be in the open left-half-plane, that is, they must have negative real parts. (A) For $\tilde{J} < 1/9$, all of the poles are in the left-half-plane; the inset shows an over-damped response of d vs. t . (B) For $\tilde{J} = 1/9$, the system would be critically damped with $K_P = 3$. (C) For $1/9 < \tilde{J} < 1$, the system would be underdamped under P control. (D) For $\tilde{J} = 1$, the system would be oscillatory for all choices in gain, K_P . (E) For $\tilde{J} > 1$, the system would be unstable. Since \tilde{J} approaches or exceeds 1 for behaviorally relevant running speeds (4.13), these graphs preclude the possibility of P control. Stability can be greatly improved by adding a derivative feedback term, as in (4.12), enabling larger values of \tilde{J} .

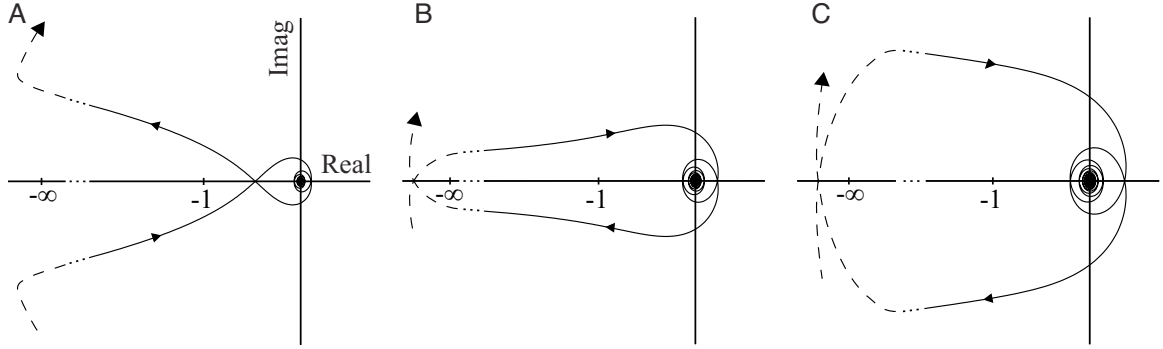


Figure 4.4: Three Nyquist plots of the system in (4.14) are shown for three characteristic values of the dimensionless neural delay, \tilde{T} , , assuming that $\tilde{J} = 0$. Delay cannot be handled using the root locus method; thus, we resort to Nyquist's stability criterion (see, e.g. [31]). (A) $\tilde{T} < 1$. (B) $\tilde{T} = 1$. (C) $\tilde{T} > 1$. Each plot is constructed by evaluating the transfer function in (4.14) along the imaginary axis. Because the open-loop system has no open right-half-plane poles, the closed-loop system is stable if the Nyquist plot does not encircle -1 on the complex plane. As can be seen, this is only possible for the case that (A) $\tilde{T} < 1$, whereas for (B-C) $\tilde{T} \geq 1$, there will always be at least two encirclements of -1, and thus at least two right-half-plane poles. Stability can be greatly improved by adding a derivative feedback term, as in (4.12), enabling larger values of \tilde{T} .

the transfer function (4.14) along the imaginary axis, namely $\tilde{G}(j\omega)$, from 0 to ∞ . Residue theory from complex analysis can be used to show that if this plot encircles the -1 point, the closed loop transfer function is unstable. In our case, for $\tilde{T} \geq 1$, the Nyquist plot always encircles the -1 point at least twice independent of the feedback gain; thus under P control the closed loop transfer function must have at least two unstable poles when $\tilde{T} \geq 1$. For values of \tilde{T} slightly lower than 1, P control will be highly oscillatory. Adding a velocity feedback component can mitigate this problem by adding phase lead which can counteract to some extent the phase lag introduced by the delay.

4.3 Experiment: Cockroach Wall Following

4.3.1 Animal Husbandry

Adult male American cockroaches *Periplaneta americana* L. were acquired from Carolina Biological Supply Company (Burlington, NC, USA) and housed in a ventilated plastic container. Cockroaches were exposed to a L:D cycle of 12 h:12 h and given fruits, vegetables, dog chow, and water *ad libitum*.

4.3.2 Wall-Following Arena

Our arena was similar to that used by Camhi and Johnson [13]. A rectangular arena, 85 cm \times 45 cm \times 15 cm (length \times width \times height), was enclosed with a corrosion-resistant aluminum sheet wall (Figs. 4.5 and 4.6). The upper half of the aluminum wall was coated with petroleum jelly to prevent the cockroaches from escaping. A long, high-density fiber (HDF) block, 50 cm \times 5 cm \times 5 cm, was used as a part of the observation wall to view the cockroach's wall following behavior. To induce turning, we placed HDF boards cut at angles of 30° and 45° in the middle of the first wall. Depending on where the cockroach started, it ran along either wall first using its right or left antenna for wall following. We noted this, but did not distinguish between the two scenarios for modeling. Henceforth, we refer to the wall that the cockroach initially tracks, either using their left or right antenna, as the control wall and refer to the wall that induces a turning behavior as the angled wall. The two walls collectively constitute the observation walls.

Two high-speed video cameras (Kodak EktaPro 1000, Eastman Kodak Company, Rochester, NY, USA) positioned approximately 1.5 m above the arena (Fig. 4.5A) captured the cockroaches' running behavior. A half-silvered mirror placed in front of each camera at 45° de-

CHAPTER 4. ANTENNA-BASED PLANAR UNICYCLE

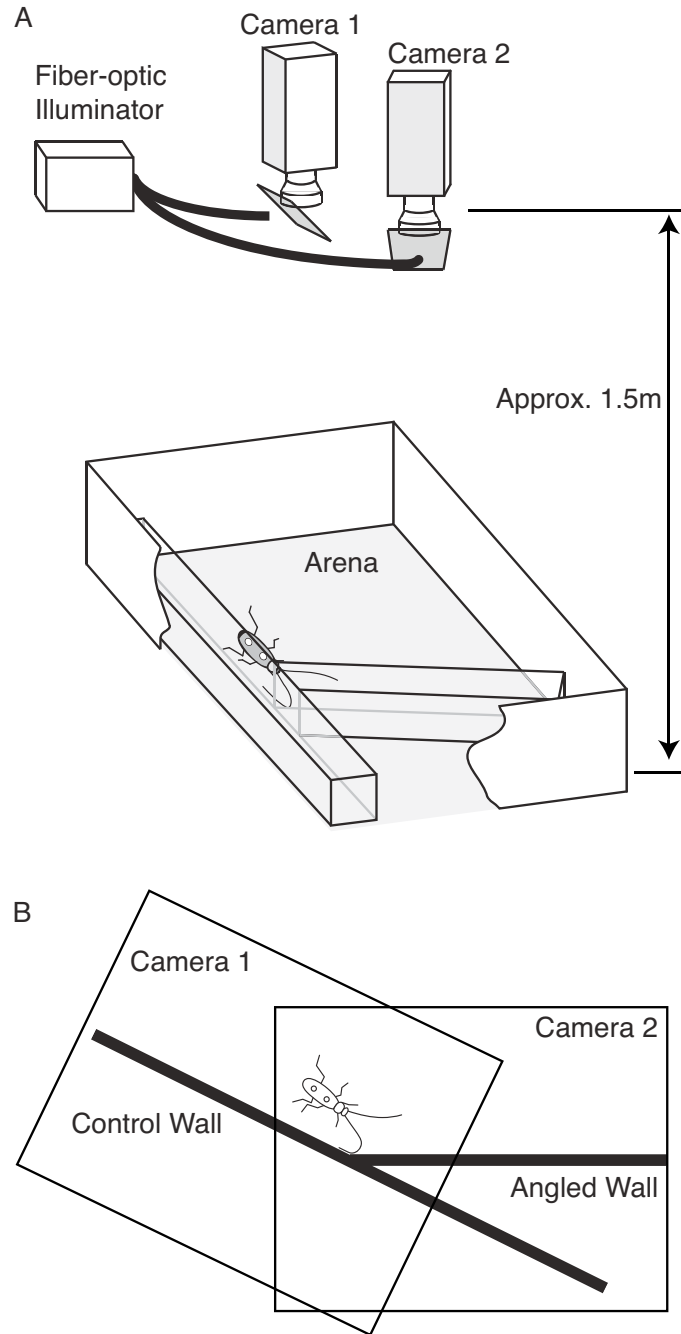


Figure 4.5: Illustration of wall-following arena viewed from side and from each camera. (A) Two high-speed cameras were positioned above an enclosed arena. The field-of-view of each camera was centered on an observation wall. Half-silvered mirrors in front of each camera reflected light from a fiber-optic illuminator onto the retroreflective running substrate, providing a stark silhouette of the cockroach despite very low ambient light. (B) The arena viewed from above showing the two cameras' overlapping fields of view.

CHAPTER 4. ANTENNA-BASED PLANAR UNICYCLE



Figure 4.6: Image of the wall-following arena illustrated in Fig. 4.5A. In this image, the room light is on to show the setup.

CHAPTER 4. ANTENNA-BASED PLANAR UNICYCLE

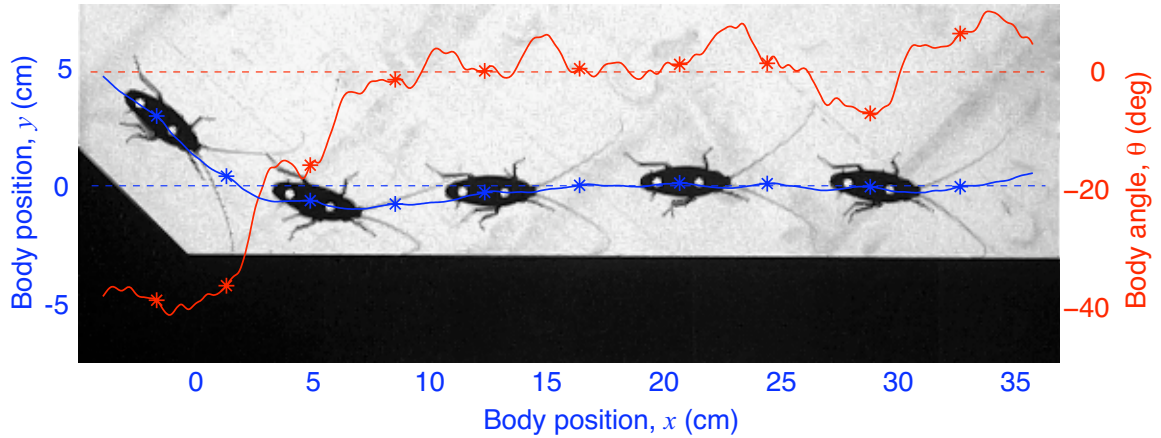


Figure 4.7: Multiple exposures of a cockroach running along an angled wall during a single trial.

flected light shone from a 150 W fiber-optic illuminator onto the running surface. There was little-to-no ambient lighting during the experiment. The two camera views of the observation walls overlapped slightly for camera calibration purposes and to ensure continuity of data from each trial (Fig. 4.5B). Each camera's field of view covered 35 cm in length of its respective wall, with an average resolution of 0.8 mm per pixel. The cameras synchronously captured images at 500 frames per second.

We captured video images (Fig. 4.7) of running cockroaches under low light using a retroreflective sheet from 3M (St Pauls, MN, USA) as the running substrate. Proper alignment of the lighting evenly illuminated the retroreflective running substrate and markers, simplifying detection and tracking of the cockroach, because the non-retroreflective walls, cockroach body and legs appeared as sharp silhouettes.

4.3.3 Animal Preparation

We prepared cockroaches inside a 4°C cold room as follows. After initially cooling the animals for 15-20 min, we anesthetized them using CO₂. While anesthetized, we attached two small round retroreflective markers to each animal's wings, approximately aligned with the body fore-aft axis, enabling us to estimate the cockroach's position and body angle from video images. The markers did not restrict the wings in any way. To block their visual senses, we covered their compound eyes and ocelli using a white nail polish, taking care to avoid the head/scape joint. This preparation process took less than 40 min per group of five cockroaches. After this preparation, the cockroaches recovered at room temperature for at least 24 h before testing.

4.3.4 Kinematics

Prior to a set of trials with a cockroach, we placed it in the arena for several minutes to acclimate. When the insect walked into position at the initial part of the control wall, we induced an escape response by tapping the running substrate with a long stick near the posterior of the cockroach. Trials were accepted when the animal ran rapidly along the wall and executed a turn at the angled wall. Trials were rejected when (1) the cockroaches stopped or climbed the wall while they were in view of the cameras, (2) the distance of their POR to the wall deviated by more than 2.5 cm while running along the angled wall; this typically occurred when the animal appeared to voluntarily leave the wall and run into the open space of the arena, (3) their body (excluding their legs) collided with the angled wall, or (4) their antenna was not in a "bent backward" posture when the antenna first encountered the angled wall; this eliminated trials in which the tip was pointing forward, thereby wedging the antenna in the corner.

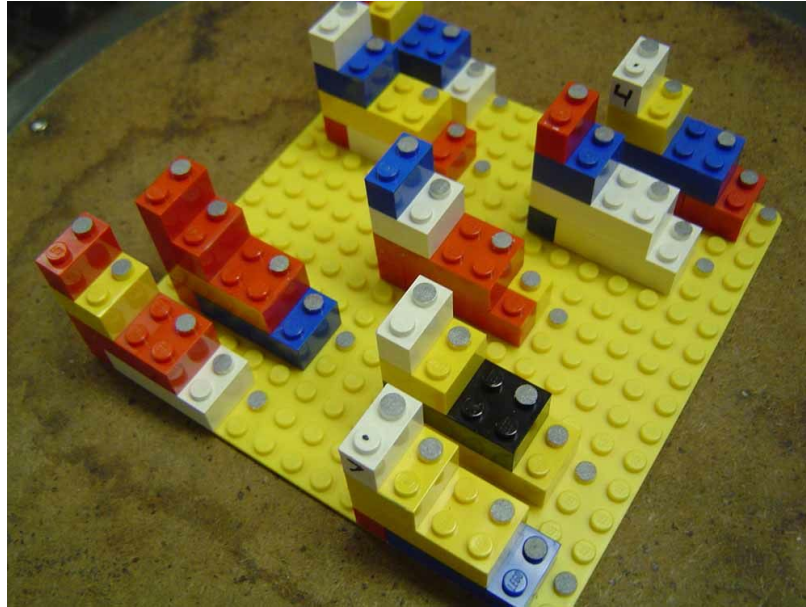


Figure 4.8: Three-dimensional lego blocks with retroreflective markers (gray circles). This object is placed in the arena in view of both cameras; the known relative marker positions and the markers seen from the cameras are used for camera calibration.

After each successful trial a cockroach rested for 2-3 min while we downloaded the recorded images to our workstation. When the animal stopped exhibiting the escape response from our perturbation or did not achieve any acceptable trials for 30 min, we switched to a different individual. An individual was never used for experiments twice in the same day.

Before each set of experiments, we captured an image from both cameras of a three-dimensional, non-coplanar block with retroreflective markers (Fig. 4.8). The geometry of the markers was measured with a set of digital calipers. Using these data, we calibrated the cameras using the direct linear transform.

We extracted four quantities from each trial. first, our custom scripts (Matlab, The Math-Works, Inc., Natick, MA, USA) tracked the cockroach's two body markers to obtain the body's POR (see below) and body angle, (x, y, θ) , for all frames (Fig. 4.7). We visually verified the tracking data

CHAPTER 4. ANTENNA-BASED PLANAR UNICYCLE

by superimposing the predicted marker measurements onto the raw images. Second, custom Matlab scripts automatically determined (and visual inspection confirmed) the frame number for each posterior extreme position (PEP) of the outside hindleg, contralateral to the observation wall. Third, we manually determined the time at which the antenna ipsilateral to the wall first came in contact with the angled wall. This time is the start time of the perturbation, $t = 0$. Fourth, we randomly selected 20 frames from which we manually digitized the antenna-wall contact points, 10 frames from the control wall and 10 frames from the angled wall. If the antenna was not in contact with the wall in the selected frame, a new frame was randomly selected. From these data, we obtained L (see Fig. 4.1A). The distance L provides an upper bound on the preview distance, ℓ (see Fig. 4.1B).

4.3.5 Finding the Point of Rotation

Since we modeled the cockroach as a unicycle, the 2-D position of the running cockroach was represented by its point of rotation (POR). To estimate the POR, we used the positions of the two retroreflective markers that were attached on the foreaft axis of the cockroaches wings. Assuming an ideal, no-slip unicycle, the following equation holds:

$$\alpha\omega = v^\perp, \quad (4.15)$$

where α is the distance between the POR and the rear marker, ω is the instantaneous rotational velocity, and v^\perp is the instantaneous velocity of the rear marker in the direction that is perpendicular to the heading (see Fig. 4.9). After approximating ω_i and v_i^\perp using two consecutive image frames, i and $i + 1$, we performed a least-squares fit to find the best α , i.e.

$$\alpha = \frac{\sum_{i=1}^{n-1} \omega_i v_i^\perp}{\sum_{i=1}^{n-1} \omega_i^2}, \quad (4.16)$$

where n is the total number of frames in a given trial, and thus found the POR.

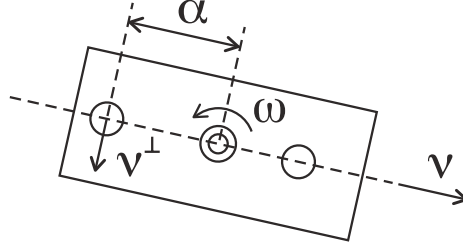


Figure 4.9: Instantaneous motion of the unicycle model. The two empty circles correspond to the two retroreflective markers that are used to finding the point of rotation locate the position of the POR (denoted as two concentric circles). v is the forward velocity; ω is the rotational velocity; v^\perp is the component of the velocity of the rear marker perpendicular to the body's fore-aft axis; α is the distance between the rear marker and the POR.

4.3.6 Data Filtering and Normalization

For each trial, we collected a time series of cockroach positions and angles spaced at 2 ms intervals. We zero-phase forward-filtered and reverse-filtered the data with a five pole, low-pass Butterworth filter with a cut-off frequency of 62.5 Hz, nearly three times the maximum observed frequency of angular motion [13] during wall following. The origin of the reference coordinate system coincided with the corner where the control wall met the angled wall, with X-axis parallel to the angled wall, pointing in the direction of running, and Y-axis perpendicular to the angled wall, pointing into the open arena.

Because our model (Fig. 4.1) inherently does not capture the detailed mechanics within each stride, we averaged the cockroach motion during each stride to estimate its state. We used the outer (contralateral to the wall) hind-leg PEP frame to segment the data into individual strides and averaged the data over each stride to obtain the values $(x_k^j, y_k^j, \theta_k^j, \omega_k^j, v_k^j, t_k^j)$, where $k = 1, 2, \dots$ indicates the stride number and $j = 1, \dots, N$ indicates the trial number. The position during the k th stride, (x_k^j, y_k^j) , was computed as the mean POR location over all frames of a given stride. Likewise, we computed the mean angle of the body axis, θ_k^j , during the k^{th} stride. We calculated

CHAPTER 4. ANTENNA-BASED PLANAR UNICYCLE

the speed, v_k^j , as the change in position of the POR between successive contralateral hindleg PEPs divided by the stride duration, $t_{k+1}^j - t_k^j$. Similarly we calculated the angular velocity, ω_k^j , as the change in angle divided by the stride period. The first stride ($k = 1$) for each trial was selected as the stride that began after the antenna first contacted the angled wall. The steady-state distance, d^* , was approximated for each trial by averaging the last three strides in view. We observed that most cockroaches had regained quasi-steady running by this point, which was typically at least 20 cm and at least 5 strides after the perturbation.

To test the model for speed dependent parameters, we segmented it into two groups, ‘slow’ and ‘fast.’ The average speed was computed for each trial as the mean of the individual stride speeds, v_k^j , for that trial. The fast group was comprised of trials whose average speed was greater than or equal to the median speed. The slow group were trials less than the median average speed. For each trial, the stride frequency was computed using the average time between successive outer hindleg PEPs.

For visualization purposes, we processed the data as follows. Each trial was normalized to distance traveled along the angled wall, with $x = 0$ corresponding to the point where the control wall meets the angled wall. This corresponds to the start time of the perturbation, $t = 0$, at $x = 0$. In all trials, x increased monotonically through the trial. The data were linearly interpolated with resampling at $x = 0, 0.1, \dots, 30.0$ cm resulting in a sequence of normalized observations (y_k^j, θ_k^j) , at the same x positions along the wall. Lastly, we grouped and averaged trials of similar speed, so that simulated trajectories could be compared with averaged actual trajectories.

4.3.7 Dynamic Model Fitting and Testing

To fit the parameters of our model we compared model simulations of each stride with the actual data from each stride, as follows. First, we combined the equations for the dynamics (4.6), antenna distance measurement (4.3), and PD-control input (4.12) into a single third order, nonlinear differential equation:

$$\begin{bmatrix} \dot{y} \\ \dot{\theta} \\ \dot{\omega} \end{bmatrix} = f_p(y, \theta, \omega) := \begin{bmatrix} v^* \sin \theta \\ \omega \\ -\frac{B}{J}\omega - \frac{K_P}{J}d - \frac{K_D}{J}\dot{d} \end{bmatrix}, \quad (4.17)$$

where

$$d = \ell \tan \theta + y \sec \theta, \quad (4.18)$$

$$\dot{d} = \omega \ell \sec^2 \theta + v^* \tan \theta + y \omega \tan \theta \sec \theta. \quad (4.19)$$

For convenience, we rewrite the last equation in (4.17) as

$$\dot{\omega} = -\hat{B}\omega - \hat{K}_P d - \hat{K}_D \dot{d} \quad (4.20)$$

where $\hat{B} \triangleq B/J$, $\hat{K}_P \triangleq K_P/J$, and $\hat{K}_D \triangleq K_D/J$. There are four independent parameters $p = (\ell, \hat{B}, \hat{K}_P, \hat{K}_D)$. Note that the position along the wall, x , can be omitted from the formulation.

We assume the parameters p and the speed v^* are constant during a trial. Given a set of parameters, p , and the cockroach state, $(y_k^j, \theta_k^j, \omega_k^j)$, at stride k of trial j , the flow, Φ , predicts the state of the cockroach during the subsequent stride:

$$\begin{bmatrix} \hat{y}_{k+1}^j \\ \hat{\theta}_{k+1}^j \\ \hat{\omega}_{k+1}^j \end{bmatrix} = \Phi_{\Delta t_k^j}^{f_p}(y_k^j, \theta_k^j, \omega_k^j), \quad (4.21)$$

CHAPTER 4. ANTENNA-BASED PLANAR UNICYCLE

where the “hatted” quantities, $(\hat{y}_{k+1}^j, \hat{\theta}_{k+1}^j, \hat{\omega}_{k+1}^j)$, are model estimates for the subsequent stride of the same trial, and $\Delta t_k^j = t_{k+1}^j - t_k^j$ is the stride duration. We evaluated the flow (4.21) by simulating the dynamics (4.17) for the full duration of a stride (using fourth order Runge-Kutta O.D.E. integration) obtain the prediction of the state at the next stride of the same trial. We assumed the residual error, $(\hat{y}_{k+1}^j, \hat{\theta}_{k+1}^j) - (y_{k+1}^j, \theta_{k+1}^j)$, between the model and the measured cockroach position and angle was an independent and identically distributed Gaussian noise process with zero mean and unknown covariance. This assumes that each stride is an independent sample for nonlinear regression. We fit the full nonlinear dynamics, rather than the linearized dynamics, since our perturbations included relatively large angles (up to 45°). After the antenna had first contacted the angled wall, only the first four stride-to-stride transitions ($k = 1, 2, 3, 4$) were considered for each trial, because after that point, most animals had almost fully recovered from the perturbation, and including more strides amounted to fitting small fluctuations that occurred during straight wall following. To fit the parameters of the controlled mechanosensory system, we followed the nonlinear statistical modeling framework described by [38].¹ We used Gauss-Newton optimization to minimize the least-squares error between the observed stride states, and the stride-to-stride predictions thereof, namely

$$\hat{p} = \arg \min_p \sum_{j=1}^N \sum_{k=1}^4 \begin{bmatrix} \hat{y}_{k+1}^j - y_{k+1}^j \\ \hat{\theta}_{k+1}^j - \theta_{k+1}^j \end{bmatrix}^T \hat{M}^{-1} \begin{bmatrix} y_{k+1}^j - y_{k+1}^j \\ \hat{\theta}_{k+1}^j - \theta_{k+1}^j \end{bmatrix} \quad (4.22)$$

where N was the number of trials used for fitting (with four strides per trial), and \hat{M} is the estimated noise covariance matrix [38]. For computing confidence intervals ($P = 0.05$ significance), we

¹ Gallant’s approach allows us to find the best fit for the parameters $p = (\ell, \hat{B}, \hat{K}_P, \hat{K}_D)$, while accounting for how random variations in the trials lead to uncertainty in the parameters. This is analogous to linear regression, e.g. fitting a line $y = mx + b$. Here, our “ x ” data are the states at the start of each stride, and our “ y ” data are the states at the end of each stride; the slope and intercept in linear regression are analogous to our unknown parameters, p . As is well known in linear regression, random fluctuations in the data affect parameter variances, and we arrive at similar results here, in a nonlinear setting.

CHAPTER 4. ANTENNA-BASED PLANAR UNICYCLE

assumed $4N - 4$ degrees of freedom ($4N$ independent state transitions and 4 fitted parameters). Because our goal was to test the overall model structure and the importance of derivative feedback for control, we did not fit the parameters to each individual animal. Moreover, doing so may be experimentally infeasible due to the large number of successful trials that are required for fitting. Thus, we fit all of the data simultaneously, and then divided the data into two groups by speed to determine if control system parameters were speed dependent. We also checked for very large variations between individuals by rerunning the statistics with data from each individual omitted. Because P control results from simply setting $K_D = 0$ in (4.12), the P-control and PD-control hypotheses can be written

$$H_P : K_D = 0 \quad (4.23)$$

$$H_{PD} : K_D \neq 0. \quad (4.24)$$

We tested the hypothesis H_P against the alternative H_{PD} using a nonlinear version of the Student's t-test with $4N - 4$ degrees of freedom and $P = 0.05$ significance.

4.4 Results and Discussions

We accepted a total of 59 trials from 11 individual cockroaches (mass= 0.770 ± 0.113 g, body length= 3.70 ± 0.17 cm, antenna length= 4.36 ± 0.41 cm, shortest antenna= 3.81 cm, longest antenna= 4.91 cm, means \pm s.d.). The speeds ranged from 24.7 to 63.6 cm/s (7 – 17 strides/s), all of which were above that of metachronal walking [117], and below the speeds for which four- and two-legged running emerges in *P. americana* [37]. Therefore the stepping pattern was consistent for all speeds in the study: the animals always exhibited an alternating tripod gait [25].

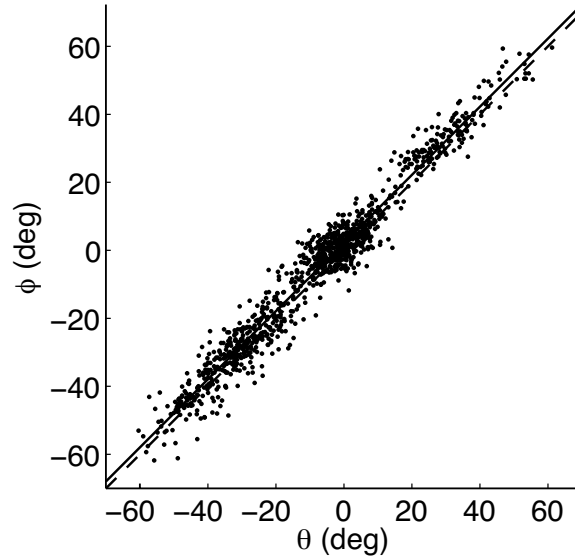


Figure 4.10: Relationship between stride-averaged ϕ and θ . Each data point consists of the averaged ϕ and θ values during a stride. We analyzed 1079 strides observed in 59 trials from 11 individuals. The best fit line (solid line) and the model, $\phi = \theta$ (broken line), are both shown.

4.4.1 Model Validation

The planar unicycle assumption requires (4.1) to hold, namely $\phi = \theta$. To validate this assumption, we performed a least-squares fit of the stride-averaged ϕ and θ to the linear model, $\phi = \beta_1\theta + \beta_0$. The result was $\beta_1 = 1.00 \pm 0.01$ and $\beta_0 = 2.18 \pm 30^\circ$ ($P = 0.05$), with an R^2 of 0.96 (see Fig. 4.10). The non-zero value of β_0 may have resulted from the inconsistencies in the placement of the two visual markers along the foreaft axis of the cockroach's body. Alternatively, occasionally, the cockroaches exhibited a wedging behavior during which they ran at a slight angle toward the observation wall.

4.4.2 P Control Is Insufficient

Table 4.1 shows the results of model fitting. For both slow running (35.2 ± 3.8 cm/s, 7 – 13 strides/s, 29 trials) and fast running (48.3 ± 6.0 cm/s, 10 – 17 strides/s, 30 trials), the null

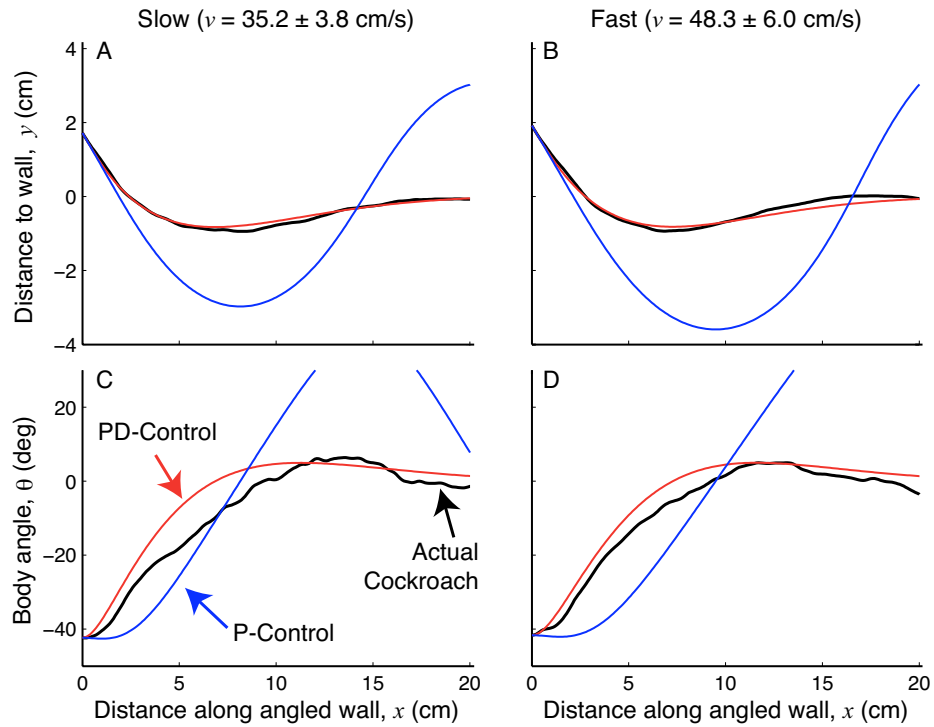


Figure 4.11: Average cockroach distance to the wall y (A,B) and body angle θ (C,D) as a function of distance traveled along the 45° angled wall for two different speed groups (Slow A,C and Fast B,D). The actual cockroach data (black) is compared to predictions from the PD-control model (red) using the parameters from Table 1. To show the importance of the derivative gain, K_D , we tested the controller with the $K_D = 0$ (P control, blue); note that for P control, performance degrades with increasing speed as expected. The derivative gain significantly improved the fit for the speeds tested.

Table 4.1: Parametric fit for PD-control models

Speed group	Speed (cm/s)	ℓ (cm)	\hat{B} (s^{-1})	\hat{K}_P ($s^{-2}cm^{-1}$)	\hat{K}_D ($s^{-1}cm^{-1}$)	Reject P-Control hypothesis?
Slow (N=29)	35.2 ± 3.8	2.71 ± 5.30	12.7 ± 16.4	26.0 ± 13.2	4.33 ± 3.29	Yes ($P = 0.01$)
Fast (N=30)	48.3 ± 6.0	2.55 ± 6.79	10.6 ± 37.7	25.1 ± 14.8	6.18 ± 3.30	Yes ($P < 0.001$)
All (N=59)	41.9 ± 8.3	1.78 ± 3.46	16.1 ± 17.7	27.0 ± 10.1	5.63 ± 2.05	Yes ($P < 0.001$)

CHAPTER 4. ANTENNA-BASED PLANAR UNICYCLE

hypothesis H_P was strongly rejected in favor of H_{PD} (t-test; slow: $P = 0.01$; fast: $P < 0.001$). Figure 4.11 shows the average trajectory of a cockroach when encountering a 45° angled wall, in addition to the model simulation. Here the model simulation trajectory is generated by simulating the fitted model using only the initial condition of the averaged data trajectory. This is different from stride-to-stride predictions (4.21) we make to find the parameters for the model. The general agreement between the simulated trajectory and the averaged cockroach data suggests that salient frequencies in the data are captured by our fitting technique [66]. To see the importance of the derivative gain, K_D , we tested the model with $K_D = 0$. In this scenario, the model predicts large excursions of the cockroach that would cause successive collisions with the wall interleaved with large departures into the open space, which is quite atypical. Clearly, the derivative gain in the model is behaviorally critical. When data from each individual were in turn omitted, there was no statistically significant difference in the parameters, so we concluded that any outlier effects were negligible. It was not possible to fit the model parameters to a single individual due to the large number of trials required to perform an accurate fit of the parameters.

There was no statistically significant dependence of the model parameters on speed, so we also fit all 59 trials 41.9 ± 8.3 cm/s simultaneously to the model, which decreased the 95% confidence intervals of the parameters. The R^2 value was 0.75. Again, H_P was strongly rejected in favor of H_{PD} (t-test, $P < 0.001$).

The model's effective preview distance, ℓ , is based on the information available to the animal from mechanosensory receptors along the antenna. Therefore, the contact distance, L , measured along the body axes from the POR to the farthest antenna-wall contact point, provides an approximate upper limit for the antenna preview distance. The preview distance will likely be shorter

CHAPTER 4. ANTENNA-BASED PLANAR UNICYCLE

than the contact distance due, for example, to delays. We randomly selected and manually digitized this contact point for 20 frames from each accepted trial. The contact distance averaged over all slow trials, $L_{slow} = 4.72 \pm 0.65$ cm, and fast trials, $L_{fast} = 4.40 \pm 0.53$ cm, were significantly different ($P = 0.04$, one-way analysis of variance). As the cockroach ran faster, the antenna contact distance decreased because the animal ran closer to the wall [13], and/or experienced increased drag of the antenna against the wall at higher speeds.

As another test of the P-control hypothesis, we directly fit the model with only three free parameters $p = (\ell, \hat{B}, \hat{K}_P)$, using the same approach as before. This pure P-control model proved inadequate because the best preview distance ($\ell = 9.29 \pm 2.95$ cm) was significantly longer than the values for L we observed for fast and slow running, and also significantly longer than the longest antenna length for any of the individuals we tested. Therefore we reject the simplistic P-control model in favor of the PD-control model, which better captures the data, and does so with physically realistic parameters.

4.4.3 Basis of Planar Unicycle Model

Our model for running is most similar to a unicycle viewed in the horizontal plane (Fig. 4.1). The planar unicycle takes advantage of the unique performance of the lateral leg-spring (LLS) model [96, 97] (see Section 3.1), allowing for simple control of body angle. The LLS model has been remarkably effective in modeling the dynamics of cockroach running [62, 96, 95, 98]. It consists of a rigid body that bounces from side-to-side as it moves forward with a pair of virtual leg-springs representing the summed behavior of an animal's legs. The leg-springs are attached at a fixed (or moving) point called the center of pressure. Six states describe the LLS: the center-of-mass position (x, y) , body angle θ , velocity ω , forward speed v^* , and the COM velocity heading

CHAPTER 4. ANTENNA-BASED PLANAR UNICYCLE

relative to the body axis, δ . Schmitt and Holmes’s analysis [96, 97] that for a wide range of center-of-pressure locations (for example, fixed behind the COM), the discrete stride-to-stride dynamics partially asymptotically self-stabilize to an isolated equilibrium point in both angular velocity and relative heading. In other words, if an external force slightly perturbs steady-state running, those two variables return to steady state as a result of mechanical feedback [35]. Stability results from losses and gains of angular momentum incurred in leg-to-leg transitions with minimal sensory feedback. In addition, the forward speed and body angle are neutrally stable, so that small perturbations might slightly increase or decrease the speed or send the model off in a somewhat different direction, but they will asymptotically acquire the new steady-state after the perturbation.

Our unicycle model captured the overall trajectories of cockroaches by utilizing the within-stride dynamics responsible for much of the passive self-stability of the LLS model [96, 97]. Specifically, in our planar unicycle, the stride-averaged body axis angle remained coincident with the POR’s velocity vector. We reduced the passively stable relative heading of the LLS model to an algebraic constraint, $\delta = 0$, a simplification supported by our data when averaged over each stride (Fig. 4.10). We added rotational damping to cause the angular velocity to decay to zero after perturbations, enabling the body angle to reach a new steady direction, much like the LLS model predicts. Because our objective was to capture the angular dynamics of antenna-based control, we made one further simplifying assumption—the animal holds its forward speed constant. To enable task-level control of the otherwise neutrally stable body angle, θ , we incorporated into our model an input moment, u , about the POR, and an antenna that measures distance, d . Finally, we assumed that a PD controller linked the measurement, d , to the input moment, u (Fig. 4.2). We then fit this control model to data experimentally to determine the parameters of the model. This enabled us to

test whether velocity feedback information was necessary for control.

4.4.4 Alternative View of the Effects of Delay

We suggest a different perspective (compared to Section 4.2) on the role of delay by assuming that the delayed signal simply decreases the preview distance. This alternative explanation leads us to the same conclusion as with Section 4.2 that P control is insufficient. One might reasonably expect the preview distance to vary according to

$$\ell \approx L - v^*T$$

where L is the maximum contact distance. In other words, the faster the cockroach runs, the less the effective preview distance due to the delay. Recalling that $\tilde{J} = Jv^*/B\ell$, we expect that

$$\tilde{J} \approx \frac{Jv^*}{B(L - v^*T)} \quad (4.25)$$

Again we assume $T = 30$ ms. As *P. americana* approach their maximum speed 1.5 m/s, \tilde{J} approaches infinity, independent of the specific values of J and B . For speeds far less than the maximum, $\tilde{J} > 1$. This supports the notion that P control will fail as an adequate explanation for control at behaviorally relevant running speeds. Moreover, as the animal increases in speed, the need for a more complex control mechanism will increase. At a running speed of $v^* = 42$ cm/s (the average speed of the fast group of cockroaches) a delay of at least $T = 30$ ms will reduce the preview distance by at least 1.3 cm. Thus, if $L = 4.4$ cm (the average value for fast trials), the preview distance should be at most 3.1 cm. This is slightly longer than our experimentally fitted value of $\ell = 2.6$ cm for fast trials (Table 4.1), and therefore it is feasible.

Because v^* is measured and ℓ and \hat{B} are fitted (Table 4.1), we can calculate the nominal value for \tilde{J} using the formula $\tilde{J} = v^*/\hat{B}\ell$ for each speed group. Based on the best-fit PD-control

CHAPTER 4. ANTENNA-BASED PLANAR UNICYCLE

parameter, at slow speeds, \tilde{J} is given by

$$\tilde{J}_{slow} = 1.02$$

while the value for fast running is

$$\tilde{J}_{fast} = 1.79.$$

Figure 4.11 (B,D) shows that P control cannot stabilize the behavior at high speeds, because $\tilde{J}_{fast} > 1$. PD control is required and we would predict that neural signals from antennae will show a distinct phasic response corresponding to velocity feedback. At the slow speeds tested, however, P control may be possible, since $\tilde{J}_{slow} \approx 1$, but with P control the cockroach wall-following dynamics would be very highly oscillatory no matter what the choice of gain, K_P (Fig. 4.11 (A,C)). One expects \tilde{J} to decrease further at slower speeds, and at the slowest speeds the system would be easily controlled by simple P control. While we suspect that to be the case, we did not test such speeds; for consistency, we used the escape response behavior to elicit running, so the slowest trials captured for this study were those with continuous non-stop running at over 20 cm/s. This is distinct from the more intermittent walk/pause style walking seen during exploratory locomotion described by [42], and examined (along with fast runs) for wall following by Camhi and Johnson [13]. To test whether P control suffices at these slow speeds one would need to model the intermittent walking behavior, which is beyond of the scope of the present study.

The data and analyses presented in this thesis refute the P-controlled dynamic unicycle model of wall following, and support (though do not prove) a simple alternative, a PD-controlled dynamic unicycle. The PD-controlled model matches the data and, according to the theoretical analysis, enables stable wall following. Our experimental and theoretical observations do not preclude more complex and elaborate alternatives. For example, acceleration feedback may also play

CHAPTER 4. ANTENNA-BASED PLANAR UNICYCLE

a critical role in some circumstances (though a more elaborate set of perturbations may be needed to tease this out). Our controlled experiments also do not support or refute more complex neural transfer functions that might be required for following more complex surfaces or avoiding isolated obstacles.

4.4.5 Multimodal Role of Antennae in Mechanosensory Integration

Behaviors mediated by antennal feedback involve a complex combination of basal and flagellar mechanoreceptors, not to mention feedback from myriad other sensory stimuli, including vision [120] and olfaction [94]. Understanding of the neural control strategies underlying sensorimotor function is further confounded by the need to identify the behavioral context, such as wall following and random exploration [53], wind following [12], and tunneling versus climbing [45].

We believe that understanding task-level neural control of rapid running requires the integration of sensing and mechanics. A neuromechanical model opens up a wide range of tools from control theory—such as root locus analysis and Nyquist’s stability criterion—to make specific predictions regarding neural function. The neural processing requirements for stability derived from such a neuromechanical model lead to novel, testable motor control predictions. In this chapter, we employed a simple neuromechanical model of wall following that predicts the need for neural coding of both antennal distance (proportional) and velocity (derivative) for stable wall following. Based on the results in this thesis, our prediction would be to see both a tonic response (position) and a phasic response (velocity) of antenna perturbations (Section 7.3).

Chapter 5

Robotic Integration of Bio-Inspired Antenna

In this chapter, we report the integration of a custom artificial antenna with a mobile robot platform to test the efficacy of using the APU as a template model for our biological system. Since Sponberg et al. [108] (Section 7.3) suggest that sensory signals encoding distance-to-wall, d , and its rate, \dot{d} , may indeed be available for cockroaches, we test whether the same PD-controller gains (up to a scale factor) that are fitted in Chapter 4 are sufficient for stable wall following in our robotic platform despite effects such as antenna-to-wall friction and non-trivial forward speed dynamics. A positive result would indicate the sufficiency of the PD controller—including the specific gains fitted to the cockroach—despite the APU model neglecting many complexities inherent to real-world antenna-based wall following.

5.1 Garcia Robot

Our physical instantiation of the unicycle-like robot is called Garcia (Acroname, Inc., Boulder, CO, USA) shown in Fig. 5.2. It is a three-wheeled robot, with two drive wheels sharing the same axis of rotation and a third passive omni-directional wheel, with zero caster sweep space, for balance. This machine was used previously by Lamperski et al. [60] to demonstrate the feasibility of wall following using a multi-rigid-linked antenna as its distance sensor. An on-board XScale ARM processor updates our control law at 50 Hz using sensory information from the antenna. During each trial, we log internal states such as the voltages from the four flex sensors (and hence the perceived distance to the wall) and the encoder-measured velocities of the two wheels. In addition, we use an overhead camera to obtain the ground-truth position of the robot for post analysis.

The primary difference between the theoretical unicycle model and the Garcia robot is the need for forward velocity control. Lamperski et al. [60] has shown that the dynamical equations for the robot are of the form

$$\begin{bmatrix} \dot{v} \\ \dot{\omega} \end{bmatrix} = \mathbf{A} \begin{bmatrix} v \\ \omega \end{bmatrix} + \mathbf{B} \overbrace{\begin{bmatrix} V_1 \\ V_2 \end{bmatrix}}^u, \quad (5.1)$$

where

$$\mathbf{A} = \begin{bmatrix} -\gamma & 0 \\ 0 & -\hat{B} \end{bmatrix}, \quad \mathbf{B} = \begin{bmatrix} b_1 & b_1 \\ -b_2 & b_2 \end{bmatrix}.$$

Here, V_1 and V_2 are the input voltages for the left and right wheels, respectively, v is the forward speed, and ω is the angular velocity of the robot. The parameters $\hat{B}, \gamma, b_1, b_2 > 0$ are expressed in terms of the armature resistance, the torque constant, the back electromotive force constant, a frictional damping constant for each wheel, the wheel radius, the lateral offset of each wheel from the center, the robot's moment of inertia in the yaw direction, the moment of inertia of each wheel,

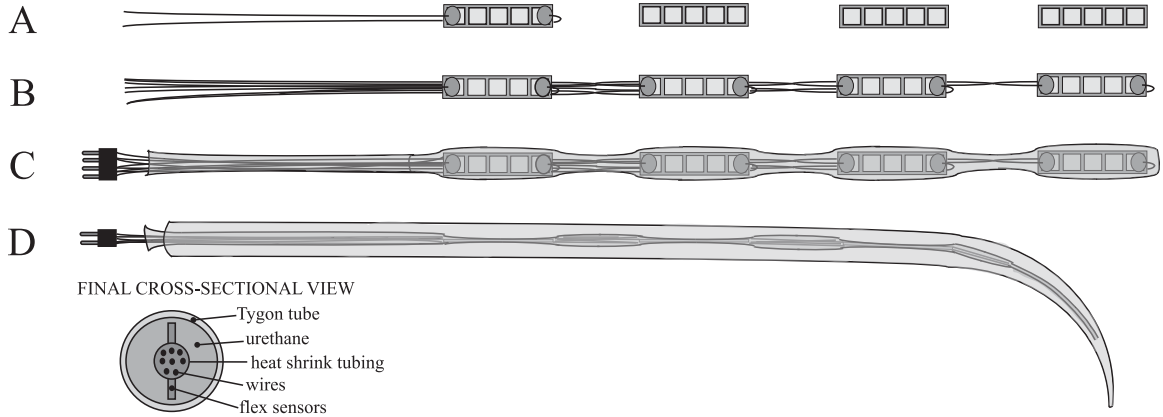


Figure 5.1: An overview of the cast urethane antenna construction process. Four flex sensors are enclosed in urethane casting with precurved tip. This bio-inspired antenna provides robot-to-wall distance information for the Garcia robot. This antenna is designed and built by Owen Loh [63,64].

and the mass of the robot. We used the values **A** and **B** that Lamperski et al. reported for the robot in [60].

5.2 Robotics Model: Implementation

5.2.1 Antenna Design

To provide tactile feedback to our mobile robot, we use an artificial antenna (Fig. 5.1) designed and built by Owen Loh [63,64]. The design is based on observations of cockroaches and their antennae while wall following [13,93,102,111].

The raw data provided by the antenna consists of an amplified voltage output, V_i , from each flex sensor. To extract the distance to the wall d from the voltage outputs, we performed a least-squares fit: while maintaining antenna-wall contact, we recorded voltages from each flex sensor as we varied the distance d and angle of the robot relative to the wall. We obtained a least-squares fit for the affine relationship $d = a^T V + b$. Here we do not consider the two proximal flex



Figure 5.2: The cast urethane antenna with embedded flex sensors mounted on the Garcia robot.

sensor measurements; the high stiffness near the base of the antenna and the addition of the support structure in the middle of the antenna have limited their motions and did not contribute significantly to the calculation of d . The omission of the most proximal sensory data is consistent with Camhi and Johnson's [13] result that wall following requires distal receptors in the flagellum without the sensory data from the base.

5.2.2 Integrating the Antenna with the Garcia Robot

For wall following, we combined the antenna-based PD controller suggested by the APU model (Section 4.1), together with a proportional-integral forward speed controller

$$\begin{bmatrix} u_1 \\ u_2 \end{bmatrix} = \begin{bmatrix} -K_V(v - v^*) - K_I \Sigma \\ -\hat{K}_P(d - d^*) - \hat{K}_D \dot{d} \end{bmatrix}, \quad \Sigma = \int_0^t (v - v^*) dt, \quad (5.2)$$

where v^* is the desired forward speed and d^* is the desired distance to the wall. To map the torques into motor voltages, the control law (5.2) is written $V = \mathbf{B}^{-1}u$, since \mathbf{B} is invertible.

Inserting (5.2) into (5.1), we have

$$\begin{bmatrix} \dot{y} \\ \dot{\theta} \\ \dot{\Sigma} \\ \dot{v} \\ \dot{\omega} \end{bmatrix} = \begin{bmatrix} v \sin \theta \\ \omega \\ v - v^* \\ -\gamma v - K_V(v - v^*) - K_I \Sigma \\ -\hat{B}\omega - \hat{K}_P(d - d^*) - \hat{K}_D \dot{d} \end{bmatrix}, \quad (5.3)$$

where d is the same as (4.3). Linearizing the system at its equilibrium point $(y, \theta, \Sigma, v, \omega) = (d^*, 0, -\hat{B}v^*/K_I, v^*, 0)^T$, we obtain the characteristic polynomial

$$p(s) = (s^2 + (\gamma + K_V)s + K_I) \cdot [s^3 + (\hat{B} + \hat{K}_D \ell)s^2 + (\hat{K}_P \ell + \hat{K}_D v^*)s + \hat{K}_P v^*]. \quad (5.4)$$

The second-order polynomial factor has negative roots if

$$K_V > -\gamma \text{ and } K_I > 0, \quad (5.5)$$

and, by Routh's stability criterion, the latter third-order polynomial factor has negative roots if

$$\hat{K}_P > 0, \quad \hat{K}_D > -\frac{\hat{B}}{\ell}, \quad \text{and} \quad \frac{\hat{K}_D}{\hat{K}_P} v^* > \frac{v^*}{\hat{B} + \hat{K}_D \ell} - \ell, \quad (5.6)$$

Table 5.1: Parameter values for *P. americana* (from Chapter 4) and the Garcia robot.

	v^* (m/s)	ℓ (m)	\hat{B} (s^{-1})	\hat{K}_P ($m^{-1}s^{-2}$)	\hat{K}_D ($m^{-1}s^{-1}$)
<i>P. americana</i>	0.352	0.027	12.7	2600	433
Garcia	0.5	0.139	3.53	39.16	23.49

where $\gamma, \hat{B}, v^*, \ell > 0$. Notice that the conditions for forward stability—which are constraints on K_V and K_I —are decoupled from the conditions on rotational stability—which are constraints on \hat{K}_P and \hat{K}_D .

5.2.3 Dynamically Scaled Parameters of *P. americana*

We found the necessary parameters for the Garcia robot using the principle of similitude; the APU's torsional dynamics equation (4.20) and the last row of (5.3) are identical, namely they are of the form

$$\dot{\omega} = -\hat{B}\omega - \hat{K}_P(d - d^*) - \hat{K}_D\dot{d}, \quad (5.7)$$

where \hat{B} , \hat{K}_P , and \hat{K}_D are known quantities for the cockroach (Chapter 4). Selecting two fundamental quantities, v and ℓ , leads to the following dimensionless ratios:

$$\tilde{B} = \frac{\hat{B}\ell}{v^*}, \quad \tilde{K}_P = \frac{\hat{K}_P\ell^3}{v^{*2}}, \quad \tilde{K}_D = \frac{\hat{K}_D\ell^2}{v^*}. \quad (5.8)$$

Setting the desired velocity for the Garcia robot to be 0.5 m/s and assuming \hat{B} to be constant, we calculated the dimensionally-scaled look-ahead distance for the Garcia robot. We found values for \hat{K}_P and \hat{K}_D in a similar way. The calculated values are shown in bold in Table 5.1 (second row).

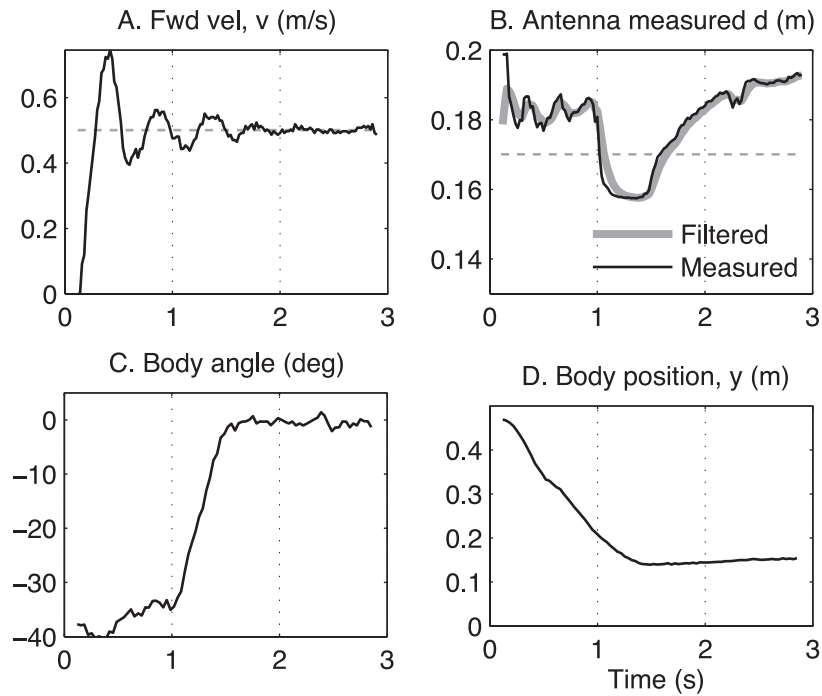


Figure 5.3: The Garcia robot’s internal states during a trial with parameters from Table 5.1. The onset of the angled wall contact occurs at $t = 1$ s. (A) Measured forward speed (solid) with $v^* = 0.5$ m/s (dashed). (B) Measured raw (solid black) and filtered (solid gray) d values with $d^* = 0.17$ m (dashed); to reduce noise, we low-pass filtered raw distance measurements: $d_k = \lambda d_{k-1} + (1 - \lambda)d_{\text{raw},k}$ where $\lambda = 0.7$ (trial and error); \hat{d} was estimated via finite difference. (C,D) Body angle and position obtained from overhead camera images.

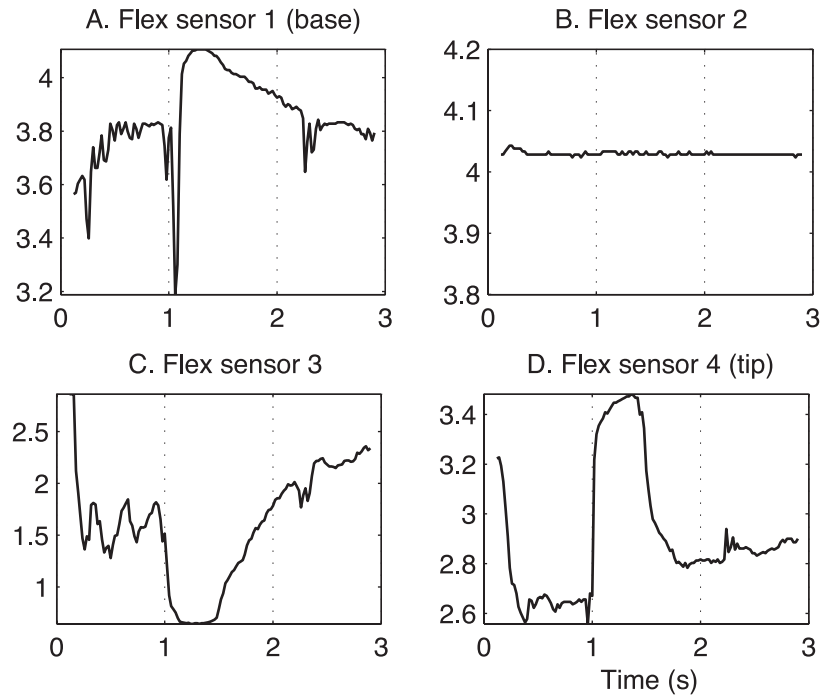


Figure 5.4: The raw amplified voltage values from the four flex sensors embedded in our antenna; they are shown for their qualitative form. The flex sensor at the base of the antenna (A), which is not used to calculate the value d_{raw} in Fig. 5.3B, shows the onset of the angled wall contact with a sharp peak. The second flex sensor from the base (B) registers zero motion because it is anchored to the rigid support base discussed in the main text. The two distal flex sensors (C,D) are used to calculate the measurement d_{raw} shown in Fig. 5.3B. The third flex sensor (C) flexes more (indicated by the decrease in voltage values) as it encounters the initial part of the angled wall. Meanwhile, the remaining distal part of the antenna (D) conforms to the wall by decreasing its flexion (indicated by the increase in voltage values).

5.3 Experiment: Robotic Wall Following

The experimental setup for the Garcia robot was similar to that of the cockroach behavioral experiment in Section 4.3. The robot followed a wall that consisted of a straight control wall to allow the robot to reach its steady state and an angled wall to act as a “step” perturbation to the internal state, θ . We used the parameter values for the Garcia robot shown in Table 5.1 with $K_V = 1 \text{ s}^{-1}$ and $K_I = 1 \text{ s}^{-2}$. This set of parameters satisfied stability conditions (5.5) and (5.6).

We ran 30 trials at $v^* = 50 \text{ cm/s}$ with the 30° angled wall; all 30 trials resulted in successful turning. Figures 5.3 and 5.4 show a subset of states that were collected during a typical trial; the rest of the trials were very similar. Our somewhat arbitrary choice of speed gains (K_V , K_I) produced substantial oscillations in the forward speed, but nevertheless reached steady state speed within about two seconds and did not imperil wall-following performance. The body-angle transient responses for the APU model and the Garcia robot were comparable (Fig. 7.1): the rise time, peak time, and overshoot for the Garcia was 0.60 s, 1.23 s, and 2.5%, respectively. For the APU from Chapter 4, dimensionally mapped into Garcia’s scale, these were 0.50 s, 1.20 s, and 17.3%.

The Garcia robot failed to negotiate turns of angles greater than about 40° because the distal end of the rigid antenna support catches the angled wall, forcing the robot to turn inward toward the wall. We believe this problem will be addressed through the design of more flexible antennae with more appropriately tapered mechanical stiffness.

Typically, the robot followed the wall with a constant error in d : in Fig. 5.3B the robot maintains the measured distance of 0.18–0.19 (solid) despite the commanded value (d^*) of 0.17 (dashed). This was likely caused by non-negligible forces produced by the artificial antenna against

CHAPTER 5. ROBOTIC INTEGRATION OF BIO-INSPIRED ANTENNA

the wall¹: adding a torsional spring term, $c(d - d_{\max})$, to the last line of (5.3) shifts the equilibrium distance from the wall to $(\hat{K}_P d^* + c d_{\max}) / (\hat{K}_P + c)$. For negligible stiffness c , the equilibrium distance is d^* as expected.

Figure 5.4 shows that flex sensors 3 and 4 (C, D) do not necessarily return to their original configuration after encountering the angled wall. One possible explanation could be that there is a range of “stable” configurations of the antenna for a given d due to friction, memory effects, or other factors. While the effects of these phenomena need to be addressed in future designs of the artificial antenna, the fact that the Garcia successfully navigated along the wall despite those factors suggests sufficiency of modeling assumptions in the APU model to represent the wall-following behavior of American cockroaches.

¹To quantify cockroach antenna reaction forces, we used the force levers that Dudek and Full [27] used to measure passive leg forces in cockroaches; the antennal forces fell below the noise floor of the sensors. This (and our qualitative observation) suggests that cockroach antennal forces are negligible compared to leg forces.

Chapter 6

The Antenna-Based Lateral Leg Spring

In the previous models, the control input is some abstract torque applied to the body through a continuous actuation. A fundamental question that remains is how such a control input might be applied to control stride-to-stride dynamics in a legged organism. To guide further development in maneuverable legged robots and generate hypotheses for how the biological system modifies its motor output, we require an more representative, anchored mathematical model than our APU model. To address this question, in this chapter, we employ a model called the lateral leg spring (LLS) which has shown to capture the within-stride dynamics of cockroach locomotion [95]. After providing a simple control strategy for this model (Section 6.1), we implement the same PD gains found in Chapter 4 and use antenna-like sensory feedback (Section 6.2) to show a stable wall-following behavior in a legged model.

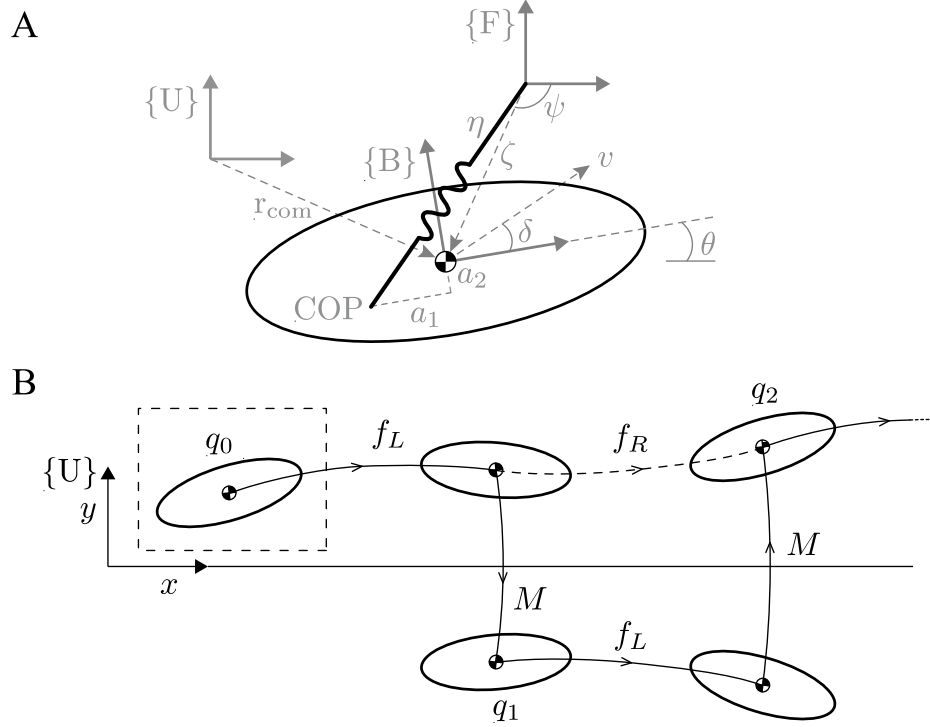


Figure 6.1: (A) A schematic model of the LLS model; θ is the body angle w.r.t. the x -axis in inertial frame $\{U\}$, v is the speed of the COM, δ is the velocity angle w.r.t. the x -axis of the body frame $\{B\}$, ζ is the distance from the foot placement to the COM, ψ is the angle from the x -axis of the foot frame $\{F\}$ to the COM, η is the leg length, $[a_1, a_2]^T$ is the location of the COP written in $\{B\}$. (B) Illustration of multi-step dynamics and its equivalent representations.

6.1 Model: LLS (2D Placement of COP)

In Section 3.1, we introduced the lateral leg spring (LLS) model developed by Schmitt and Holmes [96]. In their model, the center of pressure (COP) is placed along the fore-aft axis of the model. In this section, we relax that condition and allow the COP to be placed anywhere on the 2D plane of the LLS body.

Suppose the COP position for a left-step is parameterized by

$$\begin{bmatrix} a_1 \\ a_2 \end{bmatrix} = \begin{bmatrix} b_1 + c_1(\psi - \theta) \\ b_2 + c_2(\psi - \theta) \end{bmatrix}, \quad (6.1)$$

CHAPTER 6. THE ANTENNA-BASED LATERAL LEG SPRING

where a_1 and a_2 are along x and y-axis of the LLS body frame, $\{B\}$ and b_i 's and c_i 's are constants. A special case of this parameterization is when $a_2 = 0$ and $c_1 = 0$ (Section 3.1) [96,97]: if $a_1 < 0$, δ and ω are asymptotically stable; if $a_1 = 0$, ω becomes neutrally stable; if $a_1 > 0$, the system becomes unstable. When $a_1 < 0$, the body mechanics alone can stabilize the LLS system [96]. However a fixed COP on the fore-aft axis yields yaw dynamics that do not match biological data. Placing the COP laterally offset to the side ($a_2 = \text{const} < 0$) better matches the yaw dynamics, and that the system can achieve stability even if the COP lies in front of the COM as long as it is appropriately offset to the side (see Appendix B; [62]) as shown in Fig. 6.2.

Hamiltonian Dynamical Equation We restrict ourselves to $c_1 = c_2 = 0$ in (6.1), in which case the Hamiltonian for a left step can be written

$$H = \frac{p_\zeta^2}{2m} + \frac{p_\psi^2}{2m\zeta^2} + \frac{p_\theta^2}{2I} + \frac{k(\eta - l_0)^2}{2} \quad (6.2)$$

from which the equations of motion are

$$\begin{aligned} \dot{\zeta} &= \frac{p_\zeta}{m}, \quad \dot{p}_\zeta = \frac{p_\psi^2}{m\zeta^3} - \frac{k(\eta - l_0)}{\eta} (\zeta - a_2 \cos \phi + a_1 \sin \phi), \\ \dot{\psi} &= \frac{p_\psi}{m\zeta^2}, \quad \dot{p}_\psi = -\frac{k(\eta - l_0)}{\eta} (\zeta a_1 \cos \phi + \zeta a_2 \sin \phi), \\ \dot{\theta} &= \frac{p_\theta}{I}, \quad \dot{p}_\theta = -\dot{p}_\psi, \end{aligned} \quad (6.3)$$

where $\phi = \psi - \theta$ and p 's are the conjugate momenta. The leg length $\eta = \eta(\zeta, \psi, \theta, a_1, a_2)$ can be determined from Fig. 6.1A.

6.1.1 Hybrid Step-to-Step Dynamics

For task-level control of the multi-stride dynamics we seek a compact representation of the step-to-step dynamics. Let $\{A_k\}$ denote the location of the body frame at the beginning of the

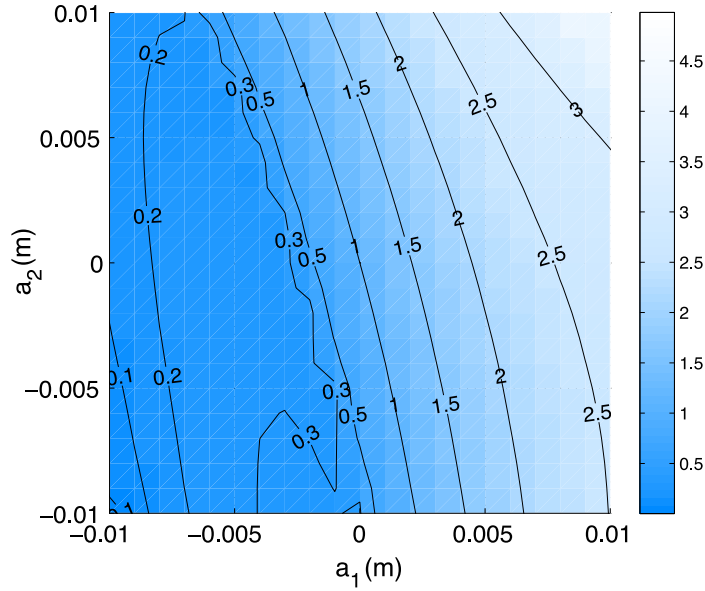


Figure 6.2: Maximum non-unity eigenvalue for the linearized return map at various fixed-COP positions around the COM. Parameters used for *P. americana* are shown in the caption of Fig. 6.3.

k^{th} step. In other words, g_k is the transformation from $\{A_k\}$ to the world frame $\{U\}$. For k odd, we take a mirror image around the x -axis of frame $\{A_k\}$ at the beginning of the k^{th} step (k odd), simulate the dynamics using the equations of motion for a left step, and then take another mirror image around the x -axis. In this way, the right step map is computed in terms of the left one. This can be expressed in terms of local coordinates $q = (v, \delta, \theta, \omega, x, y)^T$ as first “flipping” $(\delta, \theta, \omega, y)$, integrating the left step map, and then flipping back, namely

$$f_R(q) = M f_L(Mq), \quad (6.4)$$

where $M = \text{diag}\{1, -1, -1, -1, 1, -1\}$. Note that $MM = I$. We chose to flip about the x -axis for notational simplicity, but in principle any left-handed frame would work. This mapping leaves the right step map left-invariant under $\text{SE}(2)$.

For finding symmetric steady-state gaits, it will be convenient to define a special step-to-

CHAPTER 6. THE ANTENNA-BASED LATERAL LEG SPRING

step return map that amounts to an “integrate and flip” (see Fig. 6.1B). For a complete stride that includes a left step and then a right step, the stride-to-stride mapping is given by $f_{L-R} = f_R \circ f_L$, namely

$$f_{L-R} : q \mapsto Mf_L(Mf_L(q)) = (f \circ f)(q), \quad (6.5)$$

where $f(q) := Mf_L(q)$.

This approach eliminates the need to distinguish between left and right steps for control purposes. Note, however, that f is *not* left-invariant, even though both f_L and f_R are left-invariant. The resulting state evolution is given simply by

$$q_{k+1} = f(q_k), \quad (6.6)$$

keeping in mind that for odd steps, the value for q_k in this step-to-step formulation has already been “flipped.”

6.1.2 Reduced Return Map

To simplify controller analysis and design, we use translational symmetry and energy conservation, as first reported in [62]. Recall that the left- and right-step mappings, f_L and f_R are invariant to SE(2), but the step-to-step return map, $f = Mf_L$ is not. However, that mapping is invariant to pure x motions (had we chosen a different left-handed frame, translational invariance would have been in the direction of the axis of symmetry of the reflection to that frame). This was by design: our goal for control is wall following, and for simplicity, we have chosen to follow the x -axis. Thus x is removed by setting $x = 0$ at the beginning of each step. To remove v note that the Hamiltonian equation

$$H = \frac{1}{2}mv^2 + \frac{1}{2}I\omega^2 + \frac{1}{2}k(\eta - l_0)^2 = H_0 \quad (6.7)$$

is constant because the system energy is globally conserved. So, at each step

$$v = \left[\frac{2}{m} \left(H_0 - \frac{1}{2} I \omega^2 - \frac{1}{2} k (\eta - l_0)^2 \right) \right]^{1/2}. \quad (6.8)$$

Thus we have the following transformation

$$T_H : (\delta, \theta, \omega, y) \mapsto (v, \delta, \theta, \omega, 0, y) \quad (6.9)$$

that assigns $x = 0$ and computes v from (6.8). Note that T_H is invertible and T_H^{-1} is the transformation that simply removes the v and x coordinates. Then, we define the reduced variables and mapping

$$q^r = (\delta, \theta, \omega, y), \quad f^r(q_k^r, u_k) = T_H^{-1}(f(T_H(q_k^r), u_k)). \quad (6.10)$$

6.2 Model: Antenna-Based LLS (ALLS) Under PD Control

In the Appendix A, we find the LLS parameters for *P. americana* and show how we simulate the equations of motion for the LLS model; a simulation of LLS using those parameters is shown in Fig. 6.3. Based on the the same antenna model (4.3) used previously, we (numerically) “embed” the PD-controlled APU template in the LLS model providing a candidate mechanism for legged-locomotion heading control via antennal feedback.

As a preliminary control task, we chose to have the antenna-based LLS (ALLS) follow on top of a line or a virtual “wall” that is coincident with the x -axis. The result was an equilibrium point $\bar{q}^r = (\bar{\delta}, \bar{\theta}, \bar{\omega}, \bar{y})^T$ such that $\bar{q}^r = f^r(\bar{q}^r, 0)$. To address controllability, we numerically linearized the return map around a nominal equilibrium trajectory, to obtain

$$e_{k+1} = \mathbf{A}e_k + \mathbf{B}u_k, \quad z_k = \mathbf{C}e_k \quad (6.11)$$

CHAPTER 6. THE ANTENNA-BASED LATERAL LEG SPRING

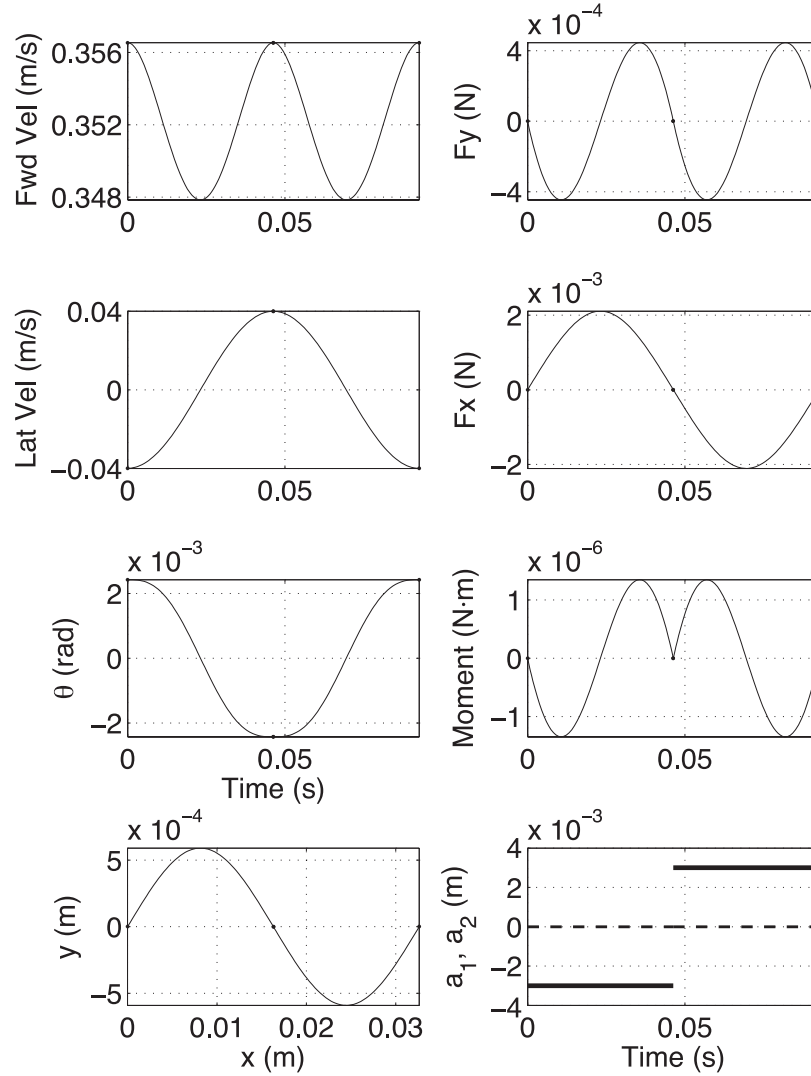


Figure 6.3: A full stride of LLS at its equilibrium point with the following parameters: $m = 0.77 \times 10^{-3}$ kg, $J = 1.0 \times 10^{-7}$ kgm², $l_0 = 0.0165$ m, $k = 0.766$ N/m, $\beta = 1.051$ rad, $a_1 = 0$ m, $a_2 = -0.003$ m, $v(0) = 0.359$ m/s. In the last subplot, dashed and solid lines are a_1 and a_2 , respectively.

CHAPTER 6. THE ANTENNA-BASED LATERAL LEG SPRING

where $\mathbf{A} = (\partial f^r / \partial q^r)(\bar{q}^r, 0)$, $\mathbf{B} = (\partial f^r / \partial u)(\bar{q}^r, 0)$, $\mathbf{C} = (\partial h / \partial q^r)(\bar{q}^r, 0)$, $e_k = q_k^r - \bar{q}^r$, $z_k = [d_k - \bar{d}, \dot{d}_k - \dot{\bar{d}}]^T$, $u_k := a_{1,k}$, and $h = [d, \dot{d}]^T$. We used a_1 rather than a_2 as our control input because in Fig. 6.2 the gradient of the eigenvalues is greater in the direction of x -axis than y -axis of $\{\mathbf{B}\}$. That is, a small displacement in a_1 gives us a greater control than that of a_2 ; this is consistent with Full and Koditschek's hypothesis, "maneuvers require minor neuromechanical alterations" [33]. In addition, updating the control input once per step (rather than continuously) resonates with the notion that inherent mechanical stability of puts less demands on neural feedback [33]. In (6.11), the condition number for the controllability and observability matrices are 7445 and 390, respectively, so the system is controllable and observable.

Here we make several approximations to the ALLS model to simplify control and connect the ALLS to a simpler model in our research program (Fig. 2.2). The third row of the linearized discrete dynamics (6.11) for parameters for *P. americana* can be written as

$$\omega_{k+1} - \omega_k = -(1.96)\omega_k - (1.08)(\delta_k - \bar{\delta}) + (611.86)u_k. \quad (6.12)$$

Since our simulations suggest that $\delta_k - \bar{\delta}$ remains at least an order of magnitude smaller than the other terms during transients, we neglect $\delta_k - \bar{\delta}$ and consider $\dot{\omega} \approx (\omega_{k+1} - \omega_k)f_s$, where $f_s = 10.8$ Hz (see Appendix A) is the stride frequency. Thus we approximate (6.12) with a continuous-time system,

$$\dot{\omega} \approx -\hat{B}\omega + u', \quad (6.13)$$

where $\hat{B} \approx 21.2$ and $u' \approx (6608)u_k$. This equation mirrors the unicycle model (4.20), and despite the fairly crude approximations, the coefficient $\hat{B} \approx 21.2$ in the LLS approximation (6.13) is within the confidence intervals of the fitted parameters for \hat{B} in cockroaches (Table 5.1). Also note that the u in (4.20) is a moment (scaled by inertia), whereas in the ALLS model, the control input is

the COP position. Hence the coefficient multiplying the control u_k in (6.13) is absorbed into u' for comparison purposes.

The similarity between the APU (4.20), and the approximate LLS (6.13), reveals a possible embedding of the PD-controlled APU into the ALLS. In fact, by setting $u'_k = -\hat{K}_P d_k - \hat{K}_D \dot{d}_k$ with the same control parameters fitted to the cockroach yields a closed-loop system of $e_{k+1} = (\mathbf{A} + \mathbf{BKC})e_k$ with all of its eigenvalues ($-0.64 \pm j0.16$ and $-0.13 \pm j0.49$) inside the unit circle, i.e., the closed-loop system is stable around the equilibrium trajectory.

6.3 Simulation: ALLS Wall Following

A simulation for this controller using the parameters for *P. americana* is shown in Fig. 7.1(E). In this control law, the COP lies nominally along the body y -axis, namely $a_1 = 0$ and $a_2 = -3$ mm (for the left step); the feedback controller varies the COP in the a_1 direction.

The most parsimonious controller sufficient to stabilize high-speed wall following in the APU model is a continuous PD controller mapping antenna measurements to a continuous moment about the COM. As shown, this control law applies with essentially no modification to the control of a legged running model, ALLS, by mapping sensor values to the COP position during each step. This result further supports the hypothesis that such a simple PD controller may underly task-level locomotion control of the American cockroaches.

Chapter 7

Discussion

This thesis takes a multifaceted view (Fig. 7.1) of a sensory-feedback-driven locomotor behavior observed in *P. americana* [13]: high-speed antenna-based wall following. In Chapter 4, we model this behavior (Fig. 7.1A) as a simple PD controller acting on the APU model (Fig. 7.1B). Next, we confirm that the PD controller (including the gains) fitted to cockroach behavior is sufficient in a real-world setting: our robot tuned with dimensionally scaled parameters and controller gains stably follows walls using our bio-inspired artificial antenna (Fig. 7.1(D)), and exhibits transient behavior comparable to both the simulated APU and the cockroach itself. To test the feasibility of the same PD controller in a legged system, we use a modified version of the LLS model [96,97]—namely, antenna-based LLS (ALLS)—in which the controller has authority over the position of the center of pressure (COP) at the start of each step as a function of antennal feedback. Importantly, we fit the parameters for the “open-loop” LLS model (leg stiffness, leg touchdown angle, etc.) during steady-state running, independent to how we fit the APU which involved fitting the closed-loop system including the controller gains to the angled-wall perturbation. Nevertheless, we find that the

CHAPTER 7. DISCUSSION

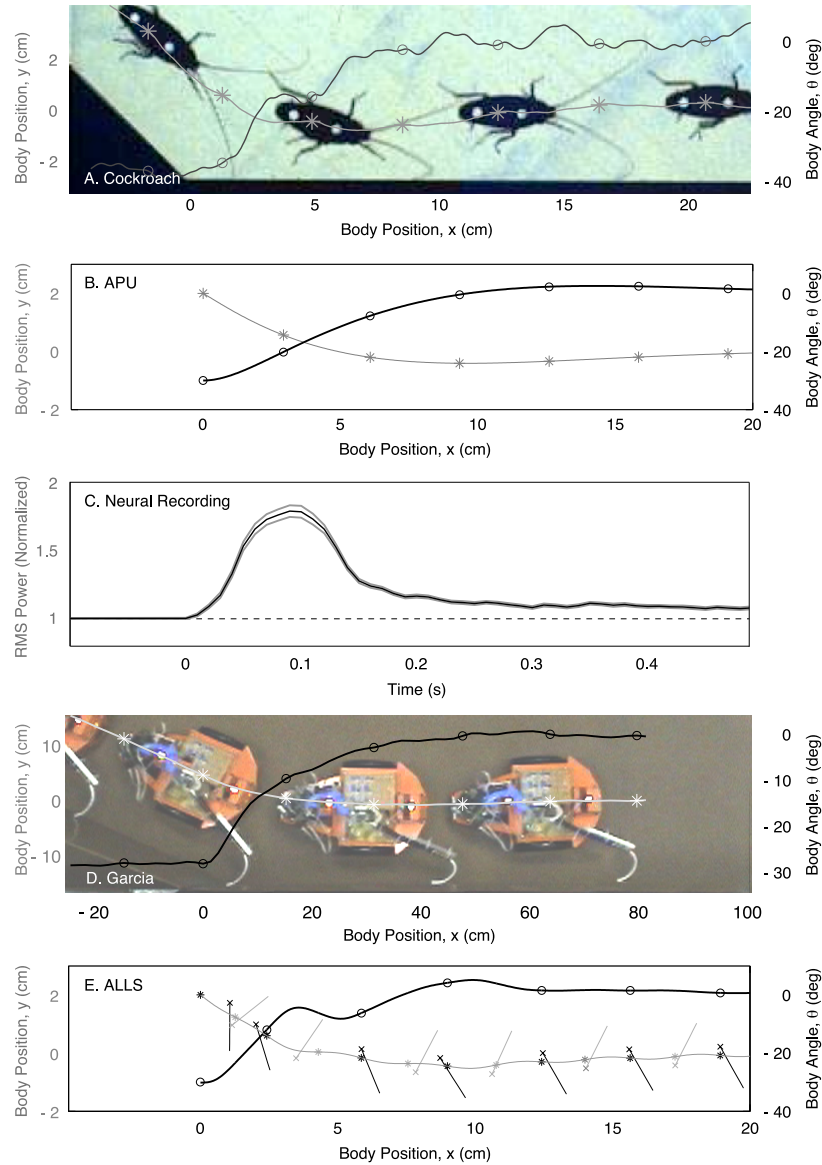


Figure 7.1: Subplots (A,B,D,E) show the task-space trajectories of several models and physical systems from our research program (Fig. 2.2); *’s and o’s indicate COM position and body angle, respectively, at the start of every stride (or dimensionally equivalent stride); (B,D,E) have dimensionally equivalent parameters and the same PD-control law as discussed in the text. (A) A typical trial of *P. americana* (the cockroach is shown every other stride); the cockroach is following the wall at ~ 45 cm/s. (B) APU model simulation using the parameters given in Table 5.1, first row. (C) Neural recording near the base of flagellum. (Image credit: [64]) (D) The Garcia robot experiment, where the robot is shown every other “stride”; the robot uses parameters given in Table 5.1, second row. (E) The ALLS model simulation, shown at the start of every step with *’s indicating COM, x’s indicating COP, and straight lines emanating from COP indicating the effective leg.

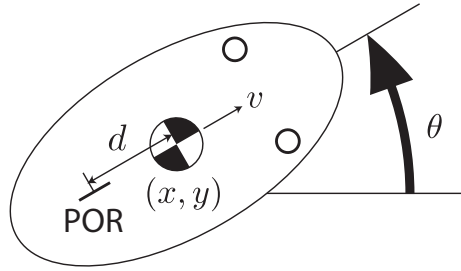


Figure 7.2: Chaplygin sleigh. The skate provides a nonholonomic constraint. d is positive as shown. The two small circles indicate frictionless sliders.

torsional dynamics of the LLS model can be numerically “reduced” to those of the APU model, with very close agreement in parameters. Using the same PD gains as the APU model, the ALLS model exhibits stability and a similar transient response (Fig. 7.1(E)) as the cockroach.

7.1 Multilevel Modeling

To elucidate the behavior of antenna-based wall following of the American cockroaches, we formulate our research program using templates and anchors [33] (Fig. 2.2), enabling us to address specific questions at each level in the hierarchy, as well as make quantitative connections between levels. For example, the simplest template, the APU model, neglects within-stride dynamics but nevertheless reveals a candidate task-level control law. We then anchor the controlled APU in the Garcia and ALLS models. At the same time, the successive elaboration of features in more complex models (e.g. forward speed control in the Garcia and within-stride dynamics of the LLS) allows us to address increasingly refined questions about the underlying biological system.

7.2 Chaplygin Sleigh and APU

The rotational damping term B discussed in Section 4.4.3 can be justified more directly if we consider a Chaplygin sleigh shown in Fig. 7.2. It is a planar unicycle (Section 4.1) but with the COM offset from the point of rotation. The equations of motion can be written as (Appendix C, [86])

$$\dot{v} = d\omega^2 \quad (7.1)$$

$$\dot{\omega} = -\frac{md}{J + md^2}v\omega \quad (7.2)$$

where m is the mass, J is the moment of inertia, v is the forward speed, ω is the angular velocity, and d is the distance of the POR (or skate) behind the COM. This has a family of equilibria of the form $(v, \omega) = (v_0, 0)$. The linearization is given by

$$\begin{bmatrix} \dot{\tilde{v}} \\ \dot{\tilde{\omega}} \end{bmatrix} = \begin{bmatrix} 0 & 0 \\ 0 & -\frac{md}{J+md^2}v_0 \end{bmatrix} \begin{bmatrix} \tilde{v} \\ \tilde{\omega} \end{bmatrix}$$

which has a zero eigenvalue and an eigenvalue with sign opposite to v_0 . The second equation

$$\dot{\tilde{\omega}} = -\underbrace{\frac{md}{J + md^2}v_0}_{\text{“} -\hat{B} \text{”}} \tilde{\omega} \quad (7.3)$$

resembles (4.20) without the input moment. This equation shows how the forward speed v_0 , mass m , and POR offset d play a role in the dynamics of angular velocity.

Using non-fitted parameter values $m = 0.77 \times 10^{-3}$ kg (from Section 4.4), $J = 1.0 \times 10^{-7}$ kgm² (from Appendix A.1), $d = 5 \times 10^{-3}$ m (assuming the COM is center of body), and $v_0 = 0.419$ m/s (from Table 4.1), we get $mdv_0/(J + md^2) \approx 13.5$ which is remarkably close to 16.1, the best-fit value of \hat{B} from behavioral experiments fitting the APU model (Table 4.1).

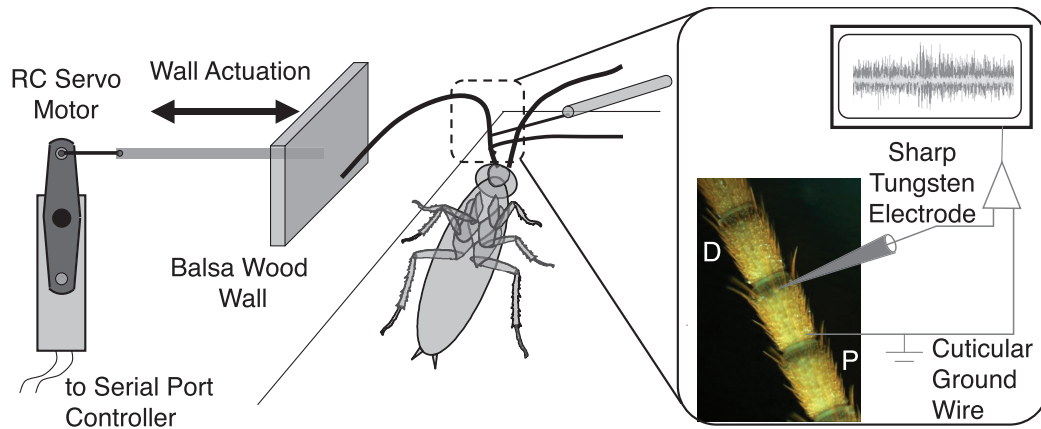


Figure 7.3: Electroantennogram setup to observe afferent signals from the flagellum under a simulated experiment that mimics a wall-following behavior. A live American cockroach is placed on its back (ventral side up) with its body and the base of its flagellum restrained. The RC servo drives the wall segment closer to the cockroach thus bending the antenna at a rate that resembles the sensory signal during first few strides of angled-wall following. A tungsten electrode is inserted near the base of the flagellum to provide extracellular recording from the antennal nerve; D: distal part of the antenna, P: proximal part of the antenna. (Image credit: [64])

7.3 Cockroach Antenna Neural Recordings

Sponberg et al. [108] examined *P. americana*'s primary antennal afferents for possible encoding of both position and velocity information with appropriate temporal filtering for the cockroaches' wall-following behavior. Their experimental setup (Fig. 7.3) created "open-loop" sensory perturbation similar to that given in Section 4.3 but without the cockroach actually moving. Their result (Figs. 7.4 and 7.1(C)) supported the hypothesis that antennal mechanoreceptors can serve as effective inputs to the proposed PD controller because the correlates of distance and rate of approach to a wall appear directly in the antennal nerve and the time course of the neural response closely matches the kinematics of turning. That is, their result provided further evidence that PD-like control may exist in cockroach wall following, although some care must be taken when comparing closed- and open-loop experiments [47, 84].

CHAPTER 7. DISCUSSION

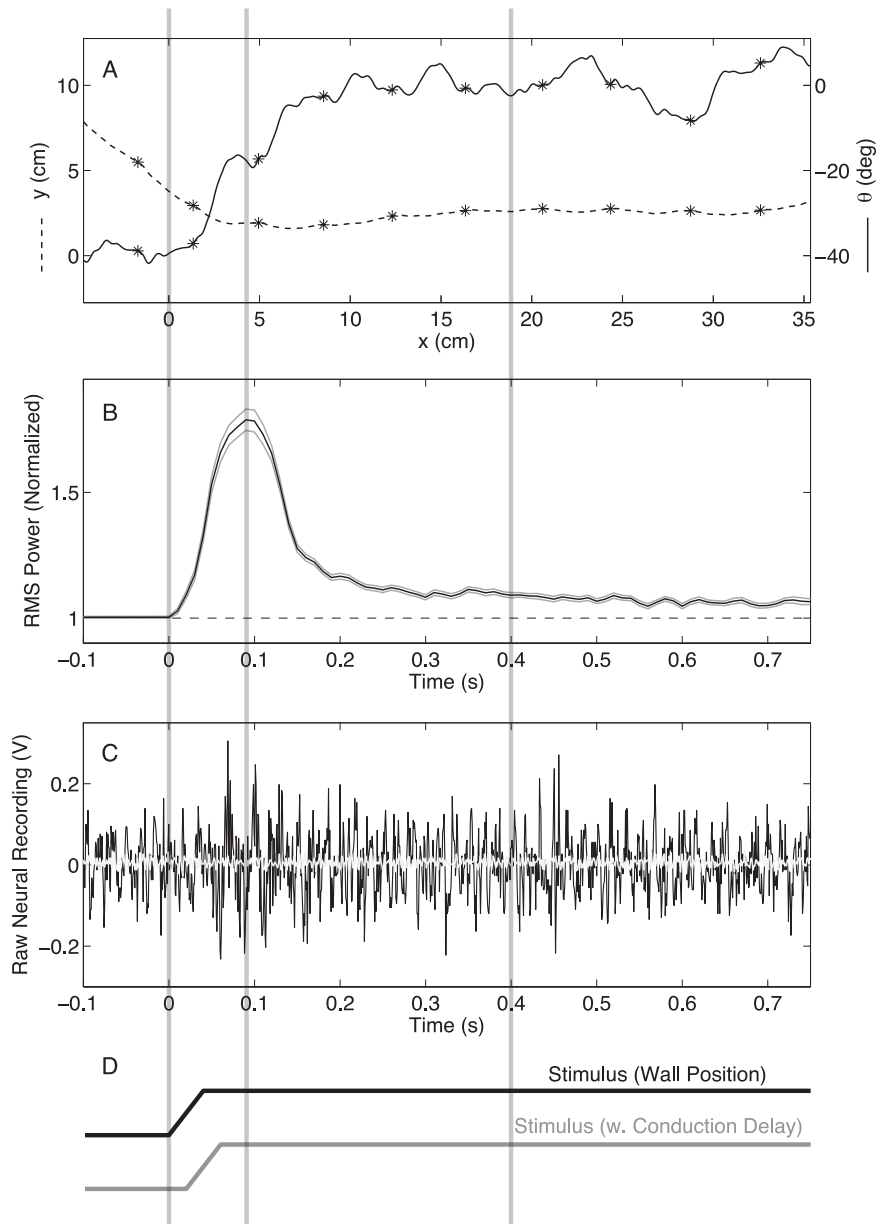


Figure 7.4: Comparison of the antenna neural recording to the kinematic data of a running cockroach. (A) The position (dashed) and orientation (solid) of a cockroach running along a wall (Fig. 4.7); strides are marked by asterisks (*). (B) Normalized neural RMS power (mean (black) with confidence interval (gray)) of the antenna when the wall approached toward the cockroach and stopped; it has been scaled to approximately match the kinematic traces above. (C) Raw neural recording voltage (black) and background voltage (gray). (D) Time trace of the actual wall displacement (black) and delay-accounted wall displacement (gray). The vertical lines indicate (from left to right) the stimulation onset, RMS peak time, and settling time. (Image and caption credit: [64])

7.4 Biologically-Inspired Tactile Sensors

Toward our goal of a robotic model of wall following, our antenna design captures several key features cockroach antennae. However, due to the constraints of our prototyping process, the antenna stiffness was not well matched to its biological counterpart: unlike that of the cockroach, this stiffness produced a non-negligible force between the robot and the wall causing an offset in the robot's distance to the wall. To remedy this issue we need to better characterize the cockroach antenna mechanics, similar to a prior study of crayfish antennae [113]. Then, we need to design our antenna to match important parameters such as the stiffness profile. We believe that Shape Deposition Manufacturing, also used for manufacturing the robot legs [3, 17], offers a viable solution.

In addition to enhancing our inquiry into a biological system, bio-inspired antennae offer potential benefits to robotics. Ours consists of a ten dollar $50\text{K}\Omega$ flex sensor cut into four pieces enclosed in urethane, rendering it inexpensive, low power, and mechanically robust. In addition, our antenna is insensitive to low or extremely bright ambient light (unlike vision and IR), does not emit energy (unlike sonar and IR), and does not require a specific wall type (unlike sonar, IR, and vision, which may fail for common urban surfaces such as fences, highly specular walls, or glass).

Other researchers have built tactile sensors inspired by arthropod antennae. Our work builds directly on [23] who use a single unmodified flex sensor to control a hexapod on a treadmill. Our design is similar to Barnes et al. [6] who embed three bend sensors in a passive, large-deflection antenna inspired by lobsters that distinguishes between contact with solid objects versus water currents [5]. Whereas our design focuses on control in the horizontal plane, Lewinger et al. [65] use two cockroach-inspired stiff antennae to traverse sagittal-plane obstacles. Our antenna uses no basal information, but whisker-inspired devices [56, 57, 68, 88, 99, 116], by contrast, use *only* basal infor-

mation, since whiskers themselves are insensitive hairs [46].

7.5 Robotics for Biology

Physical models can provide an important link between biological experimentation and mathematical modeling. In biology, complexity can obscure generalizing principles, and varying parameters to test a system's responses is often difficult and time consuming. In addition, it is difficult to capture an animal's internal states (e.g., neural recordings) while minimizing interference with the animal's natural behavior. Mathematical models can reveal idealized responses, but inevitably neglect the complexity of interaction with the surrounding environment. Experimental robotics allows the embodiment of control hypotheses in the context of difficult-to-model real-world phenomena where, in comparison to biology, it is much easier to vary system parameters and monitor system state variables. These can help in generating, refuting, and supporting biological hypotheses [50].

In this thesis, we use our robot to support the hypothesis of the efficacy of the PD controller—which is stable in our mathematical model—in a real-world setting. Two further observations can be made. (1) Our result supports Camhi and Johnson's [13] claim that cockroach wall following is mediated by the flagellum (not the base) of the antenna: our robot successfully follows a wall using feedback from the two distal flagellar antenna segments. (2) Figure 5.4 reveals that the base flex sensor can potentially provide a sensory cue faster than that from the rest of flex sensors, particularly if we account for the typical conduction velocity (1 – 4 m/s) for non-giant invertebrate neurons. This observation is consistent with the experiment by Comer et al. [20] where they show the important role that the mechanoreceptors at the base of the antenna play in triggering an escape response.

CHAPTER 7. DISCUSSION

Other researchers have considered robotics to address biological behaviors [118]. For example, Chapman and Webb [18] implement a neural circuit on a mobile robot where IR sensors act as the robot’s “antennae”; their robot exhibits an escape response followed by a wall-following response, much like that of a cockroach.

7.6 ALLS for Biology and Robotics

In this thesis, we show that the ALLS model exhibits stable wall following using exactly the same PD gains as the APU (Chapter 4). We propose two hypotheses from our result. (1) The afferents or the CNS suppresses (via a low-pass or notch filter) the sensory input frequency near their stride frequency; this hypothesis is motivated by the fact that the sensory signals seem to show a low-pass filtered response consistent with the time course of the stride-to-stride kinematics [64]. Alternative hypotheses are that (A) an efferent copy might be used to cancel out the frequencies observed by the antenna [111], or (B) the mechanics of the the antenna alone can filter the oscillation. To test the effect of the lateral oscillations on the antenna filtering, legged robots such as RHex [91] or even wheeled robots such as Garcia could be used; the Garcia robot would have to emulate, up to some limit, the within-stride dynamics of the ALLS. (2) Increasingly anchored models which represent cockroach kinematics with increasing biofidelity can be used to tease apart the contributions of individual legs during turning [54]. We hypothesize that the motion of the COP from step to step is governed by our PD controller. To test this, an experimental paradigm may consist of cockroaches following along a wall with perturbations [13, 22] while individual leg forces and kinematics are measured to recover COP motions [115]. Together, these data could be used to approximate the mapping from antennal measurements to COP motions.

CHAPTER 7. DISCUSSION

In this thesis, we numerically reduce the ALLS model to represent the APU's PD controller for the ALLS. A more formal reduction is warranted. For example, Poulakakis and Grizzle [81] provide a formal approach to apply a controller defined for a Spring-Loaded Inverted Pendulum (SLIP) model of sagittal-plane running to a more anchored model. Similarly, it may be interesting to address how the PD controller for the APU model would be applied to its higher anchors such as ALLS, ALLS with three legs [104], or 3D SLIP/ALLS model [90, 92, 103]. This may help in generating hypotheses such as the placement of the COP in 3D which can generate not only motions in yaw but also motions in pitch and roll.

Shifting COP location based on sensory stimuli may provide an alternative bio-inspired control strategy for hexapedal robots [91]. The shifting of the COP can be achieved by touching down three legs that collectively generate a force vector pointed at the desired COP position, similar to that of cockroaches [54, 115]. The sagittal-plane motions that result from 3D models or legged robots may lead to important design requirements for artificial sensors; for example, the antenna may be need to be stiffer along the sagittal plane than along the lateral plane [67, 89, 111].

7.7 Within-Modality Sensory Integration

Animals rely on a myriad of sensors—proprioceptors, vestibular, exteroception, etc.—when moving. Proper integration of sensory information is crucial to minimize the loss of important data. Understanding how animals integrate these sensory modalities is a challenging task because different sensory modalities may have weights that vary independently depending on environmental conditions. Rather, we ask a simpler question: how do cockroaches integrate sensory inputs from both of their antennae during high-speed wall following (Fig. 7.5). How cockroaches process

CHAPTER 7. DISCUSSION

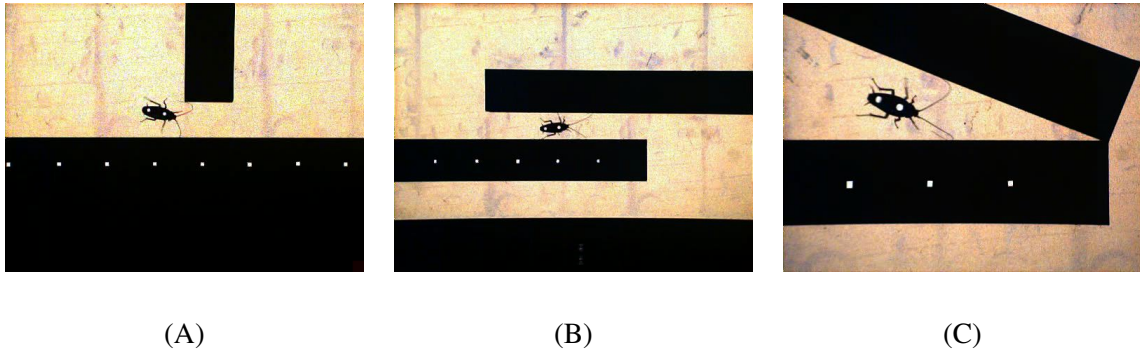


Figure 7.5: Preliminary experiments to address how a cockroach might integrate sensory information from both of its antennae. A cockroach that is following a wall using its right antenna is faced with (A) impulse-like signal, (B) step-like signal, or (C) ramp-like signal from its left antenna. How would the new information from its left antenna contribute to its right antenna wall-following control strategy? Also in (B), will it continue to follow the right wall or will it start to follow the left wall using its left antenna?

within-modality signals may provide new ideas in corridor-following mobile robots as well as in bee vision [110] and cockroach antennal decision making [18,44].

Chapter 8

Conclusion

In Part I of this thesis, we show that the synergy between robotics and biology enables mutual discoveries for both fields. We take a multidisciplinary approach that incorporates mathematical modeling, robotic experiments, and ethology to provide a glimpse into the neuromechanical control of one of the fastest terrestrial insects, the American cockroach [73]. Our biological modeling reveals a new idea for the control of legged robots under sensory feedback: stride-to-stride center-of-pressure placement may provide a simple mechanism for task-level control based on sensory feedback. Implementation of legged robot control based on this idea may in turn help biology by providing a new vehicle to test specific inter-leg coordination strategies for modulating the COP.

Appendix A

ALLS Simulation

A.1 Simulation Methods

We simulate the LLS model using Matlab (The MathWorks Inc., Natick, MA, USA) using the convention in Section 6.1.1: for every right-leg step, convert it to a left-leg step, simulate the within step dynamics, and then convert it back to a right-leg step. This enables us to specify the COP position using (6.1) and integrate the equations of motion derived from (6.3) without the explicit representations of a left or right step in the equations. We use Matlab's `ode45` with time varying step size to integrate the equations of motion. The integration for a step terminates as soon as the compressed leg returned back to its relaxed length l_0 .

We find the equilibrium point $\bar{q} = (v, \delta, \theta, \omega, y)^T$ using the Levenberg–Marquardt method in Matlab's `fsolve` function. While fixing the state v to a desired value, the function minimizes the error difference of a step, $f(q) - q$. We find the step-to-step return map Jacobian, A , about the equilibrium point using a central difference approximation. The i^{th} columns are given by $[A]_i = (f^r(q + e_i\epsilon) - f^r(q - e_i\epsilon))/2\epsilon$, where $\epsilon = 1 \times 10^{-6}$ and e_i is the i -th column of 4×4 identity

APPENDIX A. ALLS SIMULATION

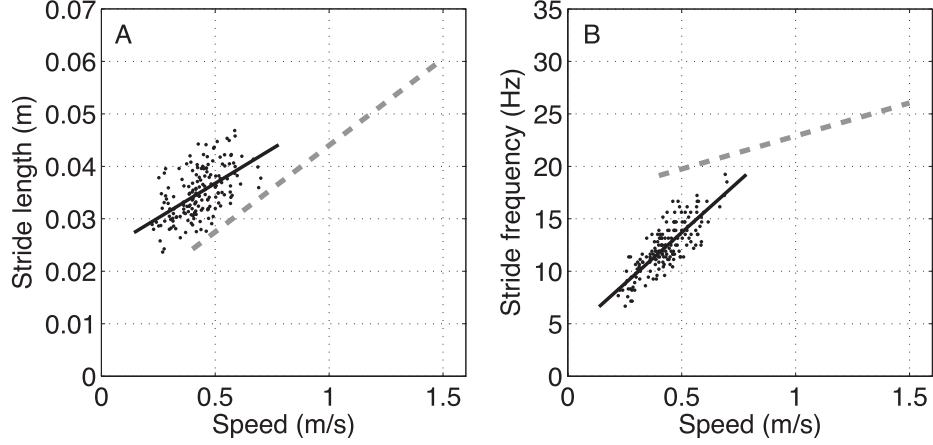


Figure A.1: (A) Stride length versus speed and (B) stride frequency versus speed of the first 4 strides (prior to angled-wall contact) of 43 trials from the data from Chapter 4. The solid line is the linear fit of the data. The dashed line is the linear fit of the data collected by Full and Tu [37]. Unlike Full and Tu, we use cockroaches that are blinded and elicited an escape response and following a wall (Section 4.3). We assume that the data is adequate for our preliminary fitting of the LLS model, and we reduce the bias incurred from wall following by matching the waveform characteristics (e.g. stride length and stride frequency) rather than the waveform itself.

matrix. Similarly, we find the stride-to-stride return map Jacobian to determine the stride-to-stride eigenvalues for Fig. 6.2.

We use the following parameters and measurements of *P. americana*: $m = 0.77 \times 10^{-3}$ kg, $J = 1.0 \times 10^{-7}$ kgm², \bar{v} (avg velocity) = 0.352 m/s, L_s (stride length) = 0.033 m, f_s (stride frequency) = 10.8 Hz, $v_{\text{lateral,max}} = 0.04$ m/s, and $\theta_{\text{max}} = 0.03$ rad. We use the rectangular prism approximation [115] to find the moment of inertia in the yaw direction. The stride length and the stride frequency has been found from Fig. A.1.

A.2 Parameters for *P. americana*

The values for leg rest length l_0 , leg spring constant k , initial leg touch down angle β_0 , and fixed COP position a_2 are chosen to satisfy constraints on the stride length, stride frequency,

APPENDIX A. ALLS SIMULATION

and maximum lateral velocity. Because the system is underdetermined, we make sure that these parameters are within an order of magnitude from the dimensionally scaled values of *Blaberus discoidalis* used in [95]. A simulation of LLS model using these set of values are shown in Fig. 6.3. The magnitude of the body oscillation is about an order of magnitude smaller than that of the actual cockroach because of LLS's simplification of the tripod legs into a single virtual leg; a single leg cannot generate enough torque to match that of the original three legs while having the parameter values that are physically realizable [62, 95].

Appendix B

Analysis of COP Placements

Just for this appendix, we use the convention defined in Lee et al. [62] to match that of Fig. B.1.¹ Using that convention, we get, for the left-leg stance, the Hamiltonian of the LLS system implemented with a linear spring

$$H = \frac{p_\zeta^2}{2m} + \frac{p_\psi^2}{2m\zeta^2} + \frac{p_\theta^2}{2I} + \frac{k(\eta - l_0)^2}{2} \quad (\text{B.2})$$

where ζ , ψ , k , l_0 , I , and m denote the distance from the foot placement to the COM, the angle from the foot placement to the COM, the linear spring stiffness, the relaxed leg length, the moment of inertia, and the mass, respectively. The length of the leg is given in terms of the COP location by

$$\eta = \left[b_1^2 + b_2^2 + \zeta^2 + \phi(2b_1c_1 + 2b_2c_2 + (c_1^2 + c_2^2)\phi) + 2\zeta((b_1 + c_1\phi)\cos\phi + (b_2 + c_2\phi)\sin\phi) \right]^{1/2}. \quad (\text{B.3})$$

¹You can covert from the convention defined in Section 6.1 as the following: $a_1 \rightarrow d_2$, $b_1 \rightarrow b_2$, $a_2 \rightarrow -d_1$, $b_2 \rightarrow -b_1$. Further,

$$\begin{bmatrix} d_1 \\ d_2 \end{bmatrix} \triangleq \begin{bmatrix} b_1 + c_1(\psi - \theta) \\ b_2 + c_2(\psi - \theta) \end{bmatrix}. \quad (\text{B.1})$$

APPENDIX B. ANALYSIS OF COP PLACEMENTS

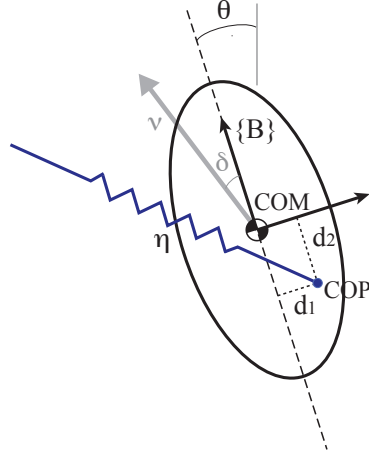


Figure B.1: A schematic model of the LLS model, showing the coordinates used by Lee et al. [62].

Hamilton's equations of motion with our new COP and the linear leg spring model are given by

$$\begin{aligned}
 \dot{\zeta} &= \frac{p_{\zeta}}{m}, & \dot{p}_{\zeta} &= \frac{p_{\psi}^2}{m\zeta^3} - \frac{k(\eta - l_0)}{\eta} (\zeta + (b_1 + c_1\phi) \cos \phi + (b_2 + c_2\phi) \sin \phi), \\
 \dot{\psi} &= \frac{p_{\psi}}{m\zeta^2}, & \dot{p}_{\psi} &= -\frac{k(\eta - l_0)}{\eta} (b_1c_1 + b_2c_2 + (c_1^2 + c_2^2)\phi \\
 & & & + \zeta(b_2 + c_1 + c_2\phi) \cos \phi - \zeta(b_1 - c_2 + c_1\phi) \sin \phi), \\
 \dot{\theta} &= \frac{p_{\theta}}{I}, & \dot{p}_{\theta} &= -\dot{p}_{\psi},
 \end{aligned} \tag{B.4}$$

where $\phi \triangleq \psi - \theta$.

B.1 Effects of Various COP Placements

In order to match the LLS system with an actual cockroach data (Fig. B.2), we need to understand the effects of b_i and c_i (or $d_i(kT)$) on the overall system. To do so, our initial attempt is to consider various protocols for the COP placements:

- (a) Increment d_1 while $d_2 = 0$;

APPENDIX B. ANALYSIS OF COP PLACEMENTS

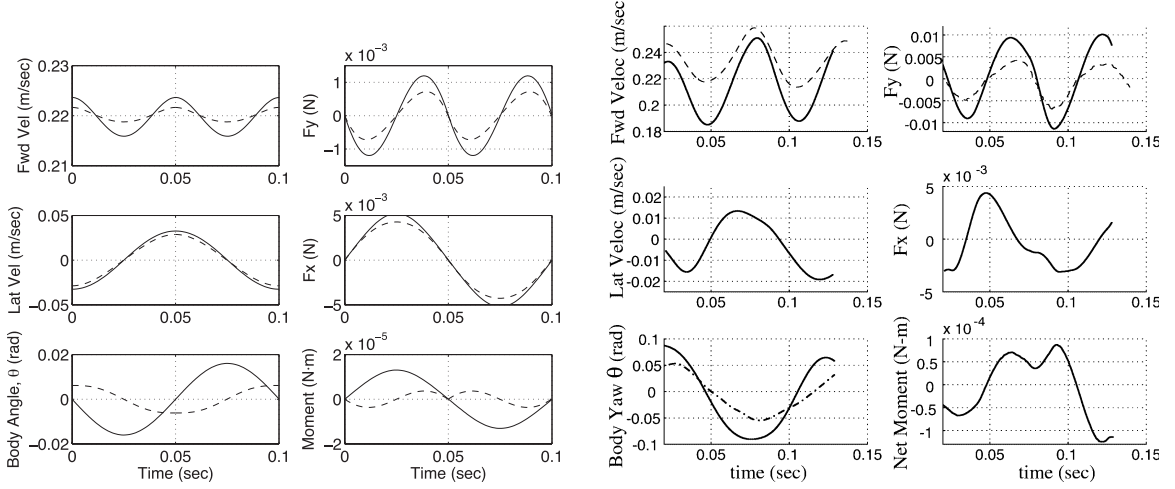


Figure B.2: *Left*: A stride of the original LLS model ($d_1 \equiv 0$) with a fixed COP (solid) and a moving COP (dashed). The used parameters for the fixed COP are: $v = 0.226$ cm/s, $k = 2.4$ N/m, $\beta_0 = 1$ rad, $l_0 = 0.0102$ m, $d_2 = -0.0025$ m; for the moving COP are: $v = 0.2235$ m/s, $k = 3.52$ N/m, $\beta_0 = 1.125$ rad, $l_0 = 0.0082$ m, $d_2 = 0.0025$ m \rightarrow -0.0025 m. *Right*: Experimental measurements of *Blaberus discoidalis* from several sources, [36, 37, 59]; figure from [95]. (Notice, since the right figure doesn't start from $t = 0$, the stride period is roughly the same between the two figures.)

- (b) Increment d_2 while $d_1 = 0$;
- (c) Increment the amplitude of a moving d_2 while $d_1 = 0$;
- (d) Increment the offset of a moving d_2 while $d_1 = 0$;
- (e) Increment d_1 while d_2 is moving;

Figure B.3 illustrates these protocols schematically for a left step; for a right step, the COP path is mirrored about the body y -axis. For each protocol and their parameter increments, we found the corresponding equilibrium points and simulated a full stride (starting with a left step) from the equilibrium points. The results from the simulations are shown in Figs. B.4, B.5, and B.6. For each incrementing parameter, we plotted the result using different shades of gray. The first two columns of a subfigure shows the COM velocity and leg-spring forces in lateral and forward directions (i.e.

APPENDIX B. ANALYSIS OF COP PLACEMENTS

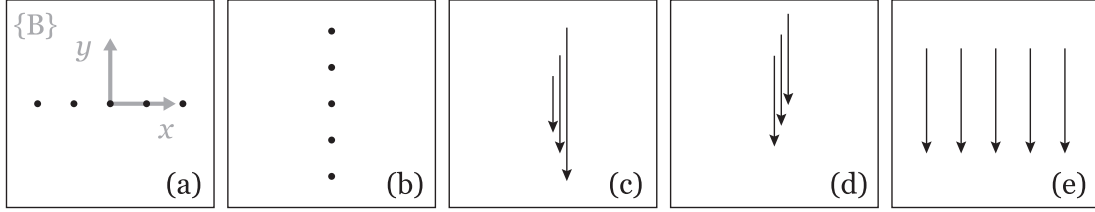


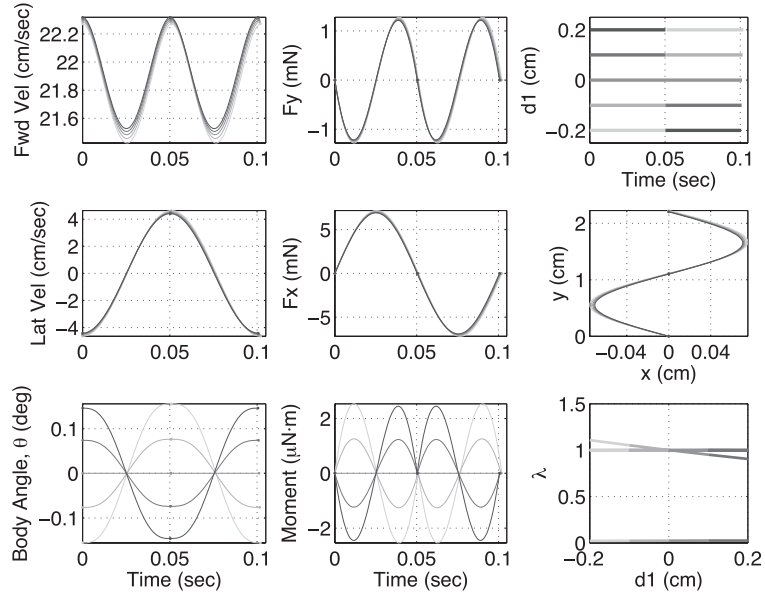
Figure B.3: COP placement protocols for a left step with respect to the body frame $\{B\}$. The solid dots indicate fixed COP positions; the arrows indicate the direction, magnitude, and offset of moving COPs.

x and y directions in the inertial frame $\{U\}$), the body angle, and the moment. The last column shows d_1 (solid line) and/or d_2 (dashed line) as a function of time, COM path, and the eigenvalues as a function of the incrementing parameter. The rest of the parameters (i.e. k , v , β_0 , and l_0) were chosen to closely match the stride length and frequency of cockroach data [95].

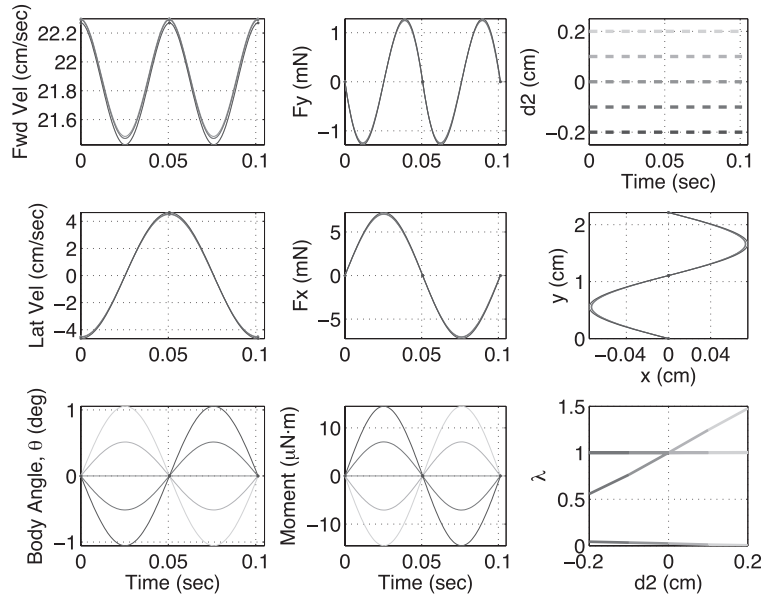
Protocol (a): Fixed COP on lateral axis. Figure B.4(a) shows results of a simulated LLS model in which we fixed the COP at various positions along the x -axis of the body frame $\{B\}$. As desired, when $d_1 > 0$, the profiles of the body angle, θ , and the moment waveforms resemble actual cockroach data (Fig. B.2), as well as that of the moving COP proposed by Schmitt and Holmes [97] (reproduced in Fig. B.2, *Left*). Note that the positive cosinusoidal waveforms of the body angle (which agrees with the biological data) for a fixed COP only occur when d is on the positive x -axis of $\{B\}$. Fig. B.4(a) indicates that the increase in $|d_1|$ amplifies the body angle and the moment waveforms while the other measurements, including the stride length and frequency, remain relatively constant. This isolated effect of d_1 will be useful later on when we fit the data to another waveform. In addition, the eigenvalue plot shows that the system becomes unstable when $d_1 < 0$ and stable when $d_1 > 0$.

Protocol (b): Fixed COP on fore-aft axis. As a comparison to the previous result, Fig. B.4(b) shows the effects of different locations d_2 for a fixed COP. Although the body angle

APPENDIX B. ANALYSIS OF COP PLACEMENTS



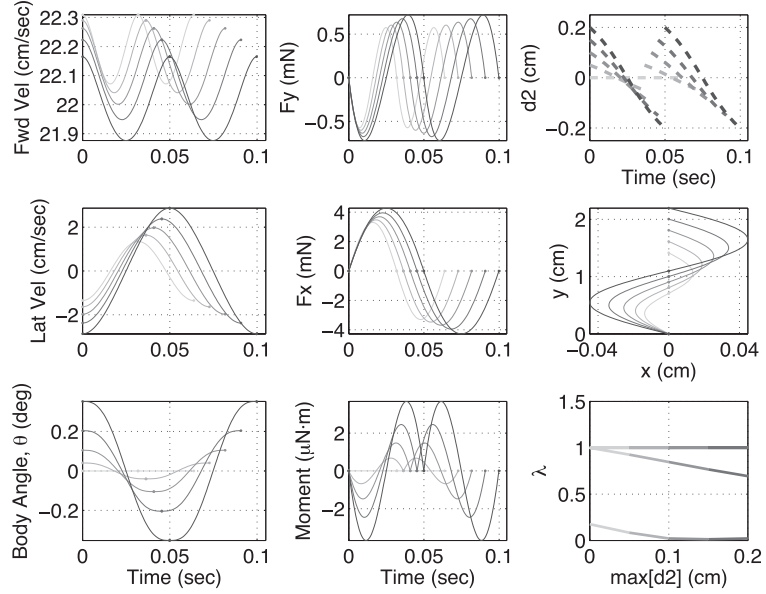
(a) Increment $d_1 = \{-0.2, \dots, 0.2 \text{ cm}\}$ while $d_2 = 0$.



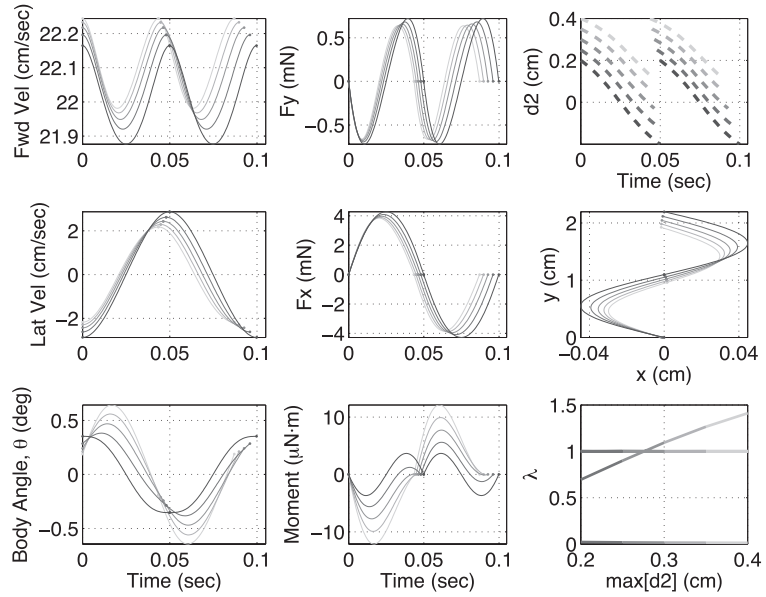
(b) Increment $d_2 = \{-0.2, \dots, 0.2 \text{ cm}\}$ while $d_1 = 0$.

Figure B.4: See text for description of each COP protocol. The parameters used in this figure are: $m = 0.0025 \text{ kg}$, $I = 2.04 \times 10^{-7} \text{ kg m}^2$, $k = 3.52 \text{ N m}^{-1}$, $v = 0.2275 \text{ m/s}$, $l_0 = 0.0127 \text{ m}$, $\beta_0 = 1.12 \text{ rad}$ (or 64.2°). Note, unlike Fig. B.2, these figures have scaled units (e.g. cm and mN) for clarity.

APPENDIX B. ANALYSIS OF COP PLACEMENTS



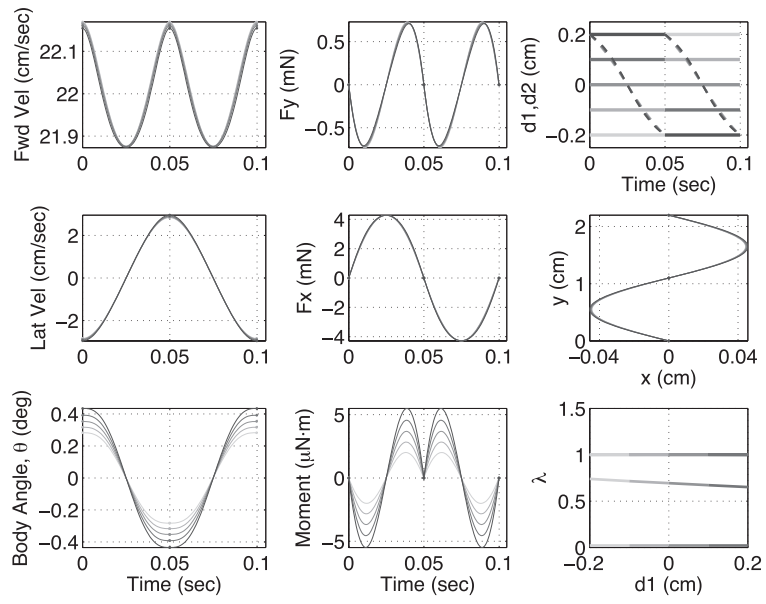
(c) Increment the amplitude of moving d_2 from 0 to 0.2 cm while $d_1 = 0$.



(d) Increment the offset of moving d_2 from 0 to 0.2 cm while $d_1 = 0$.

Figure B.5: The parameters used here are: $m = 0.0025$ kg, $I = 2.04 \times 10^{-7}$ kg m², $k = 3.52$ N m⁻¹, $v = 0.2235$ m/s, $l_0 = 0.0082$ m, $\beta_0 = 1.125$ rad.

APPENDIX B. ANALYSIS OF COP PLACEMENTS



(e) Increment $d_1 = \{-0.2, \dots, 0.2 \text{ cm}\}$ (solid) while d_2 (dashed) is moving from 0.2 to -0.2 cm .

Figure B.6: Parameters used are: $m = 0.0025 \text{ kg}$, $I = 2.04 \times 10^{-7} \text{ kg m}^2$, $k = 3.52 \text{ N/m}$, $v = 0.2235 \text{ m/s}$, $l_0 = 0.0082 \text{ m}$, $\beta_0 = 1.125 \text{ rad}$.

APPENDIX B. ANALYSIS OF COP PLACEMENTS

is sinusoidal (not cosinusoidal, like the cockroach), the location of d_2 does have a larger impact on the magnitude of body angle and the stability of the system (steeper slope for the moving eigenvalue) than d_1 in the previous protocol. We speculate that one cause of this differences in impact level is due to the large value of β_0 ; since $\beta_0 = 1.12 > \pi/4$, the leg force is oriented primarily in the lateral direction rather than the fore-aft direction. Thus, changes in d_2 cause greater moment arm changes than the equal changes in d_1 . We will utilize this effect in Sect. 6.2 by using d_2 as our control input. We also note that the body velocity (and position) and foot forces of this figure matches the previous figure. Although not shown, as the fixed COP position traverses in this neighborhood, without the restriction of $d_1 = 0$ or $d_2 = 0$, the body velocity and foot force waveforms remain relatively constant. On the other hand, the waveforms for the body angle and the moment go through phase and amplitude changes.

Protocol (c): Incrementing magnitude of a moving COP on the fore-aft axis. For fore-aft COP motion along the body frame y -axis, Fig. B.5(c) shows the effects of changing the magnitude of COP motion. Unlike the previous protocols, varying the magnitude of a moving COP causes large changes to all the kinematics, step length, and step frequency. Although it is not shown here, further increase in magnitude (also observed in [95]) or reversing the direction (i.e. aft to fore) of the moving COP drives the system unstable.

Protocol (d): Forward Shifting of a Moving COP. Figure B.5(d) shows the effects of shifting a moving COP in y direction in $\{B\}$. It shows that, as the offset b_2 increases (or decreases, although not shown), the body loses its cosinusoidal waveform and eventually becomes unstable. We emphasize that the system does not go unstable as soon as the offset $b_2 > 0$ nor $b_2 < 0$. Also the instability does not necessarily occur even though the moving COP remains in front of the COM

APPENDIX B. ANALYSIS OF COP PLACEMENTS

most of the time. Along with Protocol (c), we introduce one possible explanation of these results in Sect. B.3.

Protocol (e): Lateral Shifting of a Moving COP. Lastly, we look at the result of incrementing the lateral offset to a moving COP, as shown in Fig. B.6(e). The result resembles that of Protocol (a) in Fig. B.4(a); the changes in d_1 mostly affect the magnitude of body angle and moments, but the waveforms all remain qualitatively the same shape. Also, the increase in d_1 has amplified the waveforms, and the moving COP has stabilized the system even with $d_1 < 0$, in contrast to the results of Fig. B.4(a).

From the results from these protocols, we conclude that we can achieve the desired sinusoidal waveforms by laterally offsetting a fixed COP or moving COP. However, both cases produce body angle and moment variations that remain an order of magnitude smaller than those of a cockroach. This can be remedied with a very large—possibly non-physical—COP offset of $d_1 = 0.025 \text{ m} \approx 2l_0$ and $d_2 = 0$, which means that the virtual foot touchdown position will be far off to the positive x -axis in $\{B\}$ along with the COP. The resulting magnitude of the body angle was about 2° (or 0.035 rad) with the moment of $0.3 \times 10^{-4} \text{ N m}$. This is within an order of magnitude of the cockroach variations 5.7° (or 0.1 rad) and $1 \times 10^{-4} \text{ N m}$ in Fig. B.2.

B.2 Stability as a Function of Fixed COP Position

Figures B.4(a) and B.4(b) showed the stability plot of the LLS with a fixed COP along the x and y -axis of $\{B\}$, respectively. Figure B.7 shows a contour plot of the maximum non-unity eigenvalues as a function of more general 2D fixed COP positions. Note that the neutrally stable (i.e. $\max \lambda = 1$) gait corresponding to $(d_1, d_2) = (0, 0)$ found by Schmitt and Holmes [96] lies

APPENDIX B. ANALYSIS OF COP PLACEMENTS

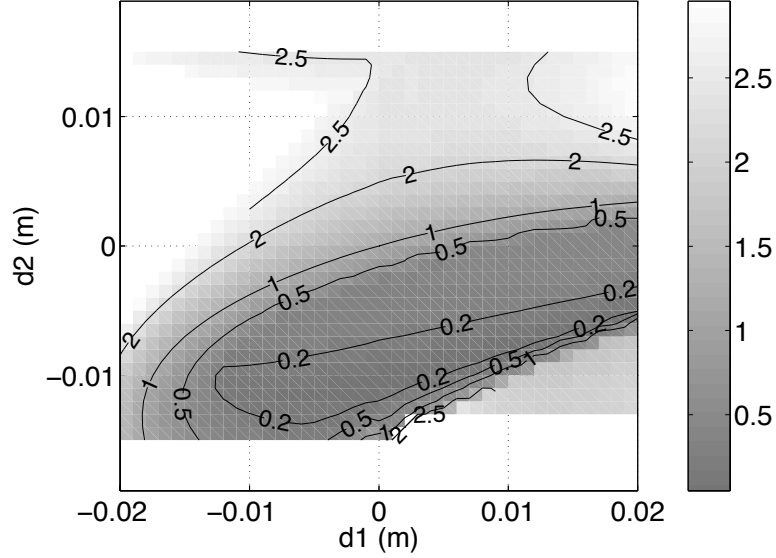


Figure B.7: Maximum eigenvalue (neglecting two invariant unity eigenvalues for energy and direction) of the linearized return map as a function of our new, two dimensional COP locations. The dark gray indicates the parameter regime of maximum stability and the neutral stability occurs when the contour reads 1. Eigenvalues greater than 3 are empty. The parameter values used are: $v = 0.25 \text{ m/s}$, $k = 2.4 \text{ Nm}^{-1}$, $l_0 = 0.01 \text{ m}$, $\beta_0 = 1 \text{ rad}$, and $-0.02 \text{ m} < d_1, d_2 < 0.02 \text{ m}$.

along a neutral stability contour through the origin of the d -plane. There is a large stable region ($\max \lambda < 1$) “inside” the neutral stability contour and an abrupt area of instability in the lower-right corner of the plot. Notice that the stable region ($\max \lambda < 1$) extends to a part of $d_2 > 0$ region for $d_1 > 0$. This indicates that we can achieve stability for the fixed COP that is in front of COM, as long as it is sufficiently offset to the right ($d_1 > 0$). We also notice that around the origin, the gradient of the eigenvalues is greater in the direction of y -axis than x -axis of $\{B\}$. This hints that a small displacement of the fixed COP in d_2 should give us a greater control than that of d_1 . We utilize this notion in Sect. 6.2.

Our long-term goal is to match the LLS to biological or robotic locomotion performance, possibly using the LLS as a plant model for control. Therefore, we examined the equilibrium state values, δ^* , θ^* , and $\dot{\theta}^*$, in Fig. B.8, as a recipe for future comparisons to biological and robotic

APPENDIX B. ANALYSIS OF COP PLACEMENTS

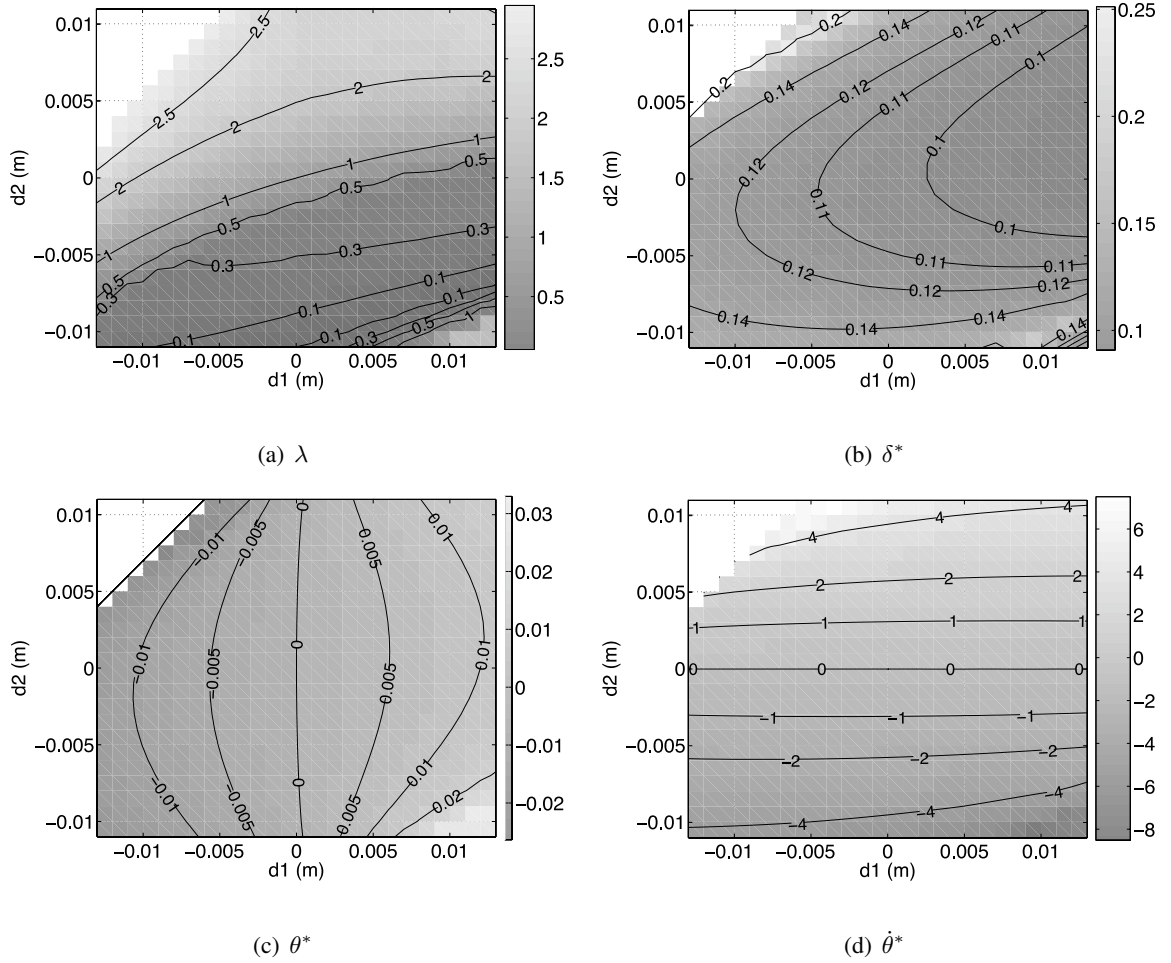


Figure B.8: Contour map of the maximum non-unity eigenvalue and the equilibrium points δ^* , θ^* , and $\dot{\theta}^*$. The parameter values are the same as Fig. B.7.

systems. As expected, the two contours $\theta^* = 0$ and $\dot{\theta}^* = 0$ indicate purely oddly symmetric (sinusoidal) and evenly symmetric (cosinusoidal) yaw motions, respectively, and these symmetries only occur on those contours.

APPENDIX B. ANALYSIS OF COP PLACEMENTS

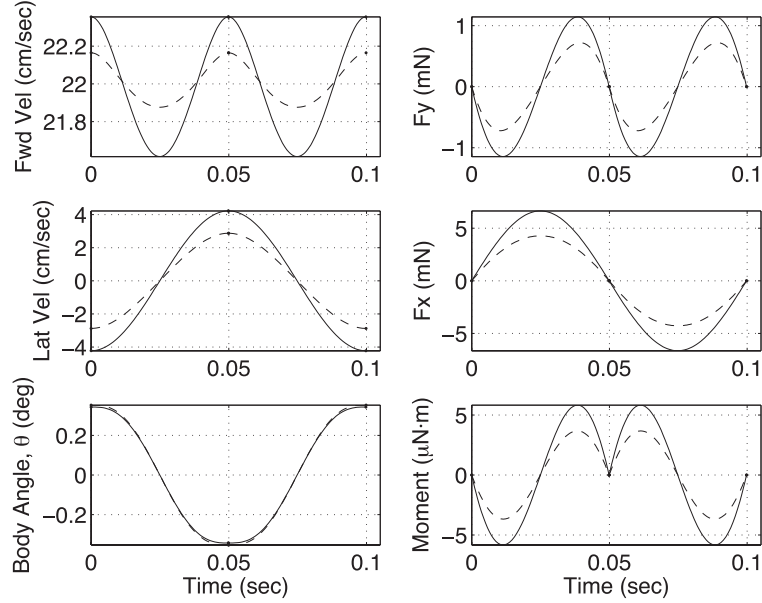


Figure B.9: Comparison between moving and fixed COP. $m = 0.0025 \text{ kg}$, $I = 2.04 \times 10^{-7} \text{ kg m}^2$, $k = 3.52 \text{ N m}^{-1}$, $\beta_0 = 1.125 \text{ rad}$. Moving COP (dashed) $v = 0.2235 \text{ m/s}$, $l_0 = 0.0082 \text{ m}$, $d_1 = 0 \text{ m}$, $d_2 = 0.002 \rightarrow -0.002 \text{ m}$. Fixed COP (solid) $v = 0.2275 \text{ m/s}$, $l_0 = 0.0128 \text{ m}$, $d_1 = 0.005 \text{ m}$, $d_2 = 0 \text{ m}$.

B.3 Comparing Fixed vs. Moving COP Models

From the observations above, we consider the relationship between a fore-aft moving COP and a fixed, laterally offset COP. These two scenarios generate similar waveforms; in fact, using very similar parameters, we can nearly match the body motions and forces using these two strategies, as shown in Fig. B.9. To find a good match, we relied on trial and error, using Figs. B.4(a) and B.5(c) as a guide to adjust d_1 and d_2 and we referred to [95] to adjust l_0 , β_0 , and k . As shown, the body angle (yaw) motions match nearly exactly, while for the other measurements, the fixed COP exceeded the moving COP somewhat in magnitude, although the results are qualitatively similar.

We compare the moving COP model to a model with a fixed COP on the positive x -axis of $\{B\}$, as follows. As the LLS moves through a left step, the leg intersects the body centerline at

APPENDIX B. ANALYSIS OF COP PLACEMENTS

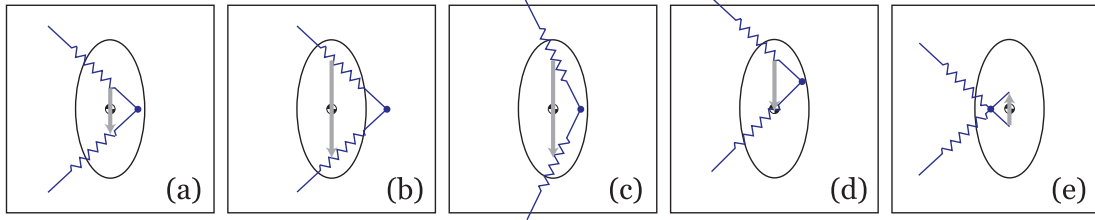


Figure B.10: Comparison between a moving COP and an effective fixed COP during a left step under different protocols. Fixed COP is denoted by a filled dot, and the moving COP is denoted by a gray arrow.

a point that moves fore-aft, as depicted in Fig. B.10(a). Suppose there is another LLS system with a moving COP that traces out the same path, and has the same foot touchdown position as the fixed COP case. With appropriate parameters (and possibly a nonlinear leg spring), the fixed COP LLS model might approximate the moving COP model. By approximating the moving COP with the fixed COP in this way, we can predict which moving COP protocols might be stable on the basis of the stability contour map (Fig. B.7, Sect. B.2). Using this approach, we address below (without formal proofs) unanswered questions from Chap. B.1.

In Protocol (c), we considered increasing the magnitude of a moving COP. We approximate this case using the effective fixed COP and effective β_0 shown in Fig. B.10(b) and (c); a larger magnitude can be created by moving the effective fixed COP in the x direction and/or decreasing the value of leg touchdown angle β_0 . From Fig. B.4(a), we saw that the increase in d_1 for a fixed COP improved stability and amplified the body angle and moment, which agrees with increasing the magnitude of fore-aft motion in the moving COP, as shown in Fig. B.5(c). Similarly, a moving COP that is shifted forward, as in Protocol (d), can be approximated by shifting the effective fixed COP forward, as shown in Fig. B.10(d). Figure B.8(a) shows that the effective fixed COP will first be stable, but eventually it will be unstable as the offset increases further.

Earlier, we indicated that the system became unstable when the moving COP moved from

APPENDIX B. ANALYSIS OF COP PLACEMENTS

back to front (i.e. aft to fore) along the body centerline. As Fig. B.10(e) shows, the effective fixed COP would then be placed on the left side of the body centerline which, according to Fig. B.8(a), would probably make the system unstable. This also suggests we can achieve stability for a forward moving COP if we choose our offsets carefully.

In Protocol (e), we increased the lateral offset of a moving COP. We can represent this simply by laterally shifting the effective fixed COP which is similar to Protocol (a), Fig. B.4(a). Indeed that is what we observed in Fig. B.6(e). This explains why the system remained stable when $d_1 < 0$; the effective fixed COP position was to the right of the COM ($d_1 > 0$). This implies that for cockroaches, if their mechanics limit the magnitude of d_2 , i.e. they cannot have a large c_2 , then an increase d_1 will achieve the desired stability, or vice versa; this would explain the shift in the moving COP observed in cockroaches [115].

In summary, the moving COP model is more complex than the fixed COP, but they have similar performance in matching biological data. Thus, in this thesis, we assume the COP is fixed to the right of the COM within each step, but let the controller adjust the location of the COP between steps.

Appendix C

Derivation of Chaplygin Sleigh Using Lagrange–D’Alembert Principle

Here we derive the equations of motion for the Chaplygin sleigh shown in Fig. 7.2. The no-slip constraint at the skate says the skate cannot slide sideways, that is, the skate’s velocity, which is given by

$$\begin{bmatrix} \dot{x} \\ \dot{y} \end{bmatrix} + \frac{d}{dt} \begin{bmatrix} d \cos \theta \\ d \sin \theta \end{bmatrix}$$

in the plane must have no projection onto $[-\sin \theta, \cos \theta]^T$, i.e.

$$\underbrace{\begin{bmatrix} -\sin \theta & \cos \theta & -d \end{bmatrix}}_{\Gamma^T} \underbrace{\begin{bmatrix} \dot{x} \\ \dot{y} \\ \dot{\theta} \end{bmatrix}}_{\dot{q}} = 0 \quad (\text{C.1})$$

APPENDIX C. DERIVATION OF CHAPLYGIN SLEIGH USING LAGRANGE–D’ALEMBERT PRINCIPLE

The COM equations of motion are given by Newton’s laws

$$\begin{bmatrix} m & 0 & 0 \\ 0 & m & 0 \\ 0 & 0 & J \end{bmatrix} \ddot{q} = \lambda \Gamma \quad (\text{C.2})$$

where the only external force is the constraint force, $\lambda \Gamma$. Note that the constraint equation (C.1)

implies that differential displacements are of the form

$$\delta q = \begin{bmatrix} \delta x \\ \delta y \\ \delta \theta \end{bmatrix} = \begin{bmatrix} 1 & 0 \\ 0 & 1 \\ -\frac{\sin \theta}{d} & \frac{\cos \theta}{d} \end{bmatrix} \begin{bmatrix} \delta x \\ \delta y \end{bmatrix} \quad (\text{C.3})$$

where $(\delta x, \delta y)$ is free. Thus, we take

$$\delta q \cdot \left(\begin{bmatrix} m & 0 & 0 \\ 0 & m & 0 \\ 0 & 0 & J \end{bmatrix} \ddot{q} - \lambda \Gamma \right) = 0 \quad (\text{C.4})$$

and note that δq is orthogonal to Γ , and $(\delta x, \delta y)$ is free. This yields

$$\begin{aligned} \begin{bmatrix} 1 & 0 & -\frac{\sin \theta}{d} \\ 0 & 1 & \frac{\cos \theta}{d} \end{bmatrix} \begin{bmatrix} m & 0 & 0 \\ 0 & m & 0 \\ 0 & 0 & J \end{bmatrix} \ddot{q} &= 0 \\ \implies m\ddot{x} - \frac{\sin \theta}{d} J\ddot{\theta} &= 0 \\ m\ddot{y} + \frac{\cos \theta}{d} J\ddot{\theta} &= 0 \end{aligned} \quad (\text{C.5})$$

Differentiating the constraint equation, we have

$$-\dot{\theta} \underbrace{\begin{bmatrix} \cos \theta & \sin \theta \end{bmatrix}}_v \begin{bmatrix} \dot{x} \\ \dot{y} \end{bmatrix} + \begin{bmatrix} -\sin \theta & \cos \theta \end{bmatrix} \begin{bmatrix} \ddot{x} \\ \ddot{y} \end{bmatrix} - d\ddot{\theta} = 0 \quad (\text{C.6})$$

APPENDIX C. DERIVATION OF CHAPLYGIN SLEIGH USING
LAGRANGE–D’ALEMBERT PRINCIPLE

where $v \in \mathbb{R}$ is the forward speed. Multiplying the equations (C.5) by $\sin \theta$ and $-\cos \theta$, respectively, and adding them together with m times (C.6), we have

$$\begin{aligned} m\ddot{x} \sin \theta - \sin^2 \theta \frac{J}{d} \ddot{\theta} - m\ddot{y} \cos \theta - \cos^2 \theta \frac{J}{d} \ddot{\theta} - m\dot{\theta}v - m \sin \theta \ddot{x} + m \cos \theta \ddot{y} - md\ddot{\theta} &= 0 \\ -\frac{J + md^2}{d} \ddot{\theta} - mv\dot{\theta} &= 0 \\ \implies \ddot{\theta} &= -\frac{md}{J + md^2} v\dot{\theta} \end{aligned}$$

Finally, noting that $v = \dot{x} \cos \theta + \dot{y} \sin \theta$, we have

$$\dot{v} = \underbrace{(\ddot{x} \cos \theta + \ddot{y} \sin \theta)}_{\overset{0}{\cancel{\text{ }}} + \underbrace{(-\dot{x} \sin \theta + \dot{y} \cos \theta)}_{d\dot{\theta}} \dot{\theta} = l\dot{\theta}^2$$

The fact that the first term cancels to zero can be seen by multiplying (C.5) by $\frac{1}{m}[\cos \theta, \sin \theta]$.

Letting $\omega = \dot{\theta}$, and putting it all together, we have

$$\begin{aligned} \dot{v} &= d\omega^2 \\ \dot{\omega} &= -\frac{md}{J + md^2} v\omega \end{aligned} \tag{C.7}$$

This has equilibria of $(v, \omega) = (v_0, 0)$. The linearization is given by

$$\begin{bmatrix} \dot{\tilde{v}} \\ \dot{\tilde{\omega}} \end{bmatrix} = \begin{bmatrix} 0 & 0 \\ 0 & -\frac{md}{J+md^2} v_0 \end{bmatrix} \begin{bmatrix} \tilde{v} \\ \tilde{\omega} \end{bmatrix}$$

which has a zero eigenvalue and an eigenvalue with sign opposite to v_0 . We cannot conclude that this is stable from the linearization due to the zero eigenvalue. However, the system is nevertheless stable, because energy is conserved, so $mv^2 + J\omega^2 \equiv E_0 = \text{constant}$, i.e.

$$v = \pm \sqrt{(E_0/m) - (J/m)\omega^2} \tag{C.8}$$

So, as $\omega \rightarrow 0$ in a neighborhood of $\omega = 0$, v can only change by a small amount.

Part II

Human Locomotion

Chapter 9

Motivation

Healthy humans adapt their gait when walking on a split-belt treadmill—a treadmill that has separate belts for the left and right legs with independent speed controls [83]. During the initial phase of walking on the split-belt treadmill with one belt going faster than the other, the subjects, not having been acclimated to walk on the treadmill, exhibit asymmetric interlimb coordination (phasing of the two legs) resulting in a limping gait Fig. 9.1 [83]. Adaptation, without the subjects' conscientious effort, takes place gradually over the course of several minutes, leading to a more symmetric interlimb coordination. The indication that learning takes place is that when the subjects are asked to walk on a tied treadmill (i.e., both belts turning at the same speed like a typical exercise treadmill) after the adaptation: although temporarily, the subjects exhibit a limping gait! For patients with cerebral damage, this after-effect can be beneficial: they temporarily stop limping.

In Part II of this thesis, we seek to understand how our bodies adapt during this locomotor task. We identify different facets of human feedback control through various perturbations using the split-belt treadmill.

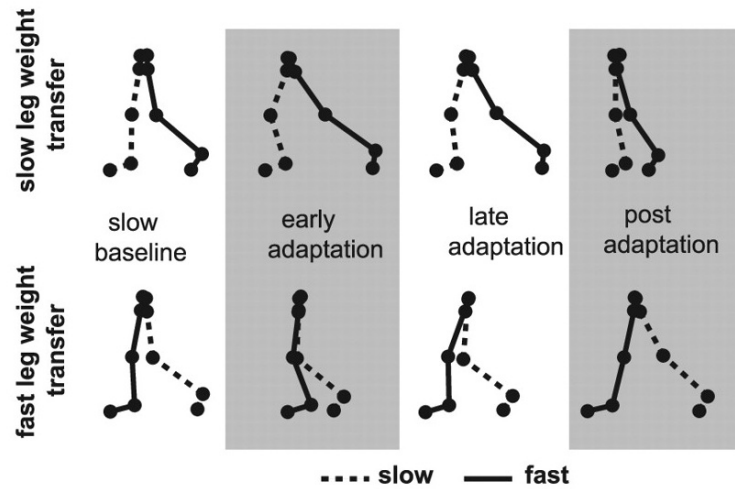


Figure 9.1: Leg kinematics at slow (first row) or fast (second row) leg touchdown. During *slow baseline* the subject has similar leg kinematics. During *early adaptation* the split-belt condition causes different shapes at fast or slow touchdowns. During *late adaptation* the legs become more symmetric. During *post adaptation* the learning has retained and causes asymmetric gait even though the belts are turning at the same speed. (Image credit: [83]; used with permission)

9.1 Biology: Humans

9.1.1 Gaits

In a paddock, horses employ one of three gaits to move around at different speeds (Fig. 9.2, right axis): walk (1-1.5 m/s), trot (2.5-4 m/s), and gallop (5-6 m/s) [51]. These gaits are defined by observing relative phasing of the four legs [39]. Why are their preferred speeds clustered around those three regions? Why do they need different gaits for different speeds? Why not “walk” at all speeds? After training horses to move at a gait beyond their preferred speeds, Hoyt and Taylor [51] measured the horses’ rate of oxygen consumption to assess their metabolic rate at different speed and gait combinations. Their results (Fig. 9.2, left axis) showed that horses change their gait to minimize their metabolic rate.

Two of the gaits employed by humans are walking and running. Walking is defined as

CHAPTER 9. MOTIVATION

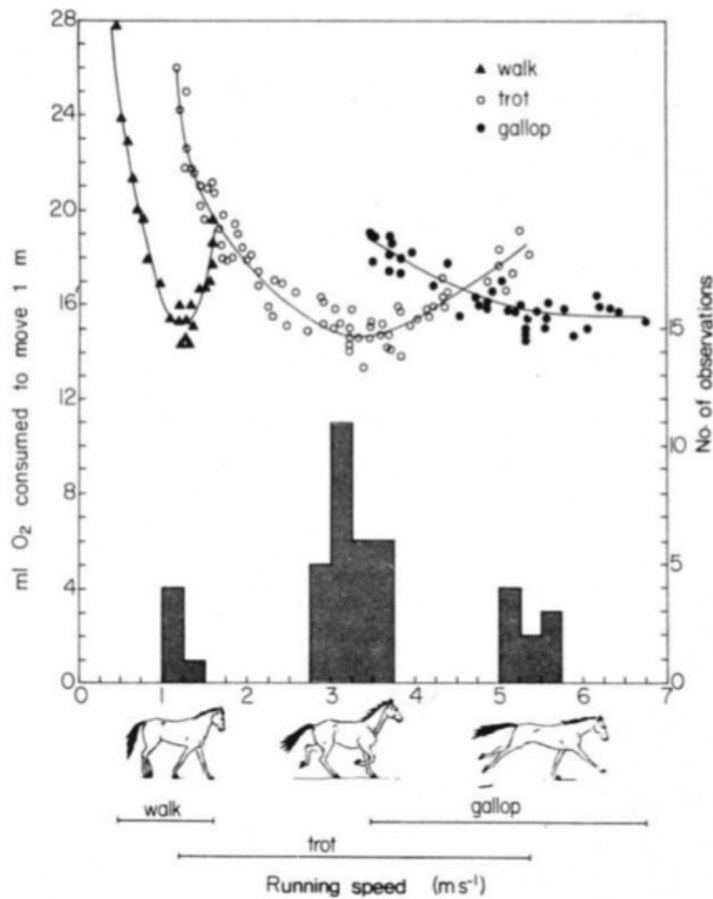


Figure 9.2: Oxygen consumption rate as a function of gait and speed. Notice the minimum of those three curves are indeed the preferred speeds and gaits for those horses. (Reprinted by permission from Macmillan Publishers Ltd: Nature [51], copyright 1981)

a gait where the kinetic energy of the COM and the gravitational potential energy are anti-phase; running is defined as a gait where the two energies are in-phase. Alternatively, walking can be defined as a gait with more than 0.5 duty cycle and running with less than 0.5 duty cycle, where a duty cycle is defined as (stance time of a leg)/(stride time). During walking, the trajectory of the COM produces semi-circular arcs; running can be represented by a hopping pogo stick. Similar to the results of Hoyt and Taylor's experiment, humans exhibit gait transitions from walking to running at a speed (~ 2.2 m/s) where oxygen-consumption curves for walking and running cross

CHAPTER 9. MOTIVATION

each other [70].

One explanation for why humans cannot maintain walking gait at high speeds can be easily understood in terms of an inverted pendulum under the force of gravity. Near vertical, the centripetal acceleration is v^2/ℓ , where v is the linear velocity of the COM (walking velocity) and ℓ is the length of the pendulum (a human hip height). If v increases such that the centripetal acceleration exceeds the downward acceleration from gravity g , then the COM will vault and the leg will lose its contact with the ground. If we divide the centripetal acceleration by g , we get a dimensionless parameter called the Froude number, $\frac{v^2}{g\ell}$. For humans with leg length of 0.9 m, the walking speed v at which the Froude number exceeds 1 (i.e., start to vault) is 3 m/s, which is close to an observed maximum human walking speed [1].

But for higher speeds, why do humans run instead of vault our way forward? Srinivasan and Ruina [109] show that running and walking gaits naturally arise to minimize metabolic cost of operating a prismatic-actuated pendulum while achieving a desired forward speed. Their results suggest a simple mechanistic explanation for why we run instead of vault but also why we walk in the first place at lower speeds.

9.1.2 Mechanics and Control of Locomotion

The tasks of walking and running rely on a neuromechanical system, coupled with force interaction with a static or dynamic environment. The process by which humans achieve muscle coordination to produce locomotive behavior is shown in Fig. 9.3. Although human brains, containing more than 100 billion neurons, have well-defined regions, the details of their function are unknown. Pathways between regions in the brain are necessary not only to achieve locomotion but also to perform basic human functions. Various sensory signals, such as those delivered along visual, au-

CHAPTER 9. MOTIVATION

ditory, vestibular, and cutaneous afferents, are integrated and processed through different regions in the brain to induce or alter locomotive patterns (Fig. 9.3(A)). The processed commands are then sent to the interneurons and motorneurons in the spinal cord to modulate and shape locomotive patterns. Finally, the motorneurons activate muscles in the legs in a coordinated manner and yield the final locomotive behavior (Fig. 9.3(B)). To understand this complex array of neuronal connections and signals, we can examine the process at different timescales during locomotion.

Within one- to two-step timescales Oscillatory motions of our legs during running are attributed to a collection of interneurons (called a central pattern generator, or CPG) in our spinal cord (Fig. 9.3(B)). This collection of interneurons is capable of generating basic rhythmic patterns without inputs from the brain and proprioceptive/cutaneous afferents; the descending and reflex inputs from both legs shape and modulate the CPG to provide rapid responses to dynamic and noisy environmental conditions [112]. Along with these basic rhythmic signals are muscle synergies: multiple leg muscles are activated in a coordinated manner from a lower dimensional command. These spinal reflexes and muscle synergies create a basic locomotive, self-stabilizing behavior. CPG's, reflexes (tuned musculoskeletal mechanics [33]), and reflexes place less demand on the higher centers of the brain and allow humans to operate at high speeds, when such operation from the brain would have otherwise been prohibitive due to neural transmission delays.

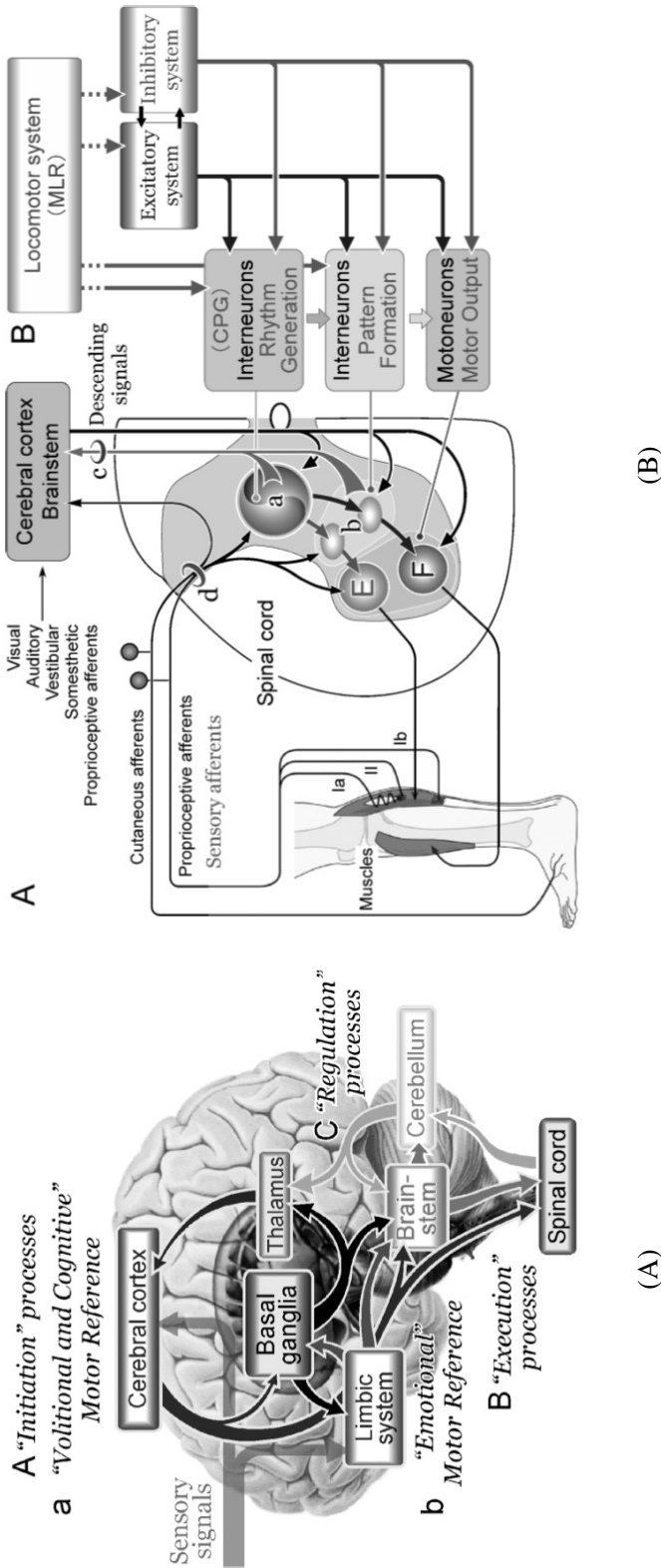


Figure 9.3: (A) A general overview of active pathways in the brain during motor control. Sensory signals (e.g., vision through thalamus or proprioception through the spinal cord) are integrated into the cerebral cortex and limbic system where movements are first initiated. Basic movements are executed in the brainstem and spinal cord which are refined and regulated by the cerebral cortex, basal ganglia, and cerebellum. [112] (Image credit: [112]; reprinted by permission from Koninklijke Brill NV) (B) A general overview of active pathways in the spine during locomotor movements. The descending commands from the brain adjust the interneurons and motoneurons in the spine to modulate the rhythm (generated by the central pattern generator) and pattern of locomotion. The sensory afferents (cutaneous and proprioceptive), in addition to their connections to the supraspinal structures, are directly connected to interneurons and motoneurons in the spine. [112] (Image credit: [112]; reprinted by permission from Koninklijke Brill NV)

CHAPTER 9. MOTIVATION

Within two- to ten-step timescales Task-level control during running (e.g., following a curved line) is mediated by the higher centers of the brain, integrating messages from visual, vestibular, and other sensory afferents (Fig. 9.3) [79]. Due to neural processing and transmission delays, the recovery rate at this level operates at a slower time scale, with comparatively less-frequent descending commands than from the spinal neural network. However, as discussed above, this delay may be accounted for through the inherent stability in the low-level system (CPG, reflexes, and reflexes) or through the use of predictive mechanisms in the cerebellum [7].

More than ten-step timescales Human motor adaptation and learning operate at the slowest timescales. Researchers attribute basic motor learning capability to the cerebellum [61]. Furthermore, learning can occur simultaneously at different timescales [107]. One hypothesis in the function of the cerebellum is that with an internal representation of body dynamics, the cerebellum uses observed discrepancies between the expected sensory afferents and the actual received sensory afferents to alter its internal representations, until the discrepancy is removed. The details of these operations, however, are not well known. For example, what exactly are the set of sensory signals responsible for adaptation (e.g., visual flow, sound of the treadmill, holding of the rail, the need to stay on the treadmill)?

To understand learning as well as introduce some of the terminologies to be used in the remaining part of this thesis, we consider our motivating example by Reisman et al. [83]. Reisman et al. used a split-belt treadmill to create a constant asymmetric perturbation. Healthy subjects walked on a *tied-belt* condition (when both belts were turning at the same speed), then walked on a *split-belt* condition (where one belt was going faster than the other) for 10 minutes. During the first few minutes of walking (*early-adaptation*) subjects limped because they were not accustomed

CHAPTER 9. MOTIVATION

to walking in such condition. Here, the limping motion is defined as an asymmetry in the left and right step lengths where a left step length is the distance between two feet at the left foot heel strike and a right step length is the distance between the two feet at the right foot heel strike. As shown in Fig. 9.1, the subjects eventually changed their gait by altering the interlimb coordination, e.g., leg touchdown angle relative to the other leg. After 10 minutes (*late-adaptation*) the subjects walked in a more symmetric gait, leading to similar step lengths for both legs. The evidence for *learning* was observed when they walked on a tied-belt after the training: the subjects temporarily exhibited a limping gait (*after effect*). But eventually the gait improved (*wash-out*) back to their normal symmetrical gait. Choi and Bastian [19] showed that similar adaptation behavior occur in running.

These different time-scale operations show diverse strategies that our CNS and musculoskeletal system employ spatially (CPG's are located in the spine and not further away near the higher centers of the brain) and temporally.

9.2 Modeling: Human Movement

Using a spring-loaded inverted pendulum (SLIP) as a template (Chapter 1), Seyfarth et al. [105] reported that for high speeds, SLIP model can attain passive stability; Rummel and Seyfarth [87] showed that a two-segment leg model with a torsional spring at the knee joint attained passive stability at even lower speeds. Seyfarth et al. [106] showed that a constant-speed leg retraction strategy which further improved SLIP's "passive" stability.¹ Güther et al. [43] showed that when people are perturbed in stepping heights, human control strategy resembles that of these "al-

¹Passive is a slight oversimplification: some neural feedback is required, for example to detect lift-off and to regulate the swing leg to achieve a desired touch-down angle.

CHAPTER 9. MOTIVATION

most” passive-control strategies used to maintain a stable running with minimal neural feedback. Daley and Biewener [24] examined within-step energy recovery strategies of guinea fowls using step-down perturbations. Jindrich and Full [55] showed that the peak ground reaction forces from lateral impulse perturbation were quicker than what neural mechanisms could explain, suggesting that reflexes (tuned musculoskeletal mechanics) play a significant role in stabilization.

A more formal stability characterization has been performed on human walking: dynamic stability of human walking [52] was quantified under the effects of space flights [71], the effects of walking speed [29], the effects of vision [8], the effects of lateral perturbation [75], the control of angular momentum balance [48], and the effects of walking on a treadmill versus overground [26]. However, to the best of our knowledge, this thesis presents the first approach to identify directly the dynamics of human running through systematic perturbation experiments.

9.3 Roadmap

The goal of the next two chapters is to identify task-level feedback control strategies used by humans during split-belt running at different stages of adaptation. In Chapter 10, we begin (Section 10.1.1) by reviewing the SLIP model and introduce notations and coordinate transformations used for the remaining part of this thesis. In Section 10.2.2, using a SLIP model as our template for human running and a deadbeat feedback control, we generate possible control strategies that humans might employ during early adaptation of split-belt running.

In Chapter 11, we address two of the challenges addressed in Chapter 10. We gain insight on how humans recover from perturbations by fitting a linear model to running data and see how the recovery rates (eigenvalues) change as a function of running speed and during late adaptation.

9.4 Dissemination

The majority of what is reported in this dissertation has been presented in the following conferences:

- J. Lee, J. Choi, A. Bastian, and N. Cowan, "Fitting the Closed-Loop Dynamics of Human Running on a Split-Belt Treadmill," Society for Integrative and Comparative Biology, Boston, MA, Jan 3-7, 2009;
- J. Lee, J. Choi, S. Carver, A. Bastian, and N. Cowan, "Toward a Neuromechanical Model for Adaptation and Control of Human Running," Fourth International Symposium on Adaptive Motion of Animals and Machines, Cleveland, OH, June 1-6, 2008.

Chapter 10

Spring-Loaded Inverted Pendulum

(SLIP) Model With Deadbeat Feedback

Control

In this chapter, we make two basic assumptions: (1) humans run with a control target of spring-loaded inverted pendulum (SLIP) template and [9, 100] (2) humans use a one-step deadbeat feedback control strategy during *overground* running (deadbeat in y suggested by Chapter 11). Using these assumptions, we ask how humans might control running when they encounter the split-belt condition for the first time (without adaptation). Do humans quickly alternate between two controllers or do they use just one type of controller? To address this question, we begin by a brief review of the SLIP model in Sections 10.1.1 and 10.1.2. In Section 10.1.3, we discuss one of many differences between overground running and treadmill running and how the difference may lead to different feedback control strategies between the two settings. In Section 10.2 we introduce

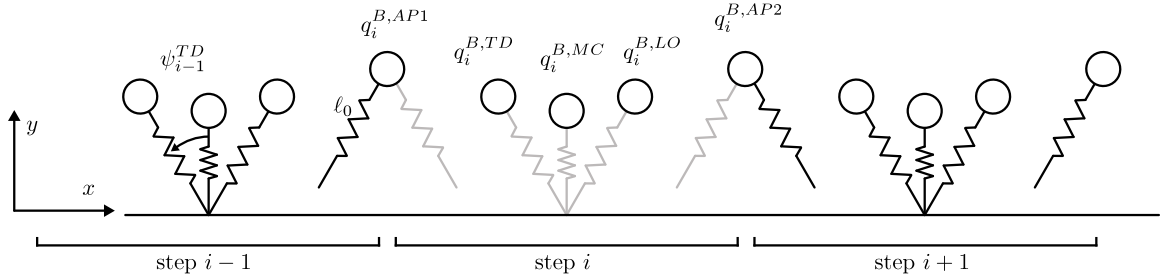


Figure 10.1: Overground running of the SLIP model (moving from left to right). Each i -th step has five phases denoted in superscripts: AP1, apex prior to i -th stance; TD, touchdown; MC, maximum compression; LO, liftoff; AP2, apex after i -th stance. A black spring leg represents one leg and a gray spring represents the other leg.

the deadbeat feedback controller and discuss how humans might employ different feedback control strategies. We compare our SLIP simulations under different control strategies to human trial data in Section 10.3.

10.1 SLIP Model and Simulation

10.1.1 Review: SLIP Model

The spring-loaded inverted pendulum (SLIP) has been a convenient template for control [9, 50]. Unlike the lateral leg spring (LLS) model (Chapter 6), SLIP tries to capture animal running dynamics in the sagittal plane [9, 101] or in 3D [14, 103].

The SLIP model is a point mass with a massless prismatic spring leg (Fig. 10.1) that bounces like a pogo stick. When the SLIP is in contact with the ground, it is said to be in a *stance phase*; when airborne, it is said to be in a *flight phase*. Alternating between the two phases produces a forward running motion. When the model is in flight phase, it prepares for the next step by placing its next leg at a predefined length and angle.

As shown in Fig. 10.1, steps are indexed by a subscript i . Associated to an i -th step

CHAPTER 10. SLIP MODEL WITH DEADBEAT FEEDBACK CONTROL

or stance, there are five well-defined phases: (1) apex prior to the stance ($AP1$; instant that COM attains its maximum height), (2) touchdown (TD ; instant that a foot makes contact with the ground), (3) maximum compression (MC ; instant that the COM is closest to the stance foot), (4) liftoff (or toe off) (LO ; instant that the stance foot leaves the ground), and (5) the apex after the stance ($AP2$).

10.1.2 SLIP: Equations of Motion

During the flight phase, we simply model the dynamics of the SLIP model as a freely falling mass and we use COM forward position x , height y , forward speed \dot{x} , and vertical speed \dot{y} as our state:

$$\ddot{x} = 0 \tag{10.1}$$

$$\ddot{y} = -g.$$

During the stance phase, we have a spring-mass system (for convenience, using generalized coordinates):

$$m\ell^2\ddot{\psi} + 2m\ell\dot{\psi} - gml \sin(\psi) = 0 \tag{10.2}$$

$$m\ddot{\ell} - m\ell\dot{\psi}^2 + k(\ell - \ell_0) + gm \cos(\psi) = 0.$$

where ψ is the leg angle, ℓ is the leg length, ℓ_0 is the rest leg length, k is the leg stiffness, g is the gravity, and m is the mass.

The simulation of a running SLIP model alternates between (10.1) and (10.2): the simulation switches from (10.1) to (10.2) when the COM reaches the height of the next touchdown. During the stance phase, the leg spring compresses and decompresses; when the leg length returns back to its rest length, the next iteration of (10.1) and (10.2) ensues.

10.1.3 Tied-Belt Treadmill vs. Overground Running

In general, many differences exist (e.g., optic flow and head wind) between overground locomotion and *tied-belt* treadmill locomotion [26]. From a feedback control perspective, a new goal is imposed on a human subject when using a treadmill: the subject has to maintain steady fore-aft position to avoid hitting the treadmill railing in the front or to avoid falling off the back of the treadmill. When translated to overground running, this constraint is much like you running next to another runner who is running at a constant speed; if you drift forward, you must slow down, and if you drift back, you must speed up to run side by side with the other runner.

To address the aforementioned difference between treadmill and overground running, we define two reference frames: the position of a subject running on a treadmill (1) observed from a fixed frame on the ground (W ; world frame) and (2) observed from a fixed frame attached to the belt of the treadmill (B ; belt frame). For the belt frame, it might be helpful to assume that the treadmill has a sufficiently long belt (e.g., moving airport walkways) so that the frame attached to the belt does not loop back. For now, we assume that there is just one belt for both legs and that the belt is moving at a constant speed v_0 . Using W and B to denote reference frames where appropriate along with the notation defined in Section 10.1.1, we define the following:

- $t_{step,i}(\text{steptime}) \triangleq t_i^{AP2} - t_i^{AP1}$;
- $t_{stance,i}(\text{stancetime}) \triangleq t_i^{LO} - t_i^{TD}$;
- $x_i^{W,AP1}$ is the forward position (w.r.t. the “world” frame) of the runner at apex prior to i -th stance. Obviously $x_i^{W,AP1} \equiv x_{i-1}^{W,AP2}$;
- $x_i^{B,AP2} = x_i^{B,AP1} + (t_i^{AP2} - t_i^{AP1})v_0$; forward position of the COM written w.r.t. the belt

CHAPTER 10. SLIP MODEL WITH DEADBEAT FEEDBACK CONTROL

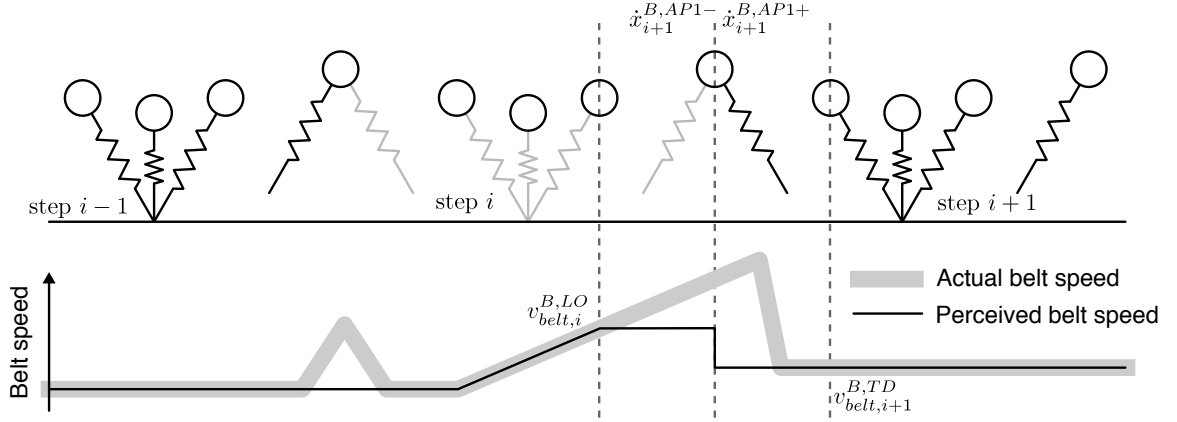


Figure 10.2: Comparison between the actual belt speed and the perceived belt speed. The upper figure is the same as the one shown in Fig. 10.1; the figure is not drawn to match the changing belt speeds. The lower figure shows the the actual belt speed (thick gray line) and our assumed perceived belt speed (thin black line). This shows that the belt speed during the flight phase is composed by $v_{belt,i}^{LO}$ and $v_{belt,i+1}^{TD}$ and does not depend on the actual belt speed.

frame;

- y_i^{AP1} is the height of the runner at apex prior to i -th stance. Note, $y_i^{W,AP1} \equiv y_i^{B,AP1}$ and $y_i^{AP1} \equiv y_{i-1}^{AP2}$;
- $\dot{x}_i^{W,AP1}$ is the forward speed (seen from ground) of the runner at apex prior to i -th stance. Note, $\dot{x}_i^{W,AP1} \equiv \dot{x}_{i-1}^{W,AP2}$;

Now suppose that the treadmill is allowed to have a piecewise linear speed profile. As shown in Fig. 10.2, the only speeds that matter to the SLIP model during the aerial phase is its stance phase belt speeds; changes during the flight phase do not affect the SLIP model. To account for ambiguities in the belt speed, we introduce “perceived belt speed,” as shown in the thin black line in Fig. 10.2; the perceived belt speed during LO to AP2 is the actual belt speed at liftoff, v_{belt}^{LO} , and the perceived belt speed during AP1 to TD is the actual belt speed at touchdown, v_{belt}^{TD} . The perceived belt speed could have been changed anywhere between the LO and TD. Note that an

CHAPTER 10. SLIP MODEL WITH DEADBEAT FEEDBACK CONTROL

implicit assumption is that the SLIP ignores the belt acceleration at its liftoff that could provide a cue for the belt acceleration that it will encounter next. From here on, belt speed is referred to in the “perceived” sense. Since there may be a jump in the belt speed at apex (e.g., the apex following step i in Fig. 10.2), we use $+$ or $-$ to distinguish the apex state before ($AP1-$) and after ($AP1+$) the jump. For that we have the following additional notions:

- $v_{belt,i}^{TD}$ is the treadmill speed at i -th stance touchdown; $v_{belt,i}^{LO}$ is the treadmill speed at LO ;
- $a_{belt,i} \triangleq (v_{belt,i}^{LO} - v_{belt,i}^{TD})/t_{stance,i}$ is the averaged acceleration of the treadmill; we assume that the treadmill exhibit constant accerleration during the stance phase;
- $x_i^{B,AP2} = x_i^{B,AP1} + (t_i^{TD} - t_i^{AP1})v_{belt,i}^{TD} + (t_i^{AP2} - t_i^{LO})v_{belt,i}^{LO} + a_{belt,i}t_{stance,i}^2/2 + v_{belt,i}^{TD}t_{stance,i}$; Forward position of the COM w.r.t. a fixed frame attached on the belt;
- $\dot{x}_i^{B,AP1-}$ is the forward speed of the person at i -th apex seen from $v_{belt,i-1}^{LO}$ (not $v_{belt,i}^{AP}$). Note, $\dot{x}_i^{W,AP1} = \dot{x}_i^{B,AP1-} - v_{belt,i-1}^{LO} = \dot{x}_i^{B,AP1+} - v_{belt,i}^{TD}$.

Using these representations, we can now convert between treadmill running and overground running.

10.1.4 Tied-Belt Treadmill vs. Split-Belt Treadmill

Other than differences in the physical setup, from a modeling perspective, there is no difference between split-belt treadmill running and tied-belt treadmill running assuming (a) there are no double stances and (b) the tied-belt treadmill can change its belt speed arbitrarily fast. Using the convention introduced above (Fig. 10.2), running on a split-belt treadmill is simply running on a tied-belt treadmill with a square-waveform belt-speed profile (Fig. 10.3A). This is not the case for

walking because during double support phases, each leg is in contact with belts of different speeds; in such a case, the placement of the belt frame $\{B\}$ becomes unclear.¹

10.2 Deadbeat Feedback Control

We use Poincaré sections and return maps to assess the stability of the SLIP model [101, 14]. We select the Poincaré section when the COM reaches each apex (i.e., $\dot{y} = 0$). Then our state associated to step i reduces to $q_i^{AP1} = [x_i^{AP1}, y_i^{AP1}, \dot{x}_i^{AP1}]$. The return map from q_i^{AP1} to q_{i+1}^{AP1} is

$$q_{i+1}^{AP1} = h_s(q_i^{AP1}, u_i) \quad (10.3)$$

where u_i is the control input (e.g., leg touchdown angle) and the subscript s indicates “slow belt.” The return map’s equilibrium point is denoted $(q_{s,*}, u_{s,*})$.

The return map for another belt speed (fast) would be (dropping AP1 to avoid clutter)

$$q_{i+1} = h_f(q_i, u_i) \quad (10.4)$$

with the corresponding equilibrium point at $(q_{f,*}, u_{f,*})$.

10.2.1 Deadbeat Control

An asymptotic controller brings a system’s state to its equilibrium asymptotically; that is, the state approaches the equilibrium as time grows but it will never reach the equilibrium in a finite time. In comparison, a deadbeat controller [14, 82] brings the state to its equilibrium in a finite time. In this section, we find a control law $u_i = g_s(q_i)$ such that it brings the apex state (10.3) to its

¹This additional information during double stance phases (direct measurement of differences in belt speeds) may promote faster adaptation.

CHAPTER 10. SLIP MODEL WITH DEADBEAT FEEDBACK CONTROL

equilibrium in one step. That is, we find $g_s(q_i)$ such that

$$q_{s,*} = q_{i+1} = h_s(q_i, u_i = g_s(q_i)). \quad (10.5)$$

To do so, we linearize our return map to find the deadbeat controller. Linearizing (10.3), we get

$$q_{i+1} = h_s(q_i, u_i) = \underbrace{h_s(q_{s,*}, u_{s,*})}_{q_{s,*}} + \left. \frac{\partial h_s}{\partial q_i} \right|_{(q_{s,*}, u_{s,*})} (q_i - q_{s,*}) + \frac{\partial h_s}{\partial u_i} (u_i - u_{s,*}) \quad (10.6)$$

$$q_{i+1} - q_{s,*} = \frac{\partial h_s}{\partial q_i} (q_i - q_{s,*}) + \frac{\partial h_s}{\partial u_i} (u_i - u_{s,*}) \quad (10.7)$$

$$= \underbrace{\frac{\partial h_s}{\partial q_i}}_A (q_i - q_{s,*}) + \underbrace{\frac{\partial h_s}{\partial u_i}}_B \underbrace{\frac{\partial g_s}{\partial q_i}}_K (q_i - q_{s,*}) \quad (10.8)$$

$$0 = q_{i+1} - q_{s,*} = (A + BK)(q_i - q_{s,*}) \quad \text{(Deadbeat)} \quad (10.9)$$

In order to achieve deadbeat, we select K such that $(A + BK)$ becomes zero. If the size of the input u_i and the states q_i are the same, we can find K by

$$\frac{\partial g_s}{\partial q_i} \equiv K = -B^{-1}A = -\left(\frac{\partial h_s}{\partial u_i}\right)^{-1} \frac{\partial h_s}{\partial q_i}. \quad (10.10)$$

Inserting K (10.10) into the Taylor series expansion of our deadbeat controller yields

$$u_i = g_s(q_i) = g_s(q_{s,*}) + \frac{\partial g_s}{\partial q_i} (q_i - q_{s,*}) \quad (10.11)$$

$$= \underbrace{g_s(q_{s,*})}_{u_{s,*}} - \left(\frac{\partial h_s}{\partial u_i}\right)^{-1} \frac{\partial h_s}{\partial q_i} (q_i - q_{s,*}). \quad (10.12)$$

From the Implicit Function Theorem, a local solution u_i to (10.5) exists if $\frac{\partial h_s}{\partial u_i}$ is not singular [14].

Now we can easily find a deadbeat controller for the fast belt:

$$u_i = g_f(q_i) = \underbrace{g_f(q_{f,*})}_{u_{f,*}} - \left(\frac{\partial h_f}{\partial u_i}\right)^{-1} \frac{\partial h_f}{\partial q_i} (q_i - q_{f,*}). \quad (10.13)$$

10.2.2 Early Adaptation Control Strategy

Suppose human subjects use $u_i = g_s(q_i)$ (slow-belt deadbeat controller) when running on a slow-belt treadmill (with $(q_{s,*}, u_{s,*})$) and use $u_i = g_f(q_i)$ (fast-belt deadbeat controller) when running on a fast-belt treadmill (with $(q_{f,*}, u_{f,*})$). What would happen if those subjects ran on the split-belt treadmill for the first time (before any adaptation)?

We simulate the SLIP model running on the split-belt treadmill using five different strategies as shown in Fig. 10.3: In (B), the model uses the slow-belt controller $g_s(q_i)$ for both legs. In (C), the model uses the fast-belt controller $g_s(q_i)$ for both legs. In (D), it selects a controller that matches what it had just experienced; this leads to wrong controller-belt matches. In (E), it selects the right controller but delayed; here, the controller is based on return maps from MC to MC². In (F), it selects the right controller all the time because it anticipates correct belt speeds and loads the right controller; the desired equilibrium trajectories and deadbeat-controller gains for the slow (s) and fast (f) belt speeds are assumed to be “stored” in the brain, and are recalled as need for the different schemes.

Before we start the simulation, we still need to decide q_* and u_* 's. As we will see in Chapter 11, humans do not achieve deadbeat in the fore-aft position $x_*^{W,AP1}$ in treadmill running. Instead we use $q_{i,*}^{B,AP1} = [x_{i,*}^{B,AP1}, y_*^{AP1}, \dot{x}_*^{B,AP1}]$ where $x_{i,*}^{B,AP1} = x_{i-1,*}^{B,AP1} + v_{belt,*} t_{step,*}$; the fore-aft control would be like controlling the fore-aft position to match the footprints on the ground. As our control input, u_i , we selected compression (k_i^c) and decompression (k_i^d) stiffnesses (representing leg braking and propulsive forces, resp.) and the leg rest length ℓ_0 .

Each of these schemes is then qualitatively and quantitatively compared to the human

²These sensory afferents may be either directly or indirectly estimated using information from, among other sensors, the neural pathways (spinocerebellar) that convey information about the whole limb orientation and limb length [80].

CHAPTER 10. SLIP MODEL WITH DEADBEAT FEEDBACK CONTROL

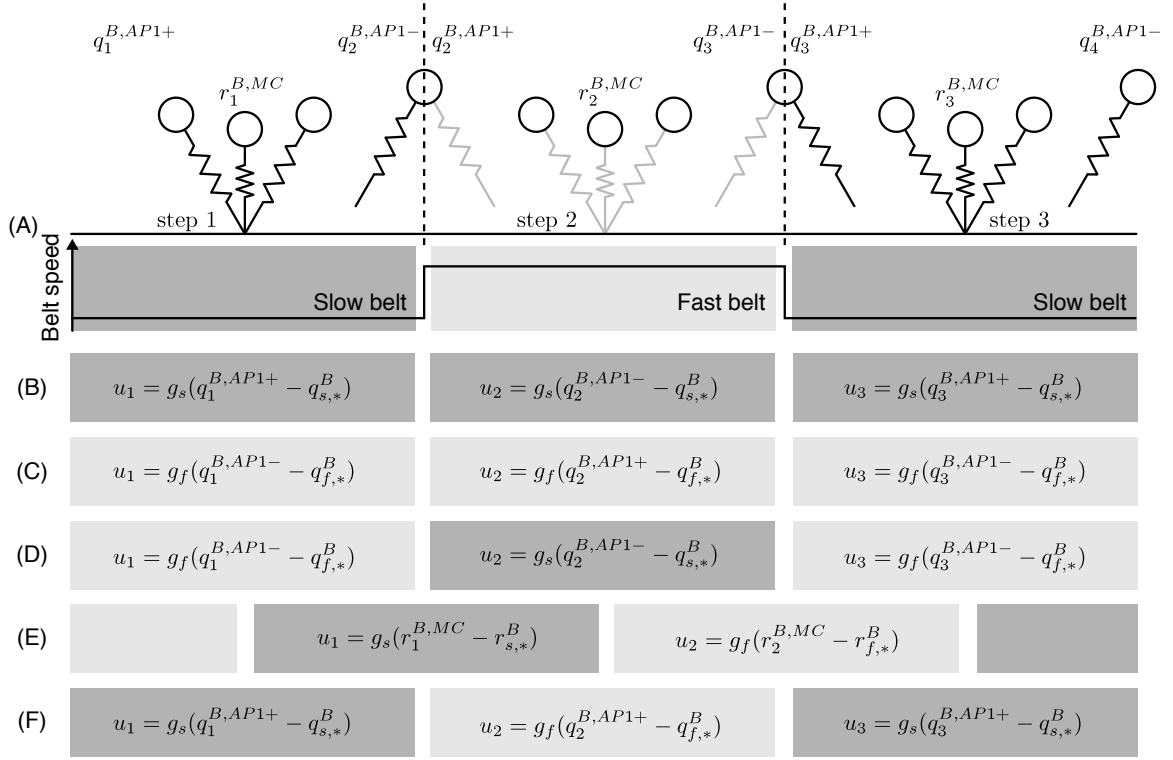


Figure 10.3: (A) Illustration of the SLIP motion under the split-belt condition. q_i 's are states at apex (AP- or AP+) and r_i 's are states at maximum compression (MC). (B)-(F) are different schemes for control during a "step." A deadbeat controller associated to the slow belt (B) or fast belt (C) is used. The rest of the controller schemes (D)-(F) alternate between slow-belt and fast-belt deadbeat controller in different phases.

trial data that were provided by Professor Amy Bastian of Department of Neuroscience at the Johns Hopkins University. Julia Choi ran the experiment; the experiment is similar to the experiment that we discuss in Chapter 11.2. Two major differences are (1) the participants for this study ran with their hands holding onto the treadmill railing and (2) the belt speed ranges were different.

10.3 Results and Discussion

10.3.1 Results: SLIP Predictions vs. Human Data

Our numerical simulations revealed that the first controller scheme [Figs. 10.3 (B), 10.5, 10.6] best represented the human trial data (Fig. 10.4). That is, the relative scale of the fast leg data to the slow leg data (either greater or less than the other) were most consistent across a multitude of observed measurements. Some of the other controller schemes produced values that were only feasible on limited split-belt speeds.

Even for the best controller scheme, not all quantities could be perfectly matched to the human trial data. For instance, there were no solutions to the 1.5m/s-3m/s split-belt velocities (Fig. 10.4). We attribute the mismatches to the simplistic assumptions made using the SLIP model and the deadbeat controller (linearization). However, the fact that one scheme in our simple framework could parsimoniously represent the general trend of the data while the other schemes failed, reveals a possible strategy that our bodies might employ.

10.3.2 Discussion

In this chapter we used a SLIP model with various compositions of deadbeat feedback controllers to assess how humans might perform under a split-belt condition without adaptation. Surprisingly one model stood out to match large portions of gait measurements from humans. We introduced two reference frames $\{W\}$ and $\{B\}$ to transform from split-belt to overground representations.

Our results on human feedback control are based on strong assumptions. Hence future research may focus on fine-tuning the detailed assumptions that we made: (1) humans may use

CHAPTER 10. SLIP MODEL WITH DEADBEAT FEEDBACK CONTROL

two-step deadbeat controller rather than one-step deadbeat controller; (2) further justification is needed to support deadbeat in the fore-aft direction $x_*^{B,AP1}$; (3) we need to identify a set of control inputs (e.g., leg hip joint) that humans utilize during running; (4) we need to identify differences in recovery strategies or rates between treadmill and overground running [26];

CHAPTER 10. SLIP MODEL WITH DEADBEAT FEEDBACK CONTROL

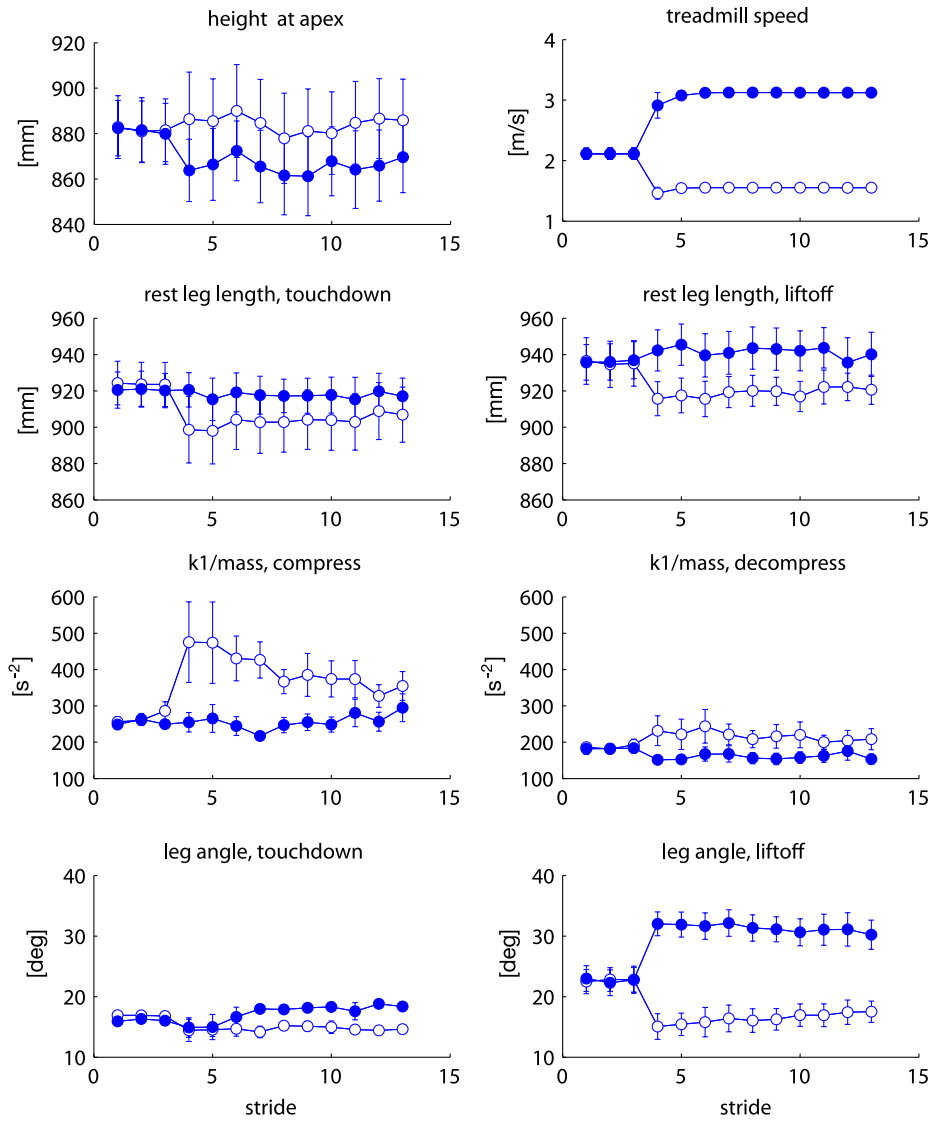


Figure 10.4: Early adaptation stage of split-belt running trial. Filled circles are the fast leg, open circles are the slow leg. The third row shows the leg spring stiffness (normalized by mass) during compression and decompression phase of the stance. The height at apex for a slow leg (fast leg, resp.) shows the apex height immediately after the slow-leg (fast-leg, resp.) liftoff.

CHAPTER 10. SLIP MODEL WITH DEADBEAT FEEDBACK CONTROL

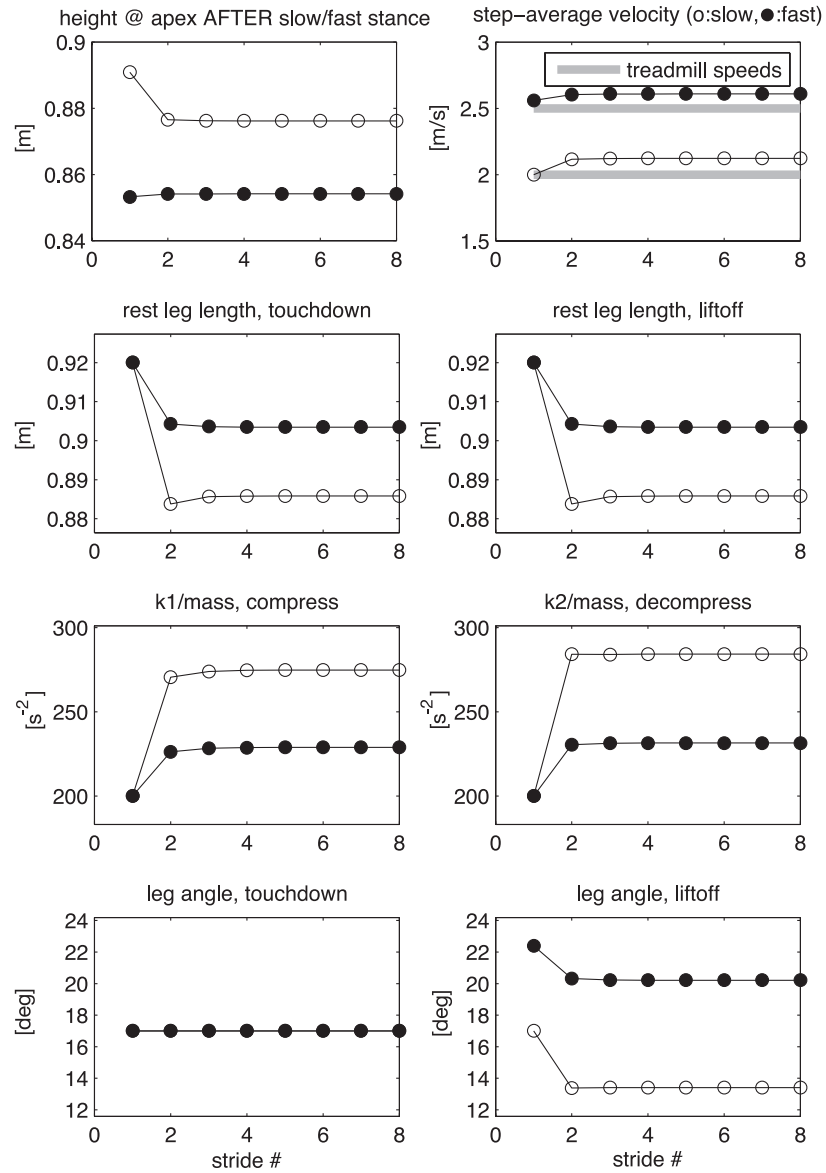


Figure 10.5: Simulation of the scheme Fig. 10.3 (B) for belt speeds 2 and 2.5 m/s. Notice that the relative scale of the fast leg data to the slow leg data are consistent with the human trial experiment shown in Fig. 10.4.

CHAPTER 10. SLIP MODEL WITH DEADBEAT FEEDBACK CONTROL

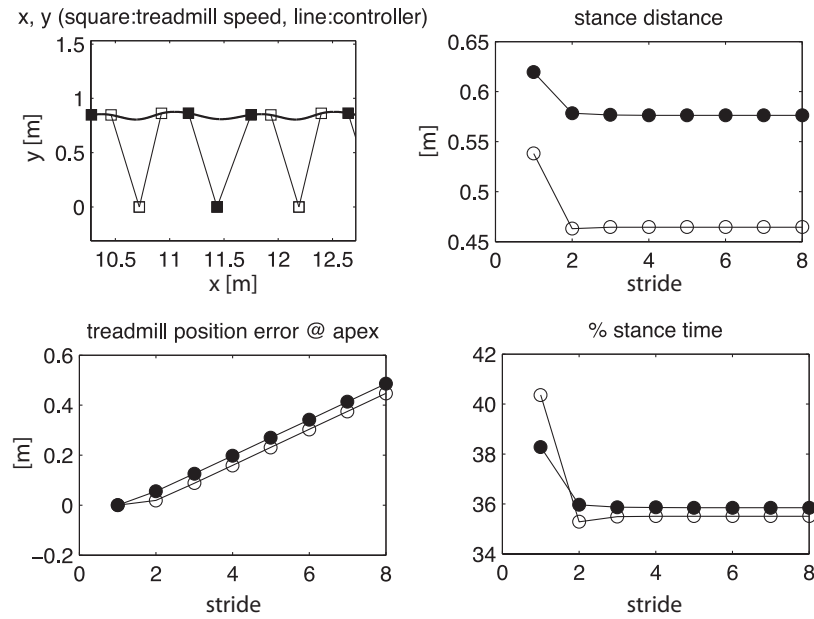


Figure 10.6: (Continuation of Fig. 10.5) The % stance time is the stance time of each leg with respect to its stride (two consecutive steps) time. The treadmill-position-error plot shows one of the mismatches of the model to the human trial: the SLIP model drifts forward when running on a split-belt treadmill.

Chapter 11

Blackbox Closed-Loop System

Identification

In this chapter, we address the overall closed-loop system's recovery rates at different speeds of tied-belt running as well as during late adaptation. To the best of our knowledge, this represents the first systematic effort to identify the stride-to-stride dynamics of human running through a set of systematic perturbation experiments.

11.1 Blackbox Model

Similar to Section 10.2, we use Poincaré return maps to assess the stability of the closed-loop system. We make a basic assumption that human subjects, in general, actively control to maintain their bodies' COM forward position x , height y , and forward speed \dot{x} from apex to apex

CHAPTER 11. BLACKBOX CLOSED-LOOP SYSTEM IDENTIFICATION

Table 11.1: Parameters for segmental analysis from [40]. Note, we omitted “Forearm, hand” and “Upper arm” segments (not listed here) discussed in [40].

Segment (proximal/distal)	% Body weight	Segment COM location from proximal endpoint
Foot (Heel/Toe)	1.8	0.506
Shank (Knee/Ankle)	4.4	0.433
Thigh (Hip/Knee)	11.2	0.433
Head, neck, trunk (Shoulder midpoint/Hip midpoint)	53.4	0.540

(following the notation introduced in Section 10.1.3):

$$q_{i+1}^{W,AP1} = A_{CL}q_i^{W,AP1} + B_w w_{belt,i} \quad (11.1)$$

$$y_i^{W,AP1} = Iq_i^{W,AP1} \quad (11.2)$$

where $w_{belt,i} \triangleq [v_{belt,i}^{TD} \ a_{belt,i}]^T$ and I is a 3 by 3 identity matrix. We perturb human running subjects by abruptly changing treadmill belt speeds. To make the system identification simpler we fit after the perturbation:

$$\begin{bmatrix} q_N^{W,AP1} & q_{N-1}^{W,AP1} & \dots & q_2^{W,AP1} \end{bmatrix} = A_{CL} \begin{bmatrix} q_{N-1}^{W,AP1} & q_{N-1}^{W,AP1} & \dots & q_1^{W,AP1} \end{bmatrix} \quad (11.3)$$

We use least squares fit to find the matrix A_{CL} . Our goal here is to identify the closed-loop feedback controller and compare the eigenvalues during slow-belt running, fast-belt running, and split-belt running (late adaptation).

11.2 Experiments: Human Split-Belt Treadmill Running

11.2.1 Experiment Setup and Data Analysis

As a preliminary study, three healthy human subjects participated for this study. All subjects gave informed written consent before participating. The data was collected with a help from Julia Choi and a courtesy of Professor Amy Bastian at the Motion Analysis Laboratory at the Kennedy Krieger Institute.

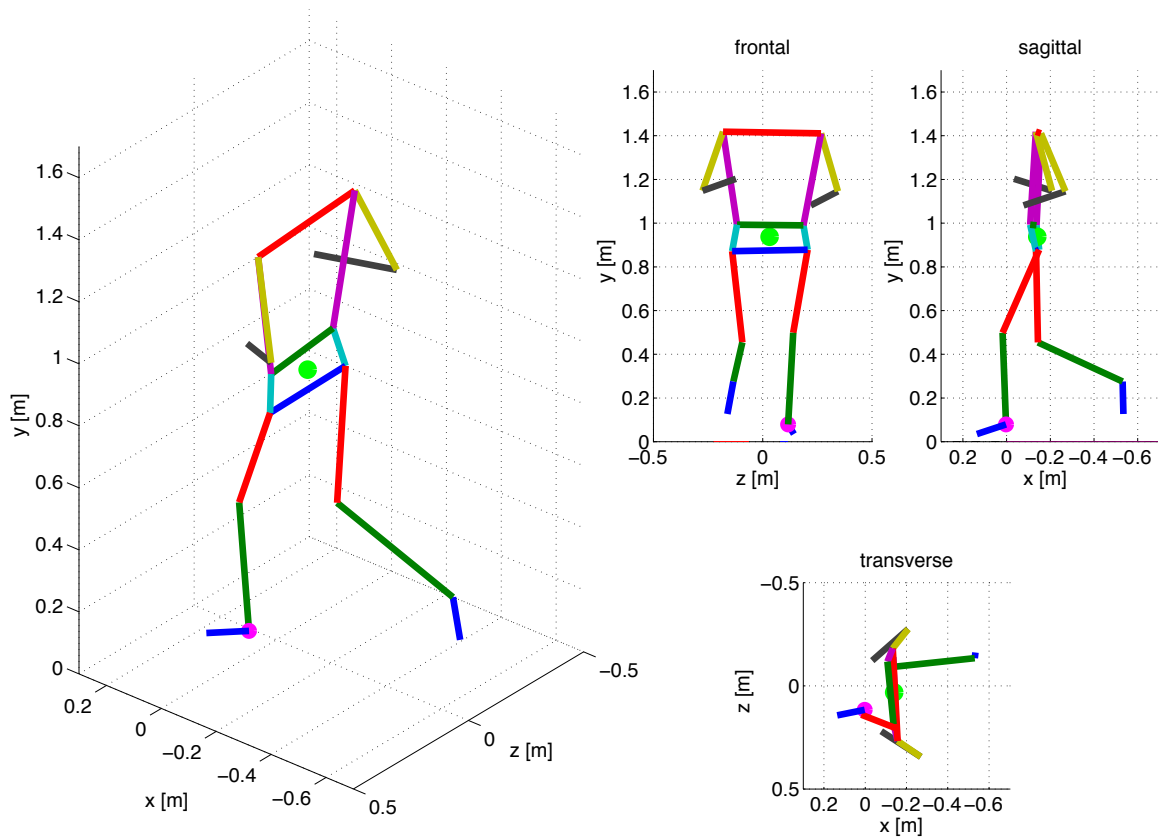


Figure 11.1: 3D kinematic data of marker positions. Note, for the actual data collection, we did not collect wrist and elbow positions because those values did not have major contributions to the overall COM dynamics. The filled green circle is the approximated COM using the segmental analysis discussed in the text.

Data acquisition The experiment setup for this study was similar to that of Reisman et al. [83]: We placed infrared (IR) markers on subjects' left and right shoulder, pelvis, hip, knee, ankle, and toe. Those markers were tracked in 3D using Optotrak (100 Hz). To detect stance phases, we used contact switches attached on the bottom of subjects' shoes (two near the front and two near the back of each shoe). The speed of the treadmill belt (encoder readings from the belt motors) and the foot contact switches were obtained at 1000 Hz. We interpolated (by a factor of 10) the kinematic tracking data using piecewise cubic splines to match the sampling rate of the treadmill belts and foot contact switches. Using the kinematic tracking data (Fig. 11.1), we approximated the COM of

CHAPTER 11. BLACKBOX CLOSED-LOOP SYSTEM IDENTIFICATION

subjects using the segmental analysis [40]; the parameter values are shown in Table 11.1.

Lateral balance The human subjects ran without holding onto the treadmill railing. Because running usually involves closer foot placements toward where the belts are split, it was important for them to maintain lateral position to avoid stepping onto the other belt during the perturbation experiment where the two belt speeds were different. To guide human subjects to run in the middle of the treadmill, a visual object was placed 4 to 5 feet in front of human subjects centered in the middle of the treadmill.

Metronome-based perturbation The experiment paradigm is illustrated in Fig. 11.2. To study how humans recover from perturbations, belt speeds were changed during their normal tied-belt and split-belt steady-state running to observe the recovery rate of human subjects. To produce consistent perturbations, we began by measuring human subjects' preferred stride frequencies (E0 phase, Fig. 11.2). Subjects were asked to synchronize their stepping patterns to match the metronome when heard; the metronome played at one of those measured frequencies. The metronome was activated for 5 to 8 consecutive strides and turned off at the onset of a perturbation; the metronome was turned off to allow subjects to recover at their own preferred cadence. The amount of time the metronome was on was randomly chosen to avoid a direct anticipation of the belt perturbations. After approximately 20 steps, the metronome started again to synchronize the stepping pattern for the next perturbation. Subjects were free to choose which leg to synchronize with to the metronome. Mostly they picked one leg and used that leg to match with the metronome for the most of their trial.

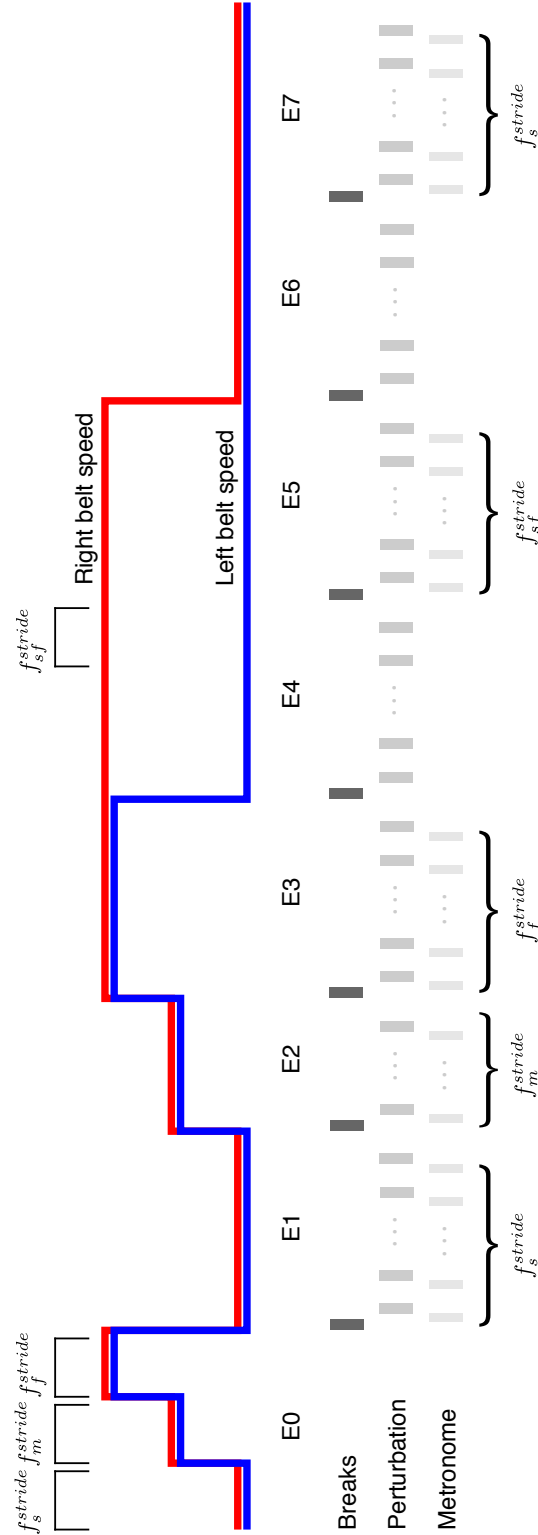


Figure 11.2: Experiment design. Red line is the right belt speed and blue line is the left belt speed. The tick marks show when the subject took breaks, when the perturbation took place, and when the metronome was on. f_s^{stride} , f_m^{stride} , f_f^{stride} , and f_{sf}^{stride} are stride frequencies for the slow (2.4m/s), medium (2.8m/s), fast (3.2m/s), and split (2.4 and 3.2m/s), resp., belt speeds. Those frequencies are measured using a stop watch during E0 and E4 phase; the metronome uses those frequencies during E1, E2, E3, E5, and E7 as shown in the last row.

Experiment paradigm The goal of our experiment (Fig. 11.2) was to obtain and compare the eigenvalues (recovery rate) of A_{CL} during E1 (slow belt speed), E3 (fast belt speed) and E5 phase (split belt, late adaptation) of the trials. The subjects were trained during E4. Near the end of E4, we measured the subjects stride frequency; we used those frequencies to set the metronome for E5.

11.3 Results and Discussion

11.3.1 Results

Figure 11.3 shows a typical data set from our experiment. As mentioned in Section 11.2.1, we use the segmental analysis to obtain the COM position. The COM velocity is calculated using the central difference method. Notice that due to the belt motor dynamics of the treadmill, the perturbation (belt speed changes) lasts for about 5 steps.

For our fitting, we reduce the data set by taking Poincaré sections at AP1 (Section 10.1.1). Figure 11.4 shows the superposition of the collected data corresponding to each type of perturbations. For each type of perturbations patterns emerge in the recovery strategy. Due in large part to unintentional offsets between the two belt speeds and the marker placements, we see step-to-step oscillations in the data.

Figure 11.5 shows a qualitative overview of changes that occur during different phases. The effects of different running speeds and adaptation can be seen.

We look at stride-based (instead of step-based) recovery strategy to avoid overfitting step-to-step oscillations. As mentioned in Section 11.1 we fit the linear model to the transient responses right after each perturbation. Figure 11.6 shows the transient responses after each perturbation for different trials (E1, E3, and E5) and simulations using the fitted A_{CL}^{stride} .

CHAPTER 11. BLACKBOX CLOSED-LOOP SYSTEM IDENTIFICATION

To develop a statistical understanding of the possible distribution of the eigenvalues of $A_{CL}^{stride}(E1)$, $A_{CL}^{stride}(E3)$, and $A_{CL}^{stride}(E5)$, we perform bootstrapping: we uniformly sample the collected data set (with replacement) and fit for A_{CL} . Iterating that for 500 times and binning the eigenvalues of A_{CL} from each fitting, we get Fig. 11.7. We see similar eigenvalues between E1 (slow belt) and E3 (fast belt). We see an eigenvalue very close to the origin indicating a deadbeat (either 1 or 2 step deadbeat) like structure. Figure 11.4 shows a quick recovery from perturbations in y^{AP1} . Furthermore, we see changes in eigenvalues between E1 (or E3) and E5 (mid or late adaptation). The near zero eigenvalue increased significantly in E5.

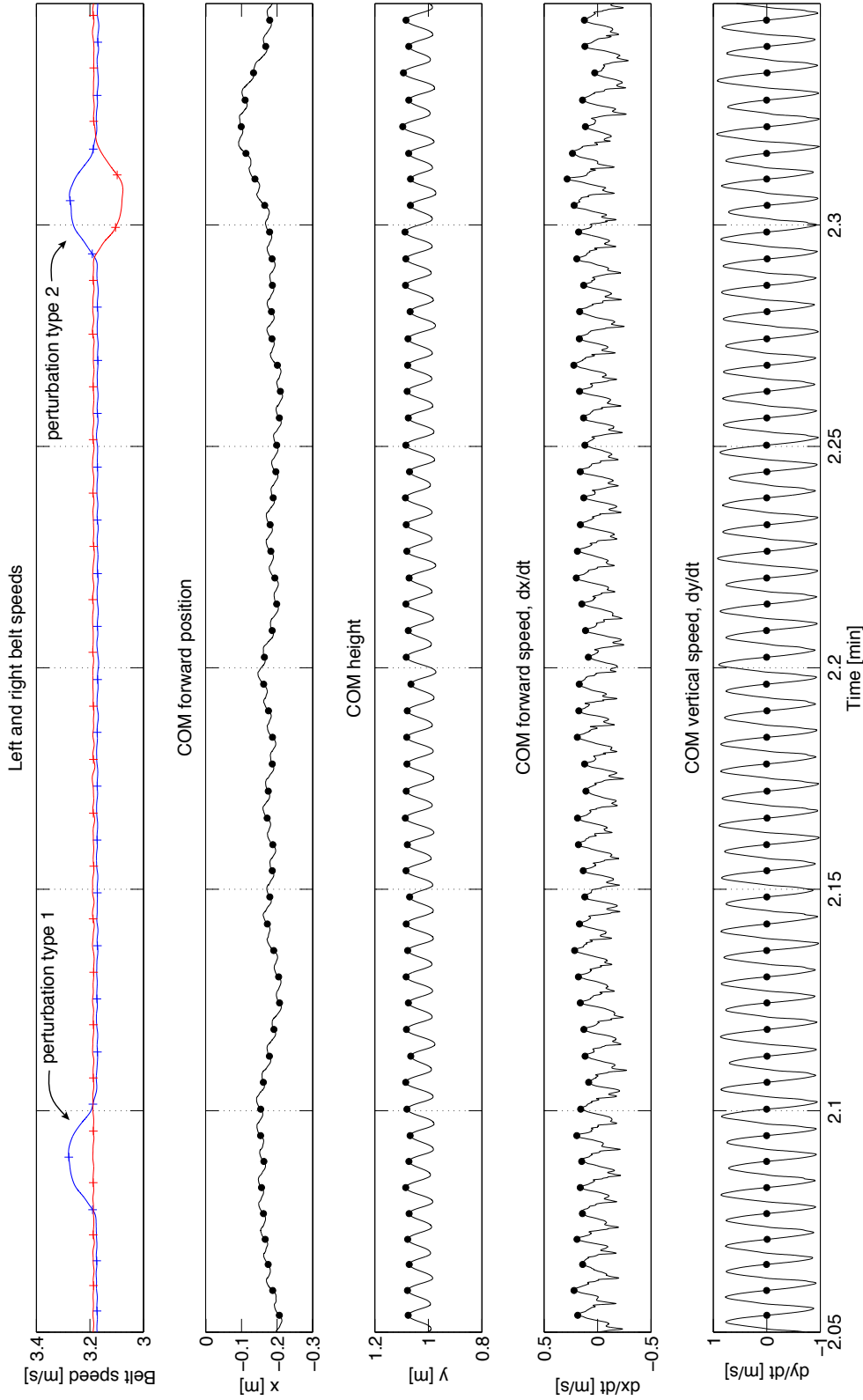
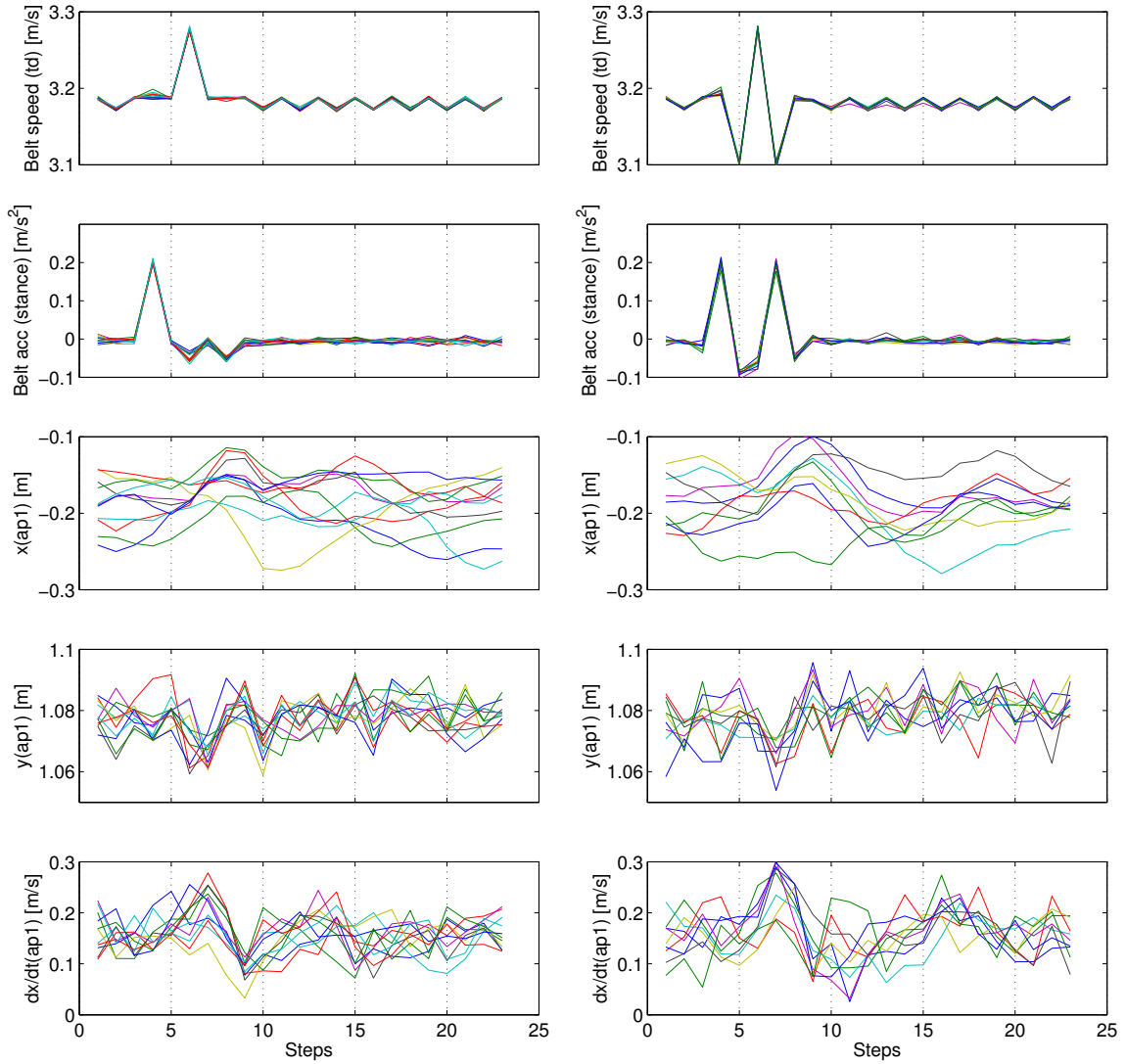


Figure 11.3: Collected data during E3 phase of a trial plotted against time. The first row shows the belt speeds for the left (red) and right (blue) belts; the crosshairs (+) indicate touch down of the corresponding leg. The second row shows the forward position of the COM; black dots (•), for the remaining plots, indicate COM apexes. The third row shows the height of the COM. The fourth row shows the forward speed of the COM. The fifth row shows the vertical speed of the COM.

CHAPTER 11. BLACKBOX CLOSED-LOOP SYSTEM IDENTIFICATION



(a) Perturbation type 1

(b) Perturbation type 2

Figure 11.4: Superposition of belt speed and acceleration perturbations of similar types during E3 phase and their corresponding COM responses plotted against *steps*. The first row shows the belt speed at at every touchdown. The second row shows the belt average acceleration during i -th stance phase. The third row shows the fore-aft position of the COM at apex. The fourth row shows the height of the COM at apex. The last row shows the COM forward speed at apex. Because we do not distinguish left versus right legs, step-to-step oscillations are introduced when there are unintentional offsets in belt speeds and marker positions.

CHAPTER 11. BLACKBOX CLOSED-LOOP SYSTEM IDENTIFICATION

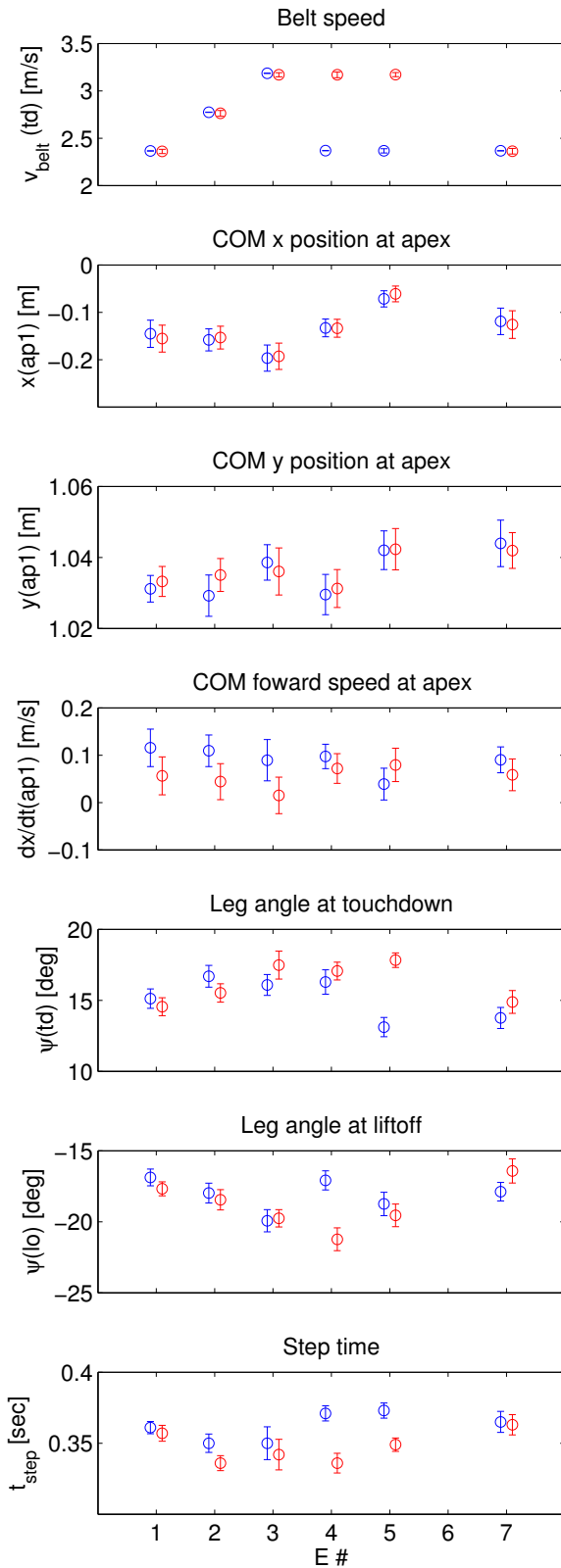


Figure 11.5: Effects of different running speeds and adaptation. The values are median of 50 contiguous steps selected at different phases of the experiment from one subject. This figure is meant to give a qualitative overview of steady-state changes that occur during different phases our experiment. Two colors show the median (open circles) and standard deviations (vertical lines) during 50 steps of corresponding experiment phases: the blue color is used for one leg, and the red color is used for the other leg. Note, for E4 phase, the median and std were obtained during early adaptation (EA). From E1 to E2 to E3, we see increase (decrease, resp.) in leg touchdown angle (leg liftoff angle, resp.). We see the leg touchdown angles being relatively similar during E3 and E4 (early adaptation); after adaptation, we see significant changes in leg touchdown and liftoff angles. E6 was unavailable for this particular experiment, hence empty.

CHAPTER 11. BLACKBOX CLOSED-LOOP SYSTEM IDENTIFICATION

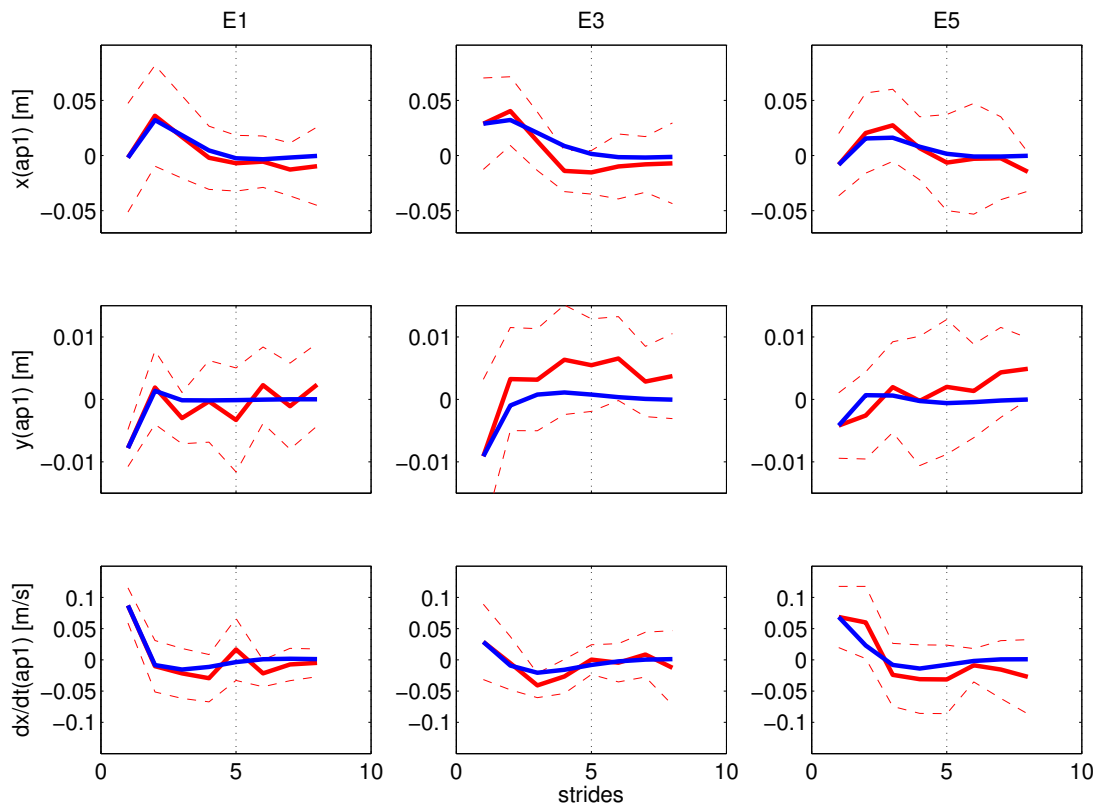


Figure 11.6: Transient response after perturbation from one subject. The solid red line is the mean of the trajectories corresponding to that run. The dashed red lines indicate $\pm \text{std}$'s. The blue lines are simulations of the linear fit to transient responses; the simulation uses the mean data (red) for the initial condition. Notice the abscissa shows strides (not steps nor time).

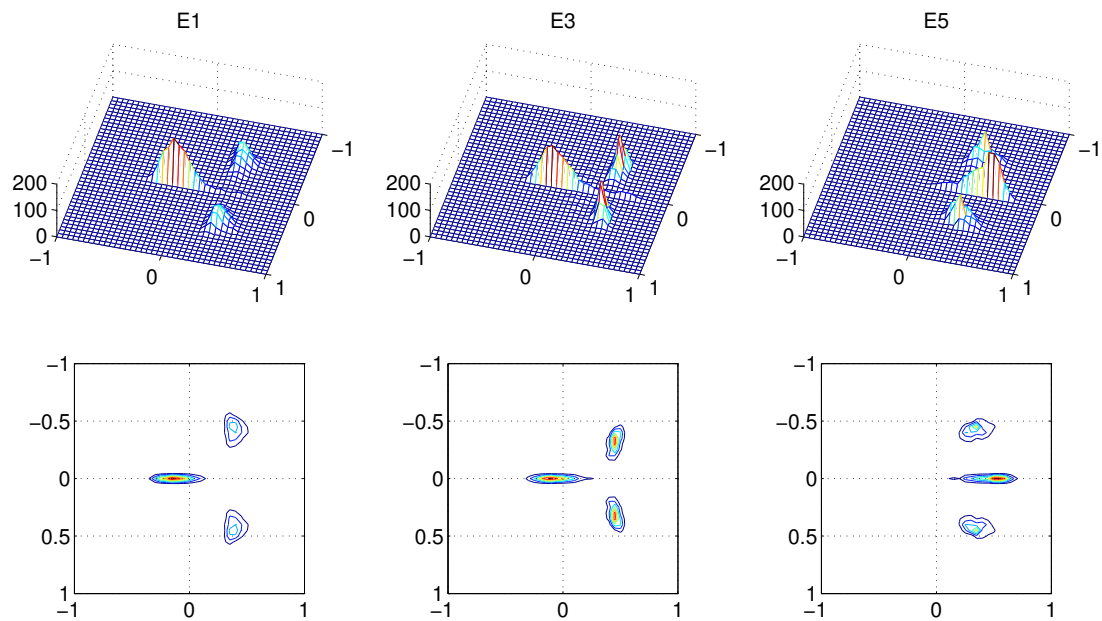


Figure 11.7: Eigenvalues of the A_{CL}^{stride} matrix fitted to the bootstrapped data from E1, E3, and E5 of one subject. The first row shows a 3D histogram of the eigenvalues. The second row shows the data but using contours.

11.3.2 Discussion

In this chapter, we fitted a linear model to the human transient response to belt-speed perturbations under different belt speeds and adaptation. We removed the effects of step-to-step oscillations by examining stride-to-stride mapping instead.

Closed-loop versus open-loop We fitted a closed-loop model which is composed of dynamics from musculoskeletal mechanics, muscle fatigue, neural delays, neural control, autoregressive noise, and many other factors. Hence we do not attribute the improvement or degradation of locomotor stability to any one specific factor. To elucidate the roles that each factor play would require further analyses, e.g., obtaining EMG signals to leg muscles.

Effects of running speed on stability In our result, we observed no significant difference in the eigenvalues between slow and fast running. This result does not rule out the Seyfarth et al.'s [105] prediction that increased running speed will improve (up to a limit) in the robustness for open-loop SLIP models. In human walking, on the other hand, England and Granata [29] showed that an increase in gait speed decreases gait stability. These results highlight the rolls that neural control and body mechanics play under different locomotor tasks. So, it may be that in unconstrained overground running that recovery rates in y^{AP1} and $\dot{x}^{B,AP1}$ may be deadbeat; our experimental approach cannot support or refute that possibility.

Effects of adaptation Suppose tied-belt stride-to-stride running is the product of two identical step-to-step mappings: $A_{CL}^{stride} = A_{CL}^{step} A_{CL}^{step}$. If the matrix A_{CL}^{stride} has only one eigenvalue at zero, then A_{CL}^{step} must have one eigenvalue at zero as well. Then, since the fast and slow tied-belt running

CHAPTER 11. BLACKBOX CLOSED-LOOP SYSTEM IDENTIFICATION

data each suggested one eigenvalue at zero for the *stride-to-stride* mapping (Fig. 11.7 first and second columns), then the *step-to-step* mappings for both fast and slow tied-belt running must also each have an eigenvalue at the origin. If split-belt running during late adaptation is the composition of a fast step and a slow step, then the stride-to-stride split-belt mapping must also have at least one eigenvalue at the origin. Since our result suggested an eigenvalue that is significantly away from the origin during late adaptation (Fig. 11.7 third column), this suggests that the adapted split-belt running is categorically different than simply the mathematical composition of a fast step with a slow step. Future research would benefit from fitting the step-to-step mapping in order to identify A_{CL}^{step} directly.

Did we rule out deadbeat control? No and Yes. We do not refute that humans use deadbeat control, say, in y^{AP1} . In fact, we partially support the argument because the height y^{AP1} seems to recover within one or two steps (Fig. 11.6). Our result do refute the claim that humans use deadbeat control, say, in $x^{W,AP1}$ and $\dot{x}^{W,AP1}$. It is not surprising however because such task of recovering in one step in $x^{W,AP1}$ (i.e., maintaining a fore-aft position while running on a treadmill) is not what humans do usually when running over ground (Section 10.1.3).

Effect of short-timescale feedback control on long-timescale adaptation We address how the short-time scale feedback control may place an upperbound on the rate of long-timescale adaptation. We do so by designing a simple control law that will make the eigenvalues of the closed-loop system to $[-0.1 \ 0.3 + 0.6i \ 0.3 - 0.6i]$ (similar to what we see in Fig. 11.7). Furthermore, we assume a hypothetical adaptive mechanism,

$$\alpha_{i+1} = \alpha_{i-1} - \eta(y_i^{AP1} - y_{i-1}^{AP1}), \quad (11.4)$$

CHAPTER 11. BLACKBOX CLOSED-LOOP SYSTEM IDENTIFICATION

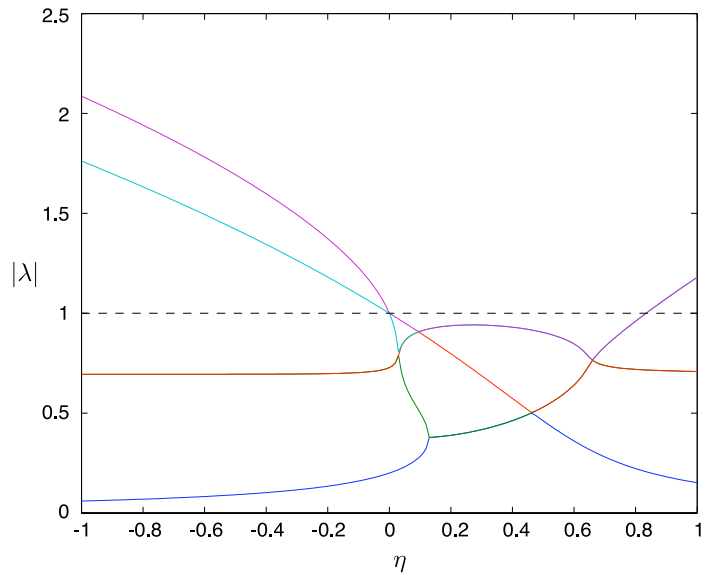


Figure 11.8: SLIP’s closed-loop eigenvalue magnitudes (y-axis) as a function of adaptation rate η (x-axis). The system is stable when $0 \leq \eta < 0.8$.

which minimizes the difference in height between two consecutive steps by changing the offset α for the corresponding leg’s touchdown angle; the rate that this adaptation takes place is denoted η . The closed-loop eigenvalues for the overall system, which includes this adaptive mechanism, is stable only for certain adaptation rates (see Fig. 11.8). If we plot the closed-loop eigenvalues of the overall system, which includes this adaptive mechanism, as a function of the adaptation rate η , we get Fig. 11.8. What we see here is that if the adaptation rate goes beyond 0.8, the overall system becomes unstable. While we do not claim that humans do this exactly, it does suggest a limit to the learning rate based on the overall stability argument, and such model-based predictions represent an exciting topic for future research.

Chapter 12

Conclusion

In this dissertation, we examined biological sensorimotor behaviors of two species: cockroach antenna-based wall following and human running on a split-belt treadmill. In Part I, we developed mathematical models and performed biological and robotic experiments and computer simulations to predict or support the proportional-derivative-like neural controller that cockroaches might employ during high-speed antenna-based wall following. In Part II, we modeled human running as a spring-loaded inverted pendulum with compositions of one-step deadbeat feedback controllers. Based on those assumptions, our result showed that the compositions of slow-belt feedback controllers best represented steady-state human running during early adaptation. We compared the eigenvalues of the linearized stride-to-stride closed-loop return map during late adaptation with those during baseline tied-belt running. Although not conclusive, our results suggested larger eigenvalues (i.e., slower recovery rate) during late adaptation, and, these two results taken together strongly suggest that the split-belt running is categorically different than simply the mathematical composition of a fast step with a slow step.

CHAPTER 12. CONCLUSION

Although American cockroaches and humans are quite different in both morphology and physiology, similar methods and tools proved useful to identify animal feedback control strategies. Specifically, the notion of templates and anchors [33] provided a general guide in terms of our ability to generate mathematical models to elucidate specific biological behaviors. Sensorimotor perturbation experiments elicited internal dynamics to allow identification of the mathematical model parameters. Control theory analyses with separate body mechanical and neural controller models allowed direct predictions of the structure of the neural controller.

As researchers seek and develop more comprehensive or detailed models that can capture complex behaviors in biological systems, future studies in modeling biological systems may benefit from a more formal treatment of how various models (e.g., operating at different time scales) relate from one another. For instance, using the analogy of computer software and hardware abstraction layers discussed in Section 1.2, developing interpreters (or “compilers”) from one level to another may be one way to address the growing number of complexities in models. Developing models and determining how they relate to one another, along with biological and robotic experiments and computer simulations, may provide unique insights into how animals integrate dynamic and complex sensory, neural, and musculoskeletal systems to achieve locomotion, i.e., move from one place to another.

Bibliography

- [1] R. M. Alexander. *Principles of Animal Locomotion*. Princeton University Press, 2002.
- [2] R. Altendorfer, D. E. Koditschek, and P. Holmes. Stability analysis of legged locomotion models by symmetry-factored return maps. *Int. J. Robot. Res.*, 23(10-11):979–999, 2004.
- [3] A. T. Asbeck, S. Kim, M. R. Cutkosky, W. R. Provancher, and M. Lanzetta. Scaling hard vertical surfaces with compliant microspine arrays. *Int. J. Robot. Res.*, 25(12):1165–1179, 2006.
- [4] K. Autumn, Y. A. Liang, S. T. Hsieh, W. Zesch, W. P. Chan, T. W. Kenny, R. Fearing, and R. J. Full. Adhesive force of a single gecko foot-hair. *Nature*, (405):681–685, JUN 2000.
- [5] J. Ayers. A reactive ambulatory robot architecture for operation in current and surge. In *Proc. Auton. Veh. Mines Countermeasures Symp.*, pages 15–31. 1995.
- [6] T. Barnes, T. Truong, G. Adams, and N. McGruer. Large deflection analysis of a biomimetic lobster robot antenna due to contact and flow. *Trans. ASME*, 68:948–951, 2001.
- [7] A. J. Bastian. Learning to predict the future: the cerebellum adapts feedforward movement control. *Curr. Opin. Neurobiol.*, 16(6):645–649, Dec 2006.

BIBLIOGRAPHY

- [8] C. E. Bauby and A. D. Kuo. Active control of lateral balance in human walking. *J Biomech*, 33(11):1433–1440, Nov 2000.
- [9] R. Blickhan. The spring-mass model for running and hopping. *J Biomech*, 22(11-12):1217–27, 1989.
- [10] R. Blickhan and R. J. Full. Similarity in multilegged locomotion: Bouncing like a monopode. *J. Comp. Physiol. A*, 173:509–517, 1993.
- [11] A. Bloch. *Nonholonomic Mechanics and Control*, volume 24. Springer, NY, 2003.
- [12] H. Bohm. Dynamic properties of orientation to turbulent air current by walking carrion beetles. *J. Exp. Biol.*, 198:1995–2005, 1995.
- [13] J. M. Camhi and E. N. Johnson. High-frequency steering maneuvers mediated by tactile cues: antenna wall-following in the cockroach. *J. Exp. Biol.*, 202:631–643, 1999.
- [14] S. G. Carver, N. J. Cowan, and J. M. Guckenheimer. Lateral stability of the spring-mass hopper suggests a two step control strategy for running. *Chaos*. Accepted.
- [15] G. A. Cavagna, N. C. Heglund, and C. R. Taylor. Walking, running, and galloping: Mechanical similarities between different animals. In T. J. Pedley, editor, *Scale Effects in Animal Locomotion, Proceedings of an International Symposium*, pages 111–125. Academic Press, New York, USA, 1975.
- [16] G. A. Cavagna, M. Mantovani, P. A. Willems, and G. Musch. The resonant step frequency in human running. *Pflugers Arch.*, 434:678–684, 1997.

BIBLIOGRAPHY

- [17] J. G. Cham, S. A. Bailey, J. E. Clark, R. J. Full, and M. R. Cutkosky. Fast and robust: Hexapedal robots via shape deposition manufacturing. *Int. J. Robot. Res.*, 21(10), 2002.
- [18] T. P. Chapman and B. Webb. A model of antennal wall-following and escape in the cockroach. *J Comp Physiol A Neuroethol Sens Neural Behav Physiol*, 192(9):949–969, Sep 2006.
- [19] J. T. Choi and A. J. Bastian. Split-belt treadmill adaptation during running. Unpublished.
- [20] C. M. Comer, L. Parks, M. B. Halvorsen, and A. Breese-Terteling. The antennal system and cockroach evasive behavior. ii. stimulus identification and localization are separable antennal functions. *J. Comp. Physiol. A*, 189:97–103, 2003.
- [21] N. J. Cowan and E. S. Fortune. The critical role of locomotion mechanics in decoding sensory systems. *J. Neurosci.*, 27(5):1123–1128, 2007.
- [22] N. J. Cowan, J. Lee, and R. J. Full. Task-level control of rapid wall following in the American cockroach. *J. Exp. Biol.*, 209(9):1617–1629, 2006.
- [23] N. J. Cowan, E. J. Ma, M. Cutkosky, and R. J. Full. A biologically inspired passive antenna for steering control of a running robot. In *Robotics Research*, Springer Tracts in Advanced Robotics, pages 540–550. Springer, Siena, Italy, 2003.
- [24] M. A. Daley and A. A. Biewener. Running over rough terrain reveals limb control for intrinsic stability. *Proc Natl Acad Sci U S A*, 103(42):15681–15686, Oct 2006.
- [25] F. Delcomyn. The locomotion of the cockroach *Periplaneta americana*. *J. Exp. Biol.*, 54:443–452, 1971.

BIBLIOGRAPHY

- [26] J. B. Dingwell, J. P. Cusumano, P. R. Cavanagh, and D. Sternad. Local dynamic stability versus kinematic variability of continuous overground and treadmill walking. *J Biomech Eng*, 123(1):27–32, Feb 2001.
- [27] D. M. Dudek and R. J. Full. Passive mechanical properties of legs from running insects. *J. Exp. Biol.*, 209(8):1502–1515, 2006.
- [28] V. Durr and A. Krause. Design of a biomimetic active tactile sensor for legged locomotion. In *Proceedings of the 5th International Conference CLAWAR*, Paris, France, 2002.
- [29] S. A. England and K. P. Granata. The influence of gait speed on local dynamic stability of walking. *Gait Posture*, 25(2):172–178, Feb 2007.
- [30] C. T. Farley, J. Glasheen, and T. A. McMahon. Running springs: speed and animal size. *J. Exp. Biol.*, 185:71–86, 1993.
- [31] G. F. Franklin, J. D. Powell, and A. Emami-Naeini. *Feedback Control of Dynamic Systems*. Addison-Wesley, third edition, 1994.
- [32] R. J. Full, R. Blickhan, and L. H. Ting. Leg design in hexapedal runners. *J. Exp. Biol.*, 158:369–390, 1991.
- [33] R. J. Full and D. E. Koditschek. Templates and anchors: neuromechanical hypotheses of legged locomotion on land. *J. Exp. Biol.*, 202(23):3325–3332, 1999.
- [34] R. J. Full, T. M. Kubow, M. Garcia, W. Schwind, and D. Koditschek. Can a simple neural oscillator generate rapid running in cockroaches? *Integr. Comp. Biol.*, 42(6):1232–1232, 2002.

BIBLIOGRAPHY

- [35] R. J. Full, T. M. Kubow, J. Schmitt, P. Holmes, and D. E. Koditschek. Quantifying dynamic stability and maneuverability in legged locomotion. *Integr. Comp. Biol.*, 42(1):149–157, 2002.
- [36] R. J. Full and M. S. Tu. Mechanics of six-legged runners. *J. Exp. Biol.*, 148:129–146, 1990.
- [37] R. J. Full and M. S. Tu. Mechanics of a rapid running insect: two-, four-, and six-legged locomotion. *J. Exp. Biol.*, 156:215–231, 1991.
- [38] A. R. Gallant. *Nonlinear Statistical Models*. Wiley, 1987.
- [39] P. P. Gambaryan. *How Mammals Run: Anatomical Adaptations*. Wiley, 1974.
- [40] S. A. Gard, S. C. Miff, and A. D. Kuo. Comparison of kinematic and kinetic methods for computing the vertical motion of the body center of mass during walking. *Hum Mov Sci*, 22(6):597–610, Apr 2004.
- [41] W. H. Gotwald. *Army Ants: The Biology of Social Predation*. Comstock Pub. Associates, 1995.
- [42] H. Gras, M. Horner, and F.-W. Schurmann. A comparison of spontaneous and wind-evoked running modes in crickets and cockroaches. *J. Insect Physiology*, 40(5):373–384, May 1994.
- [43] S. Grimmer, M. Ernst, M. Günther, and R. Blickhan. Running on uneven ground: leg adjustment to vertical steps and self-stability. *J. Exp. Biol.*, 211:2989–3000, Sep 2008.
- [44] C. Harley, B. English, and R. Ritzmann. Using your head: The involvement of the cockroach brain and head sensors in obstacle negotiation. In *Proc. Int. Symp. Adaptive Motion of Animals and Machines*, Cleveland, OH, June 2008.

BIBLIOGRAPHY

- [45] C. M. Harley, W. A. Lewinger, R. E. Ritzmann, and R. D. Quinn. Characterization of obstacle avoidance behaviors in the cockroach *Blaberus discoidalis* and implementation in a semi-autonomous robot. In *The Society for Integrative and Comparative Biology*, 2005.
- [46] M. J. Hartmann, N. J. Johnson, R. B. Towal, and C. Assad. Mechanical characteristics of rat vibrissae: Resonant frequencies and damping in isolated whiskers and in the awake behaving animal. *J. Neuroscience*, 23(16):6510–6519, 2003.
- [47] M. Heisenberg and R. Wolf. Reafferent control of optomotor yaw torque in *Drosophila melanogaster*. *J. Comp. Physiol. A*, 163(3):373–388, May 1988.
- [48] H. Herr and M. Popovic. Angular momentum in human walking. *J Exp Biol*, 211(Pt 4):467–481, Feb 2008.
- [49] D. R. Hofstadter. *Gödel, Escher, Bach: An Eternal Golden Braid*. London: Penguin, 1979.
- [50] P. Holmes, R. J. Full, D. Koditschek, and J. Guckenheimer. The dynamics of legged locomotion: Models, analyses, and challenges. *SIAM Rev.*, 48(2):207–304, 2006.
- [51] D. F. Hoyt and C. R. Taylor. Gait and the energetics of locomotion in horses. *Nature*, 292:239–240, 1981.
- [52] Y. Hurmuzlu and C. Basdogan. On the measurement of dynamic stability of human locomotion. *Transactions of the ASME*, 116:30–36, 1994.
- [53] R. Jeanson, S. Blanco, R. Fournier, J. Deneubourg, V. Fourcassie, and G. Theraulaz. A model of animal movements in a bounded space. *J Theoretical Biology*, 225(4):443–451, 2003.

BIBLIOGRAPHY

- [54] D. L. Jindrich and R. J. Full. Many-legged maneuverability: Dynamics of turning in hexapods. *J. Exp. Biol.*, 202(12):1603–1623, 1999.
- [55] D. L. Jindrich and R. J. Full. Dynamic stabilization of rapid hexapedal locomotion. *J. Exp. Biol.*, 205(18):2803–2823, 2002.
- [56] D. Jung and A. Zelinsky. Whisker-based mobile robot navigation. In *Proc. IEEE/RSJ Int. Conf. Intell. Robots Syst.*, volume 2, page 497, November 1996.
- [57] M. Kaneko, N. Kanayama, and T. Tsuji. Active antenna for contact sensing. *IEEE Trans. Robot. Autom.*, 14(2):278–291, 1998.
- [58] D. Kindersley. American cockroach (*Periplaneta americana*). <http://www.dkimages.com/discover/previews/976/80058786.JPG> [Online; accessed 8-December-2008].
- [59] R. Kram, B. Wong, and R. J. Full. Three-dimensional kinematics and limb kinetic energy of running cockroaches. *J. Exp. Biol.*, 200:1919–1929, 1997.
- [60] A. Lamperski, O. Loh, B. Kutscher, and N. J. Cowan. Dynamical wall-following for a wheeled robot using a passive tactile sensor. In *Proc. IEEE Int. Conf. Robot. Autom.*, pages 3838–3843, 2005.
- [61] C. E. Lang and A. J. Bastian. Cerebellar subjects show impaired adaptation of anticipatory emg during catching. *J Neurophysiol*, 82(5):2108–2119, Nov 1999.
- [62] J. Lee, A. Lamperski, J. Schmitt, and N. J. Cowan. Task-level control of the lateral leg spring model of cockroach locomotion. In M. Diehl and K. Mombaur, editors, *Fast Motions in*

BIBLIOGRAPHY

- Biomechanics and Robotics: Optimization and Feedback Control*, volume 340 of *Lecture Notes in Control and Information Sciences*, pages 167–188. Heidelberg: Springer-Verlag, 2006.
- [63] J. Lee, O. Y. Loh, and N. J. Cowan. A hierarchy of neuromechanical and robotic models of antenna-based wall following in cockroaches. In *Proc. IEEE/RSJ Int. Conf. Intell. Robots Syst.*, pages 3547–3553, San Diego, CA, USA, October 2007.
- [64] J. Lee, S. N. Sponberg, O. Y. Loh, A. G. Lamperski, R. J. Full, and N. J. Cowan. Templates and anchors for antenna-based wall following in cockroaches and robots. *IEEE Trans. Robot.*, 24(1):130–143, Feb. 2008.
- [65] W. A. Lewinger, C. M. Harley, R. E. Ritzmann, M. S. Branicky, and R. D. Quinn. Insect-like antennal sensing for climbing and tunneling behavior in a biologically-inspired mobile robot. In *Proc. IEEE Int. Conf. Robot. Autom.*, 2005.
- [66] L. Ljung. *System Identification*. Prentice-Hall, 1987.
- [67] C. Loudon. Flexural stiffness of insect antennae. *Amer. Entomol.*, 51:48–49, 2005.
- [68] M. Lungarella, V. V. Hafner, R. Pfeifer, and H. Yokoi. An artificial whisker sensor for robotics. In *Proc. IEEE/RSJ Int. Conf. Intell. Robots Syst.*, pages 2931–2936, Lausanne, Switzerland, 2002.
- [69] P. E. Marek and J. E. Bond. Biodiversity hotspots: rediscovery of the world’s leggiest animal. *Nature*, 441(7094):707, Jun 2006.

BIBLIOGRAPHY

- [70] R. Margaria. *Biomechanics and energetics of muscular exercise*. Oxford University Press, 1976.
- [71] P. V. McDonald, C. Basdogan, J. J. Bloomberg, and C. S. Layne. Lower limb kinematics during treadmill walking after space flight: implications for gaze stabilization. *Exp Brain Res*, 112(2):325–334, Nov 1996.
- [72] T. A. McMahon and G. C. Cheng. The mechanics of running: how does stiffness couple with speed? *J Biomech*, 23 Suppl 1:65–78, 1990.
- [73] T. M. Merritt. *Book of Insect Records*, chapter Fastest Runner. University of Florida, 1999. <http://ufbir.ifas.ufl.edu/>.
- [74] H. Nishino, M. Nishikawa, F. Yokohari, and M. Mizunami. Dual, multilayered somatosensory maps formed by antennal tactile and contact chemosensory afferents in an insect brain. *J. Comp. Neurol.*, 493(2):291–308, Dec 2005.
- [75] L. I. E. Oddsson, C. Wall, M. D. McPartland, D. E. Krebs, and C. A. Tucker. Recovery from perturbations during paced walking. *Gait Posture*, 19(1):24–34, Feb 2004.
- [76] J. Okada, Y. Kanamaru, and Y. Toh. Mechanosensory control of antennal movement by the scapal hair plate in the American cockroach. *Zool. Sci.*, 19(11):1201–1210, Nov 2002.
- [77] J. Okada and Y. Toh. The role of antennal hair plates in object-guided tactile orientation of the cockroach (*Periplaneta americana*). *J. Comp. Physiol. A*, 186(9):849–857, 2000.
- [78] J. Okada and Y. Toh. Spatio-temporal patterns of antennal movements in the searching cockroach. *J. Exp. Biol.*, 207:3693–3706, 2004.

BIBLIOGRAPHY

- [79] A. E. Patla. Understanding the roles of vision in the control of human locomotion. *Gait & Posture*, 5:54–69, 1997.
- [80] R. E. Poppele, G. Bosco, and A. M. Rankin. Independent representations of limb axis length and orientation in spinocerebellar response components. *J Neurophysiol*, 87(1):409–422, Jan 2002.
- [81] I. Poulakakis and J. W. Grizzle. Formal embedding of the spring loaded inverted pendulum in an asymmetric hopper. In *Proc. Euro. Control Conf.*, Kos, Greece, July 2007.
- [82] M. H. Raibert. *Legged Robots That Balance*. Cambridge: MIT Press, 1986.
- [83] D. S. Reisman, H. J. Block, and A. J. Bastian. Interlimb coordination during locomotion: what can be adapted and stored? *J Neurophysiol*, 94(4):2403–2415, Oct 2005.
- [84] E. Roth, M. B. Reiser, and N. J. Cowan. Reconciling open- and closed-loop experiments in sensorimotor control of *Drosophila*. In *The Society for Integrative and Comparative Biology*, Boston, MA, Jan 2009.
- [85] L. M. Roth. *The American Cockroach*, chapter Introduction, pages 1–14. Chapman and Hall Ltd, 1982.
- [86] A. Ruina. Non-holonomic stability aspects of piecewise-holonomic systems. *Rep. Math. Phys.*, 42(1-2):91–100, 1998.
- [87] J. Rummel and A. Seyfarth. Stable running with segmented legs. *Int. J. Robot. Res.*, 27:919–934, 2008.

BIBLIOGRAPHY

- [88] R. A. Russell. Object recognition using articulated whisker probes. In *Proc. Int. Symp. Intell. Robot.*, pages 605–11. Tokyo, 1985.
- [89] D. C. Sandeman. Physical properties, sensory receptors and tactile reflexes of the antenna of the australian freshwater crayfish *cherax destructor*. *J. Exp. Biol.*, 141(1):197–217, 1989.
- [90] U. Saranli. SimSect hybrid dynamical simulation environment. Technical Report CSE-TR-436-00, UM, Ann Arbor, MI, 2000.
- [91] U. Saranli, M. Buehler, and D. E. Koditschek. RHex: A simple and highly mobile hexapod robot. *Int. J. Robot. Res.*, 20(7):616–631, 2001.
- [92] U. Saranli and D. E. Koditschek. Template based control of hexapedal running. In *Proc. IEEE Int. Conf. Robot. Autom.*, volume 1, pages 1374–1379, Taipei, Taiwan, September 2003.
- [93] R. Schafer and T. V. Sanchez. Antennal sensory system of the cockroach, *Periplaneta americana*: postembryonic development and morphology of the sense organs. *J. Comp. Neurol.*, 149:335–354, 1973.
- [94] D. Schaller. Antennal sensory system of *Periplaneta americana* L.: distribution and frequency of morphologic types of sensilla and their sex-specific changes during postembryonic development. *Cell Tissue Res.*, 191(1):121–139, Jul 1978.
- [95] J. Schmitt, M. Garcia, R. C. Razo, P. Holmes, and R. J. Full. Dynamics and stability of legged locomotion in the horizontal plane: a test case using insects. *Biol. Cybern.*, 86:343–353, 2002.

BIBLIOGRAPHY

- [96] J. Schmitt and P. Holmes. Mechanical models for insect locomotion: dynamics and stability in the horizontal plane I. Theory. *Biol. Cybern.*, 83:501–515, 2000.
- [97] J. Schmitt and P. Holmes. Mechanical models for insect locomotion: dynamics and stability in the horizontal plane-II. Application. *Biol. Cybern.*, 83:517–527, 2000.
- [98] J. Schmitt and P. Holmes. Mechanical models for insect locomotion: active muscles and energy losses. *Biol. Cybern.*, 89:43–55, 2003.
- [99] A. E. Schultz, J. H. Solomon, M. A. Peshkin, and M. J. Hartmann. Multifunctional whisker arrays for distance detection, terrain mapping, and object feature extraction. In *Proc. IEEE Int. Conf. Robot. Autom.*, 2005.
- [100] W. J. Schwind. *Spring Loaded Inverted Pendulum Running: A Plant Model*. PhD thesis, University of Michigan, 1998.
- [101] W. J. Schwind and D. E. Koditschek. Approximating the stance map of a 2-dof monopod runner. *J. Nonlinear Science*, 10(5):533–568, 2000.
- [102] G. Seelinger and T. R. Tobin. *The American Cockroach*, chapter Sense Organs, pages 217–245. Chapman and Hall Ltd, 1982.
- [103] J. Seipel and P. Holmes. Three-dimensional translational dynamics and stability of multi-legged runners. *Int. J. Robot. Res.*, 25(9):889–902, September 2006.
- [104] J. Seipel, P. Holmes, and R. Full. Dynamics and stability of insect locomotion: a hexapedal model for horizontal plane motions. *Biol. Cybern.*, 91(2):76–90, 2004.

BIBLIOGRAPHY

- [105] A. Seyfarth, H. Geyer, M. Günther, and R. Blickhan. A movement criterion for running. *J Biomech*, 35(5):649–655, May 2002.
- [106] A. Seyfarth, H. Geyer, and H. Herr. Swing-leg retraction: a simple control model for stable running. *J. Exp. Biol.*, 206:2547–2555, Aug 2003.
- [107] M. A. Smith, A. Ghazizadeh, and R. Shadmehr. Interacting adaptive processes with different timescales underlie short-term motor learning. *PLoS Biol*, 4(6):e179, Jun 2006.
- [108] S. Sponberg, A. Spence, and R. J. Full. Testing neural control models for antenna-based tactile navigation in cockroaches. In *The Society for Integrative and Comparative Biology*, Orlando, FL, January 2006.
- [109] M. Srinivasan and A. Ruina. Computer optimization of a minimal biped model discovers walking and running. *Nature*, 439(7072):72–75, Jan 2006.
- [110] M. Srinivasan, S. Zhang, M. Lehrer, and T. Collett. Honeybee navigation en route to the goal: visual flight control and odometry. *J. Exp. Biol.*, 199(1):237–244, 1996.
- [111] E. Staudacher, M. Gebhardt, and V. Dürr. Antennal movements and mechanoreception: Neurobiology of active tactile sensors. *Advances in Insect Physiology*, 32:49–205, 2005.
- [112] K. Takakusaki and T. Okumura. Neurobiological basis of controlling posture and locomotion. *Advanced Robotics*, 22:1629–1663, 2008.
- [113] R. C. Taylor. Physical and physiological properties of the crayfish antennal flagellum. *J Neurobiol*, 6(5):501–519, Sep 1975.

BIBLIOGRAPHY

- [114] B. L. Thorne. Polygyny in the neotropical termite *Nasutitermes corniger*: life history consequences of queen mutualism. *Behav. Ecol. Sociobiol.*, 14:117–136, 1984.
- [115] L. H. Ting, R. Blickhan, and R. J. Full. Dynamic and static stability in hexapedal runners. *J. Exp. Biol.*, 197:251–269, 1994.
- [116] N. Ueno, M. Svinin, and M. Kaneko. Dynamic contact sensing by flexible beam. *IEEE/ASME Transactions on Mechatronics*, 3(4):254–263, 1998.
- [117] J. T. Watson and R. E. Ritzmann. Leg kinematics and muscle activity during treadmill running in the cockroach, *blaberus discoidalis*: II. fast running. *J. Comp. Physiol. A*, 182:23–33, 1998.
- [118] B. Webb. Can robots make good models of biological behaviour? *Behav. Brain Sci.*, 24(6):1033–50; discussion 1050–94, Dec 2001.
- [119] Wikipedia. American cockroach — Wikipedia, the free encyclopedia, 2008. http://en.wikipedia.org/w/index.php?title=American_cockroach&oldid=255665771 [Online; accessed 8-December-2008].
- [120] S. Ye, V. Leung, A. Khan, Y. Baba, and C. M. Comer. The antennal system and cockroach evasive behavior. i. roles for visual and mechanosensory cues in the response. *J. Comp. Physiol. A*, 189:89–96, 2003.

Vita

Jusuk Lee was born on November 23, 1981 in Seoul, Korea. He received the B.S. degree in electrical engineering and computer sciences from the University of California at Berkeley, Berkeley, in 2002 and the M.S. degree in mechanical engineering in 2005 from the Johns Hopkins University, Baltimore, MD, where he is currently working toward the Ph.D. degree in mechanical engineering. He is currently with the Locomotion in Mechanical and Biological Systems (LIMBS) Laboratory, Johns Hopkins University. His current research interests include animal locomotion and bio-inspired robotics.